Rapid Thermo-mechanical Modeling of Laser Powder-Bed Fusion Additive Manufacturing using an Effective Heat Source

by

Shahriar Imani Shahabad

A thesis

presented to the University of Waterloo

in fulfillment of the

thesis requirement for the degree of

Doctor of Philosophy

in

Mechanical and Mechatronics Engineering

Waterloo, Ontario, Canada, 2021

Examining Committee Membership

The following served on the Examining Committee for this thesis. The decision of the Examining Committee is by majority vote.

External Examiner	Henri Champliaud Professor, École de technologie supérieure
Supervisor	Ehsan Toyserkani Professor, University of Waterloo
Supervisor	Ali Bonakdar Adjunct Assistant Professor, University of Waterloo
Internal Member	Carolyn Ren Professor, University of Waterloo
Internal Member	Fue-Sang Lien Professor, University of Waterloo
Internal-external Member	John Zelek Associate Professor, University of Waterloo

Author's Declaration

This thesis consists of material all of which I authored or co-authored: see Statement of Contributions included in the thesis. This is a true copy of the thesis, including any required final revisions, as accepted by my examiners. I understand that my thesis may be made electronically available to the public.

Statement of Contributions

I want to acknowledge my co-author's contributions to the research described in this thesis:

Prof. Ehsan Toyserkani: Supervising the research, developing the initial idea for the current thesis, providing lab facilities, reviewing and editing papers.

Dr. Ali Bonakdar: Managing and supporting the research project, providing valuable discussions, reviewing and editing the papers.

Dr. Zhidong Zhang: Supporting in LPBF modeling, providing valuable discussions, reviewing the papers.

Dr. Usman Ali: Helping in conducting experimental tests, providing valuable discussion, and revising the papers.

Dr. Yahya Mahmoodkhani: Helping in conducting experimental tests and LPBF modeling, providing valuable discussions, and revising the papers.

Dr. Ali Keshavarzkermani: Helping in the characterization of the samples, providing valuable discussions, editing the paper.

Dr. Reza Esmaeilizadeh: Helping in the characterization of the samples, providing valuable discussions.

Abstract

Laser powder-bed fusion (LPBF) is one of the most common types of additive manufacturing (AM) processes that has gained a lot of attraction by industries. This process induces a high magnitude of a temperature gradient within the fabricated part due to fast thermal and cooling cycles. Therefore, the existence of residual stresses and deformation of produced parts is inevitable. There are a tremendous number of process parameters involved in LPBF that affect the quality of final products, such as laser power, scanning speed, layer thickness, hatching distance, etc. Modeling and simulation of LPBF provide an opportunity for predicting residual stresses and deformation of LBPF-made parts. Therefore, optimizing process parameters for minimizing residual stresses and deformation is required.

Extensive computational time and implementing a proper heat source model are some of the existing challenges in the modeling and simulation of LPBF. Due to micro-scale features of the LPBF melt pool zone, as well as the high-speed process (up to 5 m/s), the computational cost of the simulation process of making macro-scale large parts is highly expensive. On the other hand, extremely fine mesh is required for capturing heat transfer in the laser interaction zone accurately. Consequently, a large number of elements need to be analyzed for solving the problem, which requires a strong resource for computation.

This work presents the multi-scale modeling approach based on two groups of micro/mesoscale and macroscale simulations. Firstly, melt pool dimensions of Hastelloy X material single tracks were measured experimentally. Afterward, the micro/mesoscale simulation of LPBF single track was conducted, while implementing a volumetric heat source model (conical-Gaussian) to extract the transient temperature profile and melt pool dimensions. The percentage difference of melt pool depth and width dimensions derived from simulation results and experimental ones are 13% and 6%, respectively. The validated model was then used for multi-track multi-layer simulation. The effect of thin-wall thicknesses on the melt pool dimensions has been studied as an application of the multi-track simulation process. In the macroscale simulation, the thermo-mechanical model was developed for obtaining residual stresses and deformation of the fabricated part. As a major contribution, novel effective heat flux is proposed and applied for accelerating the simulation. Thermo-mechanical modeling of the cube building process is carried out using an effective heat flux. The residual stress is experimentally measured using an X-Ray analyzer machine. The simulation results show a good

agreement with experimental ones while a significant reduction in computational costs is achieved. The average percentage difference in predicting residual stress in longitudinal and transverse directions was 11% and the total computational time was 90 minutes.

Acknowledgments

First and foremost, I would like to express my sincere appreciation to my supervisor, Professor Ehsan Toyserkani who provided a great opportunity for me to join his top-notch team and work in Multi-scale Additive Manufacturing (MSAM) lab. I appreciate greatly his support in providing magnificent facilities and a research environment in the MSAM lab. Similarly, I would like to thank my co-supervisor Dr. Ali Bonakdar for his great support of my research project and his leadership on the Siemens Energy project. Moreover, I would like to appreciate Professor Mihaela Vlasea for her support and encouragement during these years.

I would like to thank Dr. Yahya Mahmoodkhani for his support and guidance on my research project and LPBF modeling. Moreover, I appreciate Dr. Usman Ali for providing valuable discussions and his support on my research project.

I was fortunate to have a collaboration with Dr. Zhidong Zhang who helped me a lot during these years and shared his valuable knowledge and experience with me during my Ph.D. program.

I want to thank my colleague in the Siemens project for their support, Dr. Ehsan Marzbanrad, Dr. Hamed Asgari, Dr. Yuze Sam Huang, Dr. Farid Ahmed, Dr. Ali Keshavarzkermani, Dr. Reza Esmaeilizadeh, Dr. Osezua Ibhadode, Pouyan Rahnama, Adhitan Rani Kasinathan, Ken Nsiempba, Katayoon Taherkhani, and Francis Dibia.

I had the great opportunity to collaborate with Dr. Marjan Molavi Zarandi and her professional team in the National Research Council Canada (NRC). I gained valuable knowledge and experience in the field of LPBF modeling during these times and I appreciate it.

Besides, I appreciate MSAM members who support me in every aspect of my studies, Dr. Bahareh Marzabrad, Dr. Mehrnaz Salarian, Dr. Haniyeh Fayazfar, Dr. Farzad Liravi, Dr. Esmat Sheydaeian Dr. Elham Davoodi, Mazyar Ansari, Alex Martinez, Sagar Patel, Gitanjali Shanbhag, Gijs Johannes Josef van Houtum, Issa Rishmawi.

I would like to thank Jerry Ratthapakdee, Karl Rautenberg, and Grace Kurosad for their great help in printing the parts and removing them from the substrate. Moreover, I would like to thank Toshi Suzuki and Henry Ma for their support in conducting residual stress measurements.

Besides, I thank my friends Milad Azvar, Hesam Kalbasi, Ali Karparvarfard who assisted me a lot in every aspect of my life and studies.

Last but not least I would like to profoundly appreciate the support of my family in each step of my life. I would not be in this position without their support, encouragement, and love.

Dedication

To my beloved family

Table of Contents

List of Figures

List of Tables

List of Symbols

Ω	Three-dimensional domain
Γ	Surface area [m^2]
b	Body force [N]
$\boldsymbol{S}^T$	Differential operator
$\boldsymbol{\sigma}$	Matrix stress tensor [N/m^2]
$\boldsymbol{t}$	Vector of surface tractions
Γ_t	Neumann boundary
Γ_u	Dirichlet boundary
$\bar{u}_i$	Prescribed displacement on the boundary [m]
$\boldsymbol{D}$	Elastic stress-strain matrix
$\boldsymbol{\sigma}_0$	Initial stress vector [N/m^2]
$\boldsymbol{\varepsilon}$	Strain vector
$\boldsymbol{N}$	Matrix of shape functions
$\boldsymbol{B}$	Strain matrix
$\boldsymbol{K}$	Stiffness matrix [N/m]
$\boldsymbol{F}$	External load vector [N]
E_h	Energy based on volume change [J]
E_d	Energy based on deformation [J]
v	Poisson's ratio
E	Young's modulus [GPa]
σ_y	Yield stress [MPa]
$\boldsymbol{D}_{ep}$	Elastoplastic constitutive matrix
$Q\ (x,y,z,t)$	Internal heat generation per unit volume [W/m^3]
$\boldsymbol{M}$	Capacitance matrix
$\boldsymbol{R}_Q$	Internal heat vector

$\boldsymbol{R}_s$	External surface flux vector
$\boldsymbol{R}_c$	Convection vector
$\boldsymbol{R}_r$	Radiation vector
C_p	Specific heat [J/kg.K]
I	Heat intensity distribution [W/m^3]
k	Thermal conductivity [W/m.K]
r_d	The lower radius of the heat source [μm]
q_c	Convective heat dissipation [W/m^2]
σ_{sb}	Stefan-Boltzmann coefficient [W/m^2.K^4]
z_e	z coordinates of the upper surface of the heat source [m]
h_c	Convection heat transfer coefficient [W/m^2.K]
H	Heat source height [μm]
q_0	The highest amount of heat intensity [W/m^3]
ε	Emissivity coefficient
r_0	The upper radius of the heat source [μm]
α	Absorption coefficient
L	Latent heat [J/Kg]
P	Laser power [W]
q_r	Radiative heat dissipation [W/m^2]
V	Scanning speed [m/s]
ρ	Density [Kg/m^3]
z_i	z coordinates of the lower surface of the heat source [m]
k_e	Effective thermal conductivity of powder material [W/m.K]
k_s	Thermal conductivity of solid material [W/m.K]
k_R	Thermal conductivity of the powder bed related to the radiation [W/m.K]
$k_{contact}$	Thermal conductivity attributed to the contact area of the particles [W/m.K]
k_g	The surrounding gas thermal conductivity [W/m.K]

B	Particle deformation parameter
$\emptyset$	The surface area of the particle in contact with another particle
φ	The porosity of the powder bed
$\dot{T}$	Cooling rate [K/s]
G	Temperature gradient [K/m]
R	Solidification rate [m/s]
λ_1	Primary spacing [μm]

Chapter 1. Introduction

1.1 Motivation

Laser Powder-Bed Fusion (LPBF) is the most common type of Additive Manufacturing (AM) process capable of producing complex geometries directly from digital drawing data and it has been gaining interest from researchers and industries recently [1], [2].

One of the major issues of this process is the existence of residual stresses and deformation of the printed parts because of inducing a high magnitude of temperature gradient and cooling rate during the manufacturing process [3]–[6]. Optimization of process parameters is essential for acquiring high-quality manufactured parts, which requires an extensive number of experimental tests based on a trial-and-error approach. Consequently, obtaining optimized process parameters for producing high-quality parts is immensely expensive [7], [8].

Modeling and simulation of LPBF provide an opportunity for predicting residual stresses and deformation of the final part. Therefore, a suitable set of optimized process parameters can be achieved cost-effectively for mitigating the final residual stresses and deformation of fabricated parts [9]. However, there are some challenges in modeling and simulation of LPBF as follows:

1- LPBF has the capability to fabricate parts using the layer-by-layer addition approach. Manufacturing large parts through a very thin layer thickness (20-100 μm) requires a high number of layers; therefore, the simulation of the entire process will be computationally expensive.

2- Various complex multi-physics phenomena are involved in LPBF, such as multi-phase (powder, liquid, solid, gas, and plasma) transitions and interactions, capillary force, Marangoni's flow, heat transfer, recoil pressure, buoyancy force, and thermo-mechanics. Therefore, considering all of the complex physics drastically increases the computational time for solving the problem.

3- In addition, for conducting precise analysis and solving complex problems using the finite element (FE) approach, extremely fine mesh size is required to capture heat flux in the laser interaction zone due to the small range of laser spot diameter (100 μm). Consequently, a high number of elements needs to be generated for LPBF modeling, which leads to increasing computational time.

4- As LPBF generates a high local temperature gradient during manufacturing the part, the existence of high magnitude residual stresses is inevitable within the final fabricated part. Therefore, implementing a proper heat source model is critical for obtaining a precise temperature field and predicting cooling rate, temperature gradient, residual stress, and deformation.

1.2 Objectives

The major goal of this work is to build a preliminary numerical model not only for predicting melt pool dimensions, temperature profile, cooling rate, and temperature gradient in the micro/mesoscale simulation but also for estimating residual stress and deformation in the macroscale simulation.

In order to achieve this goal, the objectives of this work are as follows:

1- In the micro/mesoscale simulation, a proper heat source model needs to be implemented for acquiring an accurate temperature field within the melt pool region. Experimental tests need to be done for verifying the model.

2- Reasonable assumptions need to be taken into account for increasing computational efficiency and accelerating the simulation process while obtaining reliable results in an acceptable range of accuracy.

3- In the macroscale simulation, a thermo-mechanical analysis is required to be conducted for predicting the residual stress and deformation of the final fabricated part. An effective heat flux needs to be implemented for accelerating the LPBF modeling on a large scale. In addition, it is necessary to carry out experimental studies for validating the model.

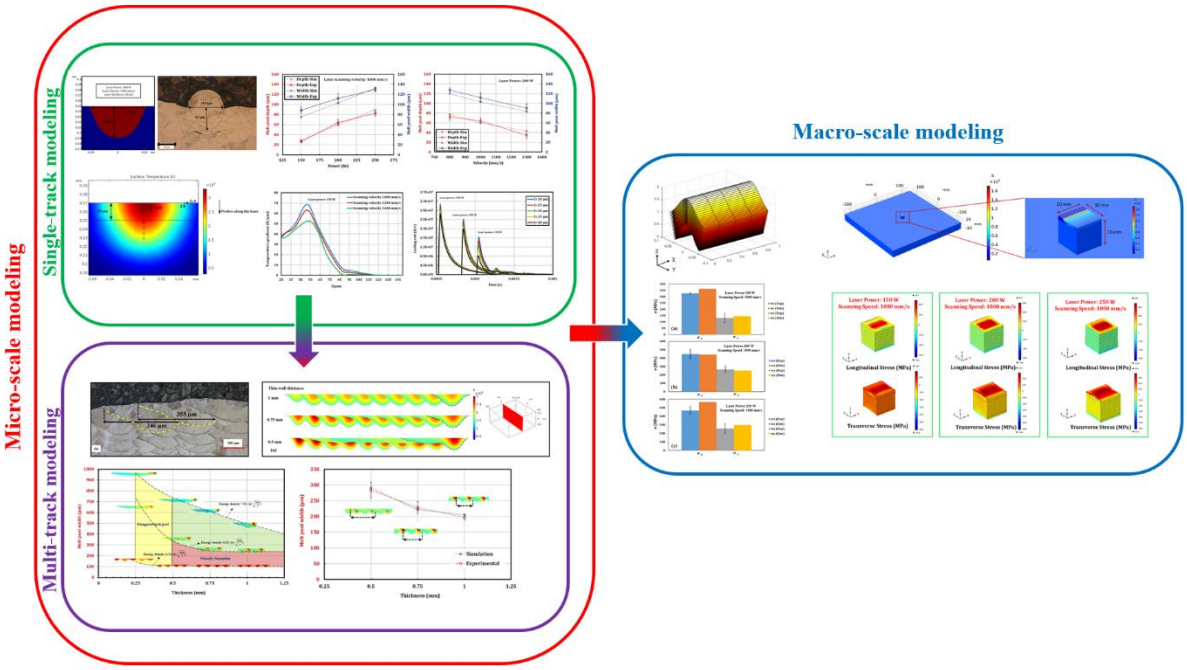

Fig. 1.1. Thesis graphical abstract.

1.3 Outline

This proposal has been organized in the following way.

Chapter 2 reviews relevant details of the modeling and simulation of the LPBF. **Chapter 3** describes the fundamentals of the Finite Element Method (FEM) of the LPBF process. **Chapter 4** illustrates thermal analysis in micro/mesoscale modeling including the single track simulation, multi-track multi-layer simulation. The experimental single-track investigation is carried out for calibrating a numerical model based on melt pool dimensions. **Chapter 5** shows the investigation of the influence of thin-wall thicknesses on melt pool dimensions as an application of multi-track process simulations. **Chapter 6** describes LPBF simulation in macroscale for conducting multi-track multi-layer thermo-mechanical analysis while a simple equivalent heat source model is implemented for accelerating the simulation. **Chapter 7** studies the thermo-mechanical modeling of the cube building process using a novel effective heat flux. The predicted residual stress results are compared with experimental ones. **Chapter 8** explains the summary and future work of this research.

Chapter 2. Literature review

This chapter will review on Laser Powder-Bed Fusion (LPBF) process as one of the most common types of Additive Manufacturing (AM) methods. Furthermore, the benefits of modeling and simulation of LPBF will be described. In addition, various approaches for modeling and simulation of LPBF will be explained.

It needs to be mentioned that each of the following chapters of the thesis has its own literature review and the purpose of this chapter is to describe the general background and explain the opportunities and challenges of the LPBF process.

2.1 Additive Manufacturing

The Additive Manufacturing process (AM) is a novel technology, which has been becoming more common to be adopted in industries such as aerospace, automotive, etc [10], [11]. This process has gained the advantage of producing complex shapes and geometries directly from digital drawing data [12]–[15]. There are different types of AM processes such as powder-bed fusion (PBF), vat photopolymerization (VP), directed energy deposition (DED), binder jetting (BJ), material extrusion (ME), material jetting (MJ), and sheet lamination (SL). PBF processes are further classified into; selective laser sintering (SLS), selective laser melting (SLM), and electron beam melting (EBM) [16], [17]. Fig. 2.1. demonstrates one of the gas turbine blades fabricated in the industry using additive manufacturing techniques.

Fig. 2.1. Printed gas turbine blades using Additive Manufacturing technology [18].

2.2 Laser Powder-Bed Fusion (LPBF)

The selective laser melting process, which is generally known as Laser powder-bed fusion (LPBF) produces parts using the layer upon layer addition approach [19]–[21]. After spreading metal powder on the build plate, the laser heat source selectively melts the powder particles and the solidified track takes the shape of the desired contour. A new layer of powder is then added to the previously solidified layer and this process is repeated until the final part is manufactured completely [17], [22], [23]. The schematic of LPBF is shown in Fig. 2.2.

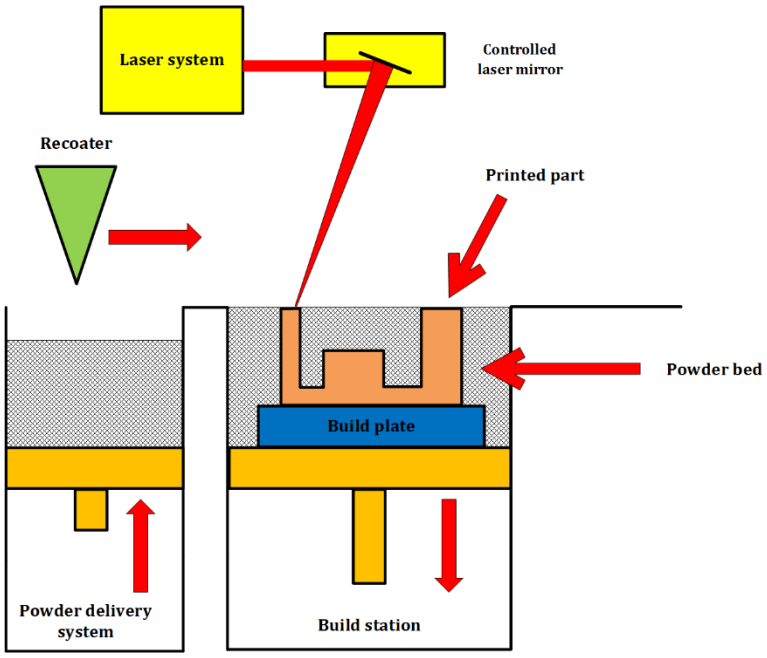

Fig. 2.2. Schematic of LPBF.

2.3 Simulation of Laser Powder-Bed Fusion (LPBF)

Modeling and simulation of LPBF provide an insight into understating the effect of process parameters on temperature distribution, residual stress, and deformation of the fabricated part without conducting a high number of trial-and-error experimental tests [24]–[26]. This section will focus on the modeling and simulation of LPBF, which can be classified into two groups of micro/mesoscale simulation (melt pool modeling) and macroscale simulation (part level modeling).

2.3.1 Micro/Mesoscale simulation (Melt pool modeling)

The quality of the manufactured part depends on melt pool features, which is evolved from selectively melting the powder by irradiation of the laser heat source [7], [27]. In order to analyze and capture melt pool features, an extremely fine-scale model (micro/mesoscale model) needs to be investigated numerically [28]. One of the major challenging issues in the simulation and modeling of LPBF is taking into consideration all complex multi-physics namely, phase change transformation from solid to liquid, Capillary or Marangoni phenomenon, recoil pressure, vaporization, etc [29]. As a result, considering all the complex multi-physics in modeling leads to increasing computational time for solving the problem [30]. Researchers have been attempting to carry out micro/mesoscale modeling for analyzing melt pool behavior and extracting temperature distribution adjacent to the laser beam interaction zone with powder material [31]–[34].

2.3.1.1 Discrete-domain simulation

Recently, some studies have been done in micro/mesoscale modeling of LPBF by taking into account the actual shapes of powder particles as a discrete domain [35], [36]. Gürtler et al. [37] developed a transient three-dimensional laser beam interaction model. They considered the complex hydrodynamic physics such as melting, wetting, and solidification phenomenon in their model by employing the volume of fluid method. Khairallah et al. [38] developed a three-dimensional model by using the ALE3D multi-physics code. They considered randomly distributed powder particles and coupled their model with hydrodynamics and surface tension while having an interaction of powder bed with a laser heat source. Fig. 2.3 illustrates the effect of considering surface tension in their model. In their recent investigation [39], they considered Marangoni convection and recoil pressure in their modeling approach. Results came out of their modeling showed that dynamical melt flow has a significant influence on evolving pore defects, material spattering, and denudation zones. Panwisawas et al. [40] developed a model considering powder particle distribution and thermal fluid flow. Their results illustrated that with increasing layer thickness and scanning speed, shapes of single track morphologies become irregular. Wu et al. [41] investigated melt pool behavior in LPBF by developing a three-dimensional heat transfer model. The randomly-packed powder was modeled by using the Discrete Element Method (DEM) method. The numerical results demonstrated that keyhole formation of melt pool was formed as the evaporation phenomenon occurred and the melt pool became a deep and narrow shape. Russell et al. [42] developed a model for resolving thermo-mechanical and material fields in LPBF by implementing Smooth Particle Hydrodynamics (SPH)

method. The Two-dimensional (2D) model illustrated that the driving force of the Marangoni phenomena has a significant influence on the process. In addition, they found that by increasing the laser power, surface roughness is suffered. Wang et al. [43] investigated modeling multi-track multi-layer LPBF. In their modeling approach, DEM and Volume of Fluid (VOF) methods had been coupled for reproducing powder particle deposition and melting the process.

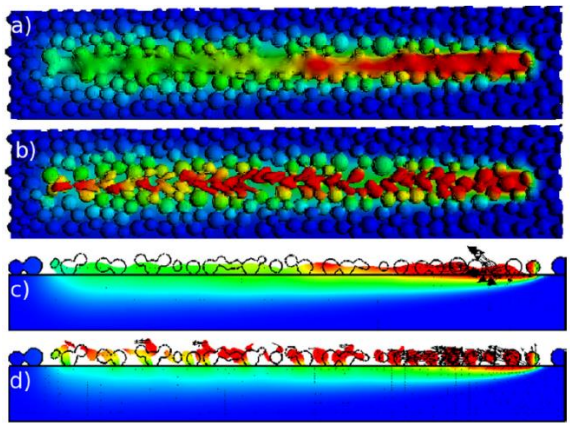

Fig. 2.3. (a and b) Laser tracks with and without surface tension, (c and d) 2D slices cut at the center of the tracks [38].

2.3.1.2 Continous-domain simulation

Since considering all of the underlying complex physics in LPBF for solving the problem is computationally expensive some researchers have been conducting modeling the micro/mesoscale simulation without considering individual powder particles as a continuous domain [29].

Antony et al. [44] investigated single track formation in LPBF of SS 316 powder on AISI 316L substrate. They developed a finite element model for predicting the temperature distribution in one layer of deposited powder. Moreover, the effect of process parameters on melt pool characteristics was studied. Y. Li and Gu [45] performed a numerical analysis of the LPBF of aluminum alloy powder. Their results showed that by increasing scanning speed from 100mm/s to 400 mm/s, the cooling rate was elevated significantly from 1.25×10^6 ºC/s to 6.17×10^6 ºC/s. Loh et al. [46] investigated numerically the LPBF of aluminum alloy 6061 using the FE method. They proposed an effective method considering volume shrinkage and material removal in their model. Their model was validated by experimental results. Huang et al. [47] studied the heat transfer phenomenon during LPBF. They investigated numerically the effect of linear energy density, volume shrinkage, hatch spacing, scanning track length, and the time interval between tracks on temperature distribution and

melt pool dimensions. They found that shorter track lengths caused lower temperature gradients and better quality of final products. In addition, by considering volume shrinkage, maximum temperature and melt pool dimensions slightly decrease. Foroozmehr et al. [48] developed a three-dimensional finite element model for investigating the effect of different process parameters on melt pool depth, width, and length. In their model, they considered the Optical Penetration Depth (OPD) of the laser beam in the powder bed which was taken into account in their heat source model. Liu et al. [49] developed a three-dimensional heat transfer finite element model for predicting microstructure during single track LPBF of AlSi10Mg material. Predicting microstructure was established by extracting thermal variables such as temperature gradient, cooling rate, and solidification rate from numerical analysis. In addition, anisotropic thermal conductivity was applied in their model. Validation of their model was conducted by comparing experimental melt pool geometries and surface features of the single-track process. Denlinger et al.[50] developed a model for predicting the temperature distribution of Inconel 718 during LPBF. They validated their model by comparing numerical results with in-situ temperature measurements using thermocouples during the process. Roy et al.[51] proposed a novel approach of finite element modeling of LPBF by taking into account the effect of consolidation on laser absorption of the material. Their results illustrated that consolidation would have an effective impact on laser absorption and decreases significantly as powder material transforms into melting and solidified phase. Hu et al. [52] developed a three-dimensional finite element model for investigating the effect of laser energy input on the melt pool depth, cooling rate, and temperature distribution during multi-layer deposition of LPBF. They found that maximum temperature and molten pool size increase as the number of layers increases. Y. Fu, C, and Guo [53] investigated three-dimensional (3D) finite element modeling of multi-layer LPBF. Temperature gradient and thermal cycle during the multi-layer build-up process were captured from their model. In addition, predicted melt pool dimensions derived from their modeling were validated with experimental measurements. Liu et al.[54] investigated multi-layer LPBF and subsequent thermal cycling happening during the process. Their modeling results showed that by increasing the number of layers, maximum temperature, melt pool dimensions, and liquid lifetime increase, while heating and cooling time rates decrease. Ali et al.[55] proposed a numerical model considering a volumetric heat source model for taking into account heat transfer penetration within the material. They were able to predict the cooling rate, temperature gradient, and residual stress evolution. Their model was validated based on melt pool dimensions which was extracted experimentally. Kundakc et al.[56] developed a finite element model considering 3D heat source to predict melt pool geometries and

temperature distribution during LPBF. They carried out some experimental tests on Inconel 625 and Titanium material for validating their model. Their model was able to predict melt pool shapes within the error range of 11-18 %. Fig. 2.4 shows the temperature distribution captured by their modeling. Du et al.[57] implemented a 3D Gaussian heat source in their model for predicting temperature field within LPBF. In addition, the variation of laser absorptivity with temperature was considered. Mishra and Kumar [58] applied a volumetric heat source model and considered thermos-fluidic transport in their modeling for LPBF of Ti64Al4V material. They validated their model based on some experimental measurements of melt pool size from the literature. Zhang et al.[59] studied on various common heat source models for predicting the melt pool dimensions in LPBF. They developed a novel model considering volumetric heat source, anisotropic thermal conductivity and varied absorptivity of the material. Their model was validated based on experimental melt pool geometries and surface features of the laser track.

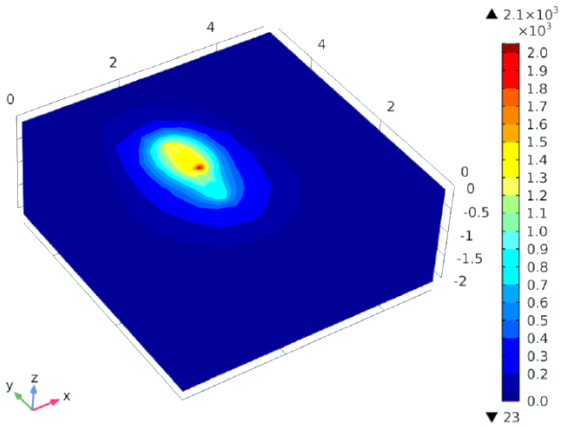

Fig. 2.4. The 3D temperature [°C] distribution of the 5 mm× 5 mm× 2 mm sample [56].

2.3.2 Macroscale simulation (build-up process modeling)

Macroscale simulation for predicting residual stress and deformation of LPBF processed part has been gaining interest from researchers recently. Few studies have been conducted in this area for modeling LPBF to predict residual stress and deformation for different geometries of parts such as cantilevers or even more complex geometries like gas turbine nozzle.

Zaeh and Branner [60] studied the evolution of residual stress and deformation produced during LPBF. They developed a finite element model for predicting residual stress during the production of the cantilever part and they validated their model based on neutron diffractometry experimental tests.

Papadakis and Loizou [61] proposed a reduction model approach for predicting the deformation of twin cantilever parts produced by LPBF. Their developed model results were close to the experimental investigation done by Zaeh and Branner. Keller and Ploshikhin [62] proposed a new approach for the fast prediction of deformation and residual stress called Mechanical Layer Equivalent (MLE). They used inherent strain value based on microscale simulation and conducted a structural analysis in macroscale modeling. The required computational time was decreased by more than two orders of magnitude. Denlinger et al.[63] implemented activation and deactivation of elements methodology for simulating large dimensions of components. Li et al.[64] developed a temperature thread multiscale modeling approach. A proposal equivalent heat flux was derived from the microscale model and applied to the mesoscale hatch model for deriving local residual stress. By mapping the results to the macroscale model they were able to predict the distortion of the twin cantilever part produced by LPBF. Fig. 2.5 depicts the validation of their model for predicting distortion of the cantilever part. Jayanath and Achuthan [65] developed a new finite element framework that allowed them to have coarse mesh size on the region which was far away from the heat source. Therefore, the computational cost would be decreased significantly. Li et al.[66] developed a multiscale modeling approach for LPBF. They scaled up their model in macroscale simulation and implemented larger layer thickness and heat source dimensions for accelerating the computational time. Bridge and L-shaped structures were investigated for predicting residual stress and deformation in the macroscale model. Cheng et al.[67] proposed a modified inherent strain approach for predicting residual stress and deformation. They studied two geometries of thin wall and rectangular contour during the directed energy deposition process (DED) for validation of their model. Their results showed that their modeling approach was capable of predicting residual stress and deformation accurately within a short period. Zhang et al.[68] developed a macroscale finite element model based on fraction layer energy input and level set approach. Their modeling approach was able to predict temperature history for complex geometries. Promoppatum et al. [69] conducted layer by layer heat input approach in their modeling for obtaining temperature distribution of macroscale part during build-up LPBF. Schänzel et al.[70] studied the thermo-mechanical finite element model of LPBF in the macroscale model. A new approach of the two-dimensional plane of interest for mechanical analysis by mapping temperature load from the previous step was proposed. In addition, adaptive mesh and heat source were implemented for reducing computational effort.

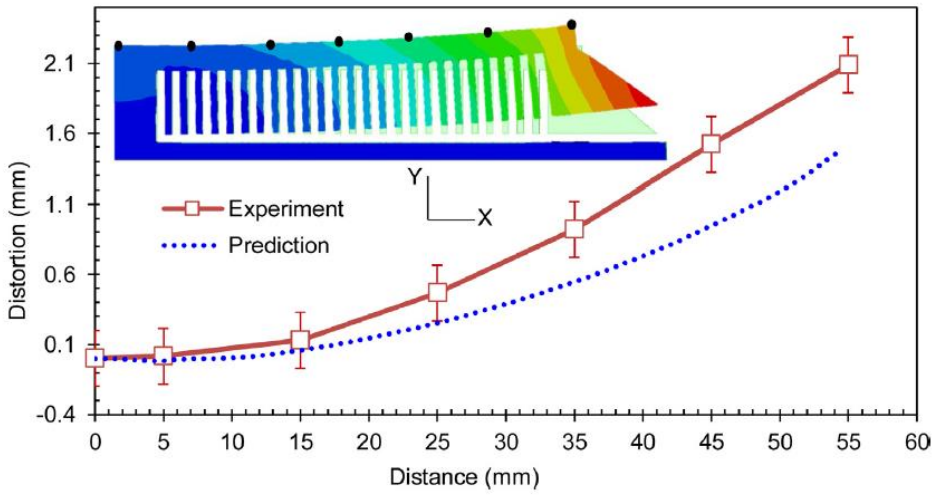

Fig. 2.5. Predicted distortion for cantilever part versus experimental measurement [64].

2.4 Summary

In this chapter, the importance of LPBF modeling has been specified. Two main modeling scales including micro/mesoscale and macroscale for modeling LPBF have been categorized and reviewed. Although modeling LPBF would be beneficial for industries and researchers, however, there have been limitations and challenges for LPBF modeling. For instance, accelerating computational time for solving the problem and fast prediction of residual stress and deformation of real LPBF processed part in an acceptable range of accuracy are some challenges which researchers would have faced in LPBF modeling. Most of the research on the macroscale model was based on the inherent strain approach which is a purely mechanical analysis method and is not close to the real building process. Few investigations are done on thermo-mechanical analysis using uniform heat flux on each layer which is not taken into consideration of laser scanning strategies and Gaussian profile of laser heat source. Therefore, the literature lacks comprehensive investigations on rapid thermo-mechanical modeling using an appropriate effective heat flux for predicting residual stress and deformation of the manufactured parts. Table 2.1 illustrates a summary of the modeling investigations done by researchers.

Table 2.1. Literature review summary.

Modeling scale	Domain	Researchers	Methodology
Micro/mesoscale	Discrete-domain	Gürtler et al. [37]	Employing volume of fluid method, considering the complex hydrodynamic physics such as melting, wetting and solidification phenomenon
		Khairallah et al.[39]	Considering Marangoni convection and recoil pressure
		Panwisawas et al. [40]	Considering powder particle distribution and thermal fluid flow
		Wu et al. [41]	Investigating melt pool behavior by developing a three-dimensional heat transfer model, Randomly packed powder was modeled by using the DEM method
		Wang et al. [43]	Investigating on modeling multi-track multi-layer LPBF by coupling DEM and VOF methods
	Continuous-domain	Y. Fu, C and Guo [53]	Investigating the modeling of multi-layer LPBF, Deriving temperature gradient, thermal cycle, and melt pool geometries
		Antony et al. [44]	Studying single track formation in LPBF, developing a finite element model for predicting the temperature distribution in one layer deposited powder.
		Loh et al. [46]	Proposing an effective method considering volume shrinkage and material removal in their modeling. Their model was verified by experimental results.
		Foroozmehr et al. [48]	Considering the Optical Penetration Depth of the laser beam in the powder bed and was taken into account in their heat source model.
		Zhang et al.[59]	Developing novel model considering volumetric heat source, anisotropic thermal conductivity, and varied absorptivity of the material.
Macroscale	Continuous-domain	Keller and Ploshikhin [62]	Proposing a new approach for fast prediction of deformation and residual stress called Mechanical Layer Equivalent (MLE), using inherent strain value based on microscale simulation and conducted structural analysis in macroscale modeling
		Denlinger et al.[63]	Implementing activation and deactivation of elements methodology for simulating large dimensions of components.
		Li et al.[66]	Scaling up the model in macroscale simulation and implementing increased layer thickness and heat source dimension for accelerating the computational time.
		Lia et al.[69]	Conducting layer by layer heat input approach in their modeling for obtaining temperature distribution of macroscale part during build-up LPBF.
		Schänzel et al.[70]	Implementing adaptive mesh and heat source for reducing the computational effort.

Chapter 3. Finite Element Method (FEM) basics of Laser Powder-Bed Fusion

3.1 Introduction

The Finite Element Method (FEM) has been gained a lot of interest from researchers and industries due to its advantage in heat transfer and structural analysis. Since complex multi-physics are involved in the LPBF process, FEM provides the opportunity to investigate further the physics behind this process. Moreover, by conducting FEM analysis temperature distribution, cooling rate, temperature gradient, residual stress, and deformation can be predicted without carrying out extensive experiments. In this chapter, three different categories of FEM analysis including, thermal analysis, mechanical analysis, thermo-mechanical analysis are going to be explained.

3.2 Fundamentals of mechanical analysis

3.2.1 Linear elasticity

The governing equations for a three-dimensional domain Ω and surface area of Γ can be written as follows [71]:

$$\begin{aligned} \frac{\partial \sigma_{xx}}{\partial x} + \frac{\partial \tau_{yx}}{\partial y} + \frac{\partial \tau_{zx}}{\partial z} + b_x = 0 \\ \frac{\partial \tau_{xy}}{\partial x} + \frac{\partial \sigma_{yy}}{\partial y} + \frac{\partial \tau_{zy}}{\partial z} + b_y = 0 \\ \frac{\partial \tau_{xz}}{\partial x} + \frac{\partial \tau_{yz}}{\partial y} + \frac{\partial \sigma_{zz}}{\partial z} + b_z = 0 \end{aligned} \tag{3.1}$$

In this equation, b_x, b_y, and b_z represent the body force in the *x*-, *y*-, and z-directions, respectively.

Based on the symmetry of the Cauchy stress, $\tau_{ij} = \tau_{ji}$, (*i, j=x, y, z).*

The governing equation can be described as follows:

$$\boldsymbol{S}^T\boldsymbol{\sigma} + \boldsymbol{b} = \boldsymbol{0} \tag{3.2}$$

where $\boldsymbol{S}^T$ represents the differential operator,

$$\boldsymbol{S}^T = \begin{Bmatrix} \frac{\partial}{\partial x} & 0 & 0 & \frac{\partial}{\partial y} & 0 & \frac{\partial}{\partial z} \\ 0 & \frac{\partial}{\partial y} & 0 & \frac{\partial}{\partial x} & \frac{\partial}{\partial z} & 0 \\ 0 & 0 & \frac{\partial}{\partial z} & 0 & \frac{\partial}{\partial y} & \frac{\partial}{\partial x} \end{Bmatrix} \tag{3.3}$$

The matrix stress tensor is represented by $\boldsymbol{\sigma} = \{\sigma_{xx}, \sigma_{yy}, \sigma_{zz}, \tau_{xy}, \tau_{yz}, \tau_{zx}\}^{\mathrm{T}}$, and the vector of the body load is shown as $\boldsymbol{b} = \{b_x, b_y, b_z\}^{\mathrm{T}}$.

The stress boundary conditions can be expressed as follows:

$$\begin{aligned} \boldsymbol{t_x} &= \boldsymbol{\sigma_{xx} n_x + \tau_{yx} n_y + \tau_{zx} n_z} \\ \boldsymbol{t_y} &= \boldsymbol{\tau_{xy} n_x + \sigma_{yy} n_y + \tau_{zy} n_z} \\ \boldsymbol{t_z} &= \boldsymbol{\tau_{xz} n_x + \tau_{yz} n_y + \sigma_{zz} n_z} \end{aligned} \tag{3.4}$$

The vector of surface tractions, $\boldsymbol{t} = \{t_x, t_y, t_z\}^{\mathrm{T}}$ is applied on the surface boundaries which is denoted as Γ_t (Neumann boundary).

On the other hand, the displacement boundary conditions are expressed as follows:

$$\mathrm{u}_i = \bar{\mathrm{u}}_i \tag{3.5}$$

The mentioned boundary is applied on the points of the surface denoted as Γ_u. (Dirichlet boundary). The prescribed displacement on the boundary is represented by $\bar{\mathrm{u}}_i$.

The above-mentioned equations are independent of the material. The constitutive equations that govern the stress-strain relations of the material are shown as follows:

$$\boldsymbol{\sigma = D(\varepsilon - \varepsilon_0) + \sigma_0} \tag{3.6}$$

The elastic stress-strain matrix is defined by $\boldsymbol{D}$, $\boldsymbol{\sigma}_0$ is the initial stress vector, $\boldsymbol{\varepsilon} = \{\varepsilon_{xx}, \varepsilon_{yy}, \varepsilon_{zz}, \gamma_{xy}, \gamma_{yz}, \gamma_{zx}\}^{\mathrm{T}}$ is the strain vector, and $\boldsymbol{\varepsilon}_0 = \{\varepsilon_{0xx}, \varepsilon_{0yy}, \varepsilon_{0zz}, \gamma_{0xy}, \gamma_{0yz}, \gamma_{0zx}\}^{\mathrm{T}}$ is the strain vector that is not generated from displacement.

The equation for the isotropic material can be expressed as the following,

$$\begin{bmatrix}\sigma_{xx}\\ \sigma_{yy}\\ \sigma_{zz}\\ \tau_{xy}\\ \tau_{yz}\\ \tau_{zx}\end{bmatrix} = \begin{bmatrix}\lambda+2\mu & \lambda & \lambda & & & \\ & \lambda+2\mu & \lambda & & & \\ & & \lambda+2\mu & & & \\ & & & \mu & 0 & 0\\ & Symm & & & \mu & 0\\ & & & & & \mu\end{bmatrix}\begin{bmatrix}\varepsilon_{xx}-\varepsilon_{0xx}\\ \varepsilon_{yy}-\varepsilon_{0yy}\\ \varepsilon_{zz}-\varepsilon_{0zz}\\ \gamma_{xy}-\gamma_{0xy}\\ \gamma_{yz}-\gamma_{0yz}\\ \gamma_{zx}-\gamma_{0zx}\end{bmatrix} + \begin{bmatrix}\sigma_{0xx}\\ \sigma_{0yy}\\ \sigma_{0zz}\\ \tau_{0xy}\\ \tau_{0yz}\\ \tau_{0zx}\end{bmatrix} \tag{3.7}$$

Moreover, for relating strain $\boldsymbol{\varepsilon}$ and displacement $\mathbf{u} = \{u_x, u_y, u_z\}$, the differential operator matrix $\boldsymbol{S}$ can be presented as follows:

$$\boldsymbol{\varepsilon} = \boldsymbol{S}\mathbf{u} \tag{3.8}$$

A weak version of the governing Eq. (3.2), can be expressed by multiplying the equation into an arbitrary function, virtual displacement vector $\delta\boldsymbol{u}$, and integrate it over the domain, [71], [72]. As a result, the weak form of the governing equation is presented as follows,

$$\delta\prod\nolimits_{eq} = \int_{\Omega} \delta\mathbf{u}^T(\boldsymbol{S}^T\boldsymbol{\sigma} + \boldsymbol{b})\, d\Omega = 0 \tag{3.9}$$

Based on Green's theorem, the equation can be described as follows:

$$\delta\prod\nolimits_{eq} = -\int_{\Omega} \delta(\boldsymbol{S}\mathbf{u})^T\boldsymbol{\sigma} d\Omega + \int_{\Gamma} \delta\mathbf{u}^T\boldsymbol{t} d\Gamma + \int_{\Omega} \delta\mathbf{u}^T\boldsymbol{b} d\Omega = 0 \tag{3.10}$$

By considering all the boundary conditions, the final equation can be described as follows,

$$\delta\prod\nolimits_{eq} = -\int_{\Omega} \delta(\boldsymbol{S}\mathbf{u})^T\boldsymbol{\sigma} d\Omega + \int_{\Gamma_t} \delta\mathbf{u}^T\boldsymbol{t} d\Gamma + \int_{\Omega} \delta\mathbf{u}^T\boldsymbol{b} d\Omega = 0 \tag{3.11}$$

3.2.2 FEM of linear elasticity

The Galerkin approach can be implemented for approximating Eq. (3.2), in such a way that the domain of interest Ω, is divided into subdomains or elements Ω_e which is shown in the following equation [71],

$$\Omega \approx \sum_e \Omega_e \tag{3.12}$$

Similarly, the boundary can be divided into sub-surfaces as follows,

$$\Gamma \approx \sum_e \Gamma_e = \sum_{e_t} \Gamma_{e_t} + \sum_{e_u} \Gamma_{e_u} \tag{3.13}$$

The tractions and displacements are applied in the boundaries Γ_{e_t} and Γ_{e_u}, respectively.

As a result, the weak form equation can be described as follows,

$$\delta \prod\nolimits_{eq} \approx \sum_e \left(-\int_{\Omega_e} \delta(\boldsymbol{S}\mathbf{u})^T \boldsymbol{\sigma} d\Omega + \int_{\Gamma_{e_t}} \delta\mathbf{u}^T \boldsymbol{t} d\Gamma + \int_{\Omega_e} \delta\mathbf{u}^T \boldsymbol{b} d\Omega \right) = 0 \tag{3.14}$$

The displacement $\boldsymbol{u}$ will be described by the finite element approximation as follows,

$$\mathbf{u}\,(x, y, z) \approx \boldsymbol{N}(x, y, z)\hat{\mathbf{u}} \tag{3.15}$$

$\boldsymbol{N}$ is a matrix of shape functions of an element with *n* nodes, and $\hat{\mathbf{u}}$ is the node-displacement vector of an element

$$\boldsymbol{N} = \begin{bmatrix} N_1 & 0 & 0 & N_2 & 0 & 0 & \dots & N_n & 0 & 0 \\ 0 & N_1 & 0 & 0 & N_2 & 0 & \dots & 0 & N_n & 0 \\ 0 & 0 & N_1 & 0 & 0 & N_2 & \dots & 0 & 0 & N_n \end{bmatrix} \tag{3.16}$$

The interpolation functions of displacement and the geometry are similar in the isoparametric form which is usually utilized in FEM. The equations can be presented as follows,

$$\mathbf{u}\,(\varepsilon, \eta, \xi) \approx \boldsymbol{N}(\varepsilon, \eta, \xi)\hat{\mathbf{u}} \tag{3.17}$$

$$\mathbf{x}\,(\varepsilon, \eta, \xi) \approx \boldsymbol{N}(\varepsilon, \eta, \xi)\hat{\mathbf{x}}$$

$\hat{\mathbf{x}} = \{x_1, y_1, z_1; \ldots; x_n, y_n, z_n\}$ expressed nodal coordinate parameters in the Cartesian system and ε, η, ζ are the parametric coordinates for each element.

The integration of weak form can be converted from element region Ω_e to the Gaussian range $-1 \leq \varepsilon, \eta, \zeta \leq 1$ by using the isoparametric form.

The volume element transformation from Cartesian to the natural coordinates can be expressed as follows,

$$dxdydz = det\boldsymbol{J}.\ d\varepsilon d\eta d\xi \tag{3.18}$$

The Jacobian transformation can be illustrated as follows,

$$\boldsymbol{J} = \frac{\partial\,(x,y,z)}{\partial\,(\varepsilon,\eta,\xi)} = \begin{bmatrix} \frac{\partial N_1}{\partial \varepsilon} & \frac{\sigma N_2}{\partial \varepsilon} & \cdots & \frac{\partial N_n}{\partial \varepsilon} \\ \frac{\partial N_1}{\partial \eta} & \frac{\partial N_2}{\partial \eta} & \cdots & \frac{\partial N_n}{\partial \eta} \\ \frac{\partial N_1}{\partial \xi} & \frac{\partial N_2}{\partial \xi} & \cdots & \frac{\partial N_n}{\partial \xi} \end{bmatrix} \begin{bmatrix} x_1 & y_1 & z_1 \\ x_2 & y_2 & z_2 \\ \vdots & \vdots & \vdots \\ x_n & y_n & z_n \end{bmatrix} \tag{3.19}$$

The strain-displacement equations can be represented as follows,

$$\boldsymbol{\varepsilon} = \boldsymbol{S}\mathbf{u} \approx \boldsymbol{SN}\hat{\mathbf{u}} = \boldsymbol{B}\hat{\mathbf{u}} \tag{3.20}$$

In this equation, $\boldsymbol{B}$ is the strain matrix. By substituting in Eq. (3.14) and adding material constitutive equations (3.6), the weak form equations can be shown as follows,

$$\delta \prod\nolimits_{eq} \approx \sum_e \delta\hat{\mathbf{u}}^T \left(-\int_{\Omega_e} \boldsymbol{B}^T \boldsymbol{D}\boldsymbol{B}\hat{\mathbf{u}} d\Omega + \int_{\Omega_e} \boldsymbol{B}^T \boldsymbol{D}\boldsymbol{\varepsilon_0} d\Omega - \int_{\Omega_e} \boldsymbol{B}^T \boldsymbol{\sigma_0} d\Omega + \int_{\Gamma_{e_t}} \boldsymbol{N}^T \boldsymbol{t} d\Gamma + \int_{\Omega_e} \boldsymbol{N}^T \boldsymbol{b} d\Omega \right) = 0 \tag{3.21}$$

In this equation, the terms in the bracket should be equal to zero because of arbitrary virtual displacement vector $\delta\hat{\mathbf{u}}$.

Moreover, by summing up to over all the elements, the final expression can be presented as follows,

$$\boldsymbol{KU} = \boldsymbol{F} \tag{3.22}$$

where $U = \hat{\mathbf{u}}$, and K is the stiffness matrix which can be illustrated as follows,

$$\boldsymbol{K} = \sum_{e} \int_{\Omega_e} \boldsymbol{B}^T \boldsymbol{D} \boldsymbol{B} d\Omega \tag{3.23}$$

and F is the external load vector, and can be described as follows,

$$\boldsymbol{F} = \sum_{e} \int_{\Omega_e} \boldsymbol{B}^T \boldsymbol{D} \boldsymbol{\varepsilon_0} d\Omega - \int_{\Omega_e} \boldsymbol{B}^T \boldsymbol{\sigma_0} d\Omega + \int_{\Gamma_{e_t}} \boldsymbol{N}^T \boldsymbol{t} d\Gamma + \int_{\Omega_e} \boldsymbol{N}^T \boldsymbol{b} d\Omega \tag{3.24}$$

The displacement $\boldsymbol{U}$ can be calculated from solving Eq. (3.23). Furthermore, the consequent results of stress and strain can be achieved.

3.2.3 Elastoplasticity

The plasticity of the material has three main criteria including 1. Yielding criteria where the limitation of the plastic deformation is defined; 2. The flow rule where the stress-strain relationship is defined; 3.The consistency condition in which the stresses are limited from exceeding the yield limit [71].

3.2.3.1 Stress-strain behavior

The plastic strain ε_p exists in the plastic deformation, as a result, the stress-strain equation will be shown as follows,

$$\boldsymbol{\sigma} = \boldsymbol{D} \left(\boldsymbol{\varepsilon} - \boldsymbol{\varepsilon_0} - \boldsymbol{\varepsilon_p} \right) + \boldsymbol{\sigma_0} \tag{3.25}$$

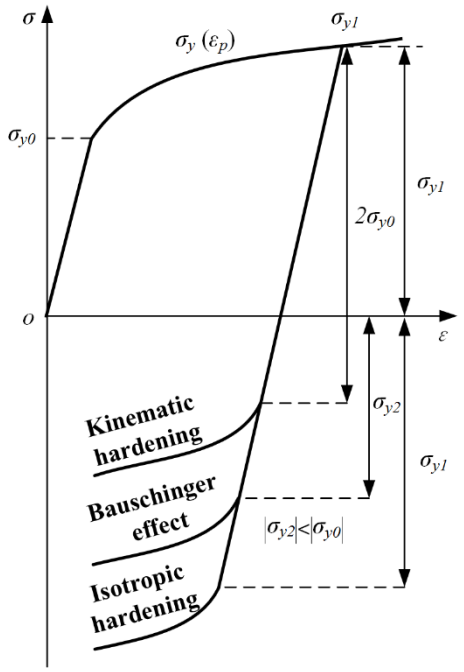

Fig. 3.1. Bauschinger effect and strain hardening type [71].

The strain-stress curves can be achieved by conducting tensile tests. The reduction in compressive yield stress after conducting cold tensile is observed which is called as Bauschinger effect [71], [73].

Furthermore, there are four basic models of the stress-strain behavior of the materials. The models include as follows: (a) linear elastoplastic model, (b) elastic perfectly plastic model, (c) rigid linear hardening model, and (d) rigid perfectly plastic model, as shown in Fig. 3.2. The tangent modulus is represented by H equal to $(\frac{E_{Tiso}}{1-\frac{E_{Tiso}}{E}})$ which is derived based on Isotropic tangent modulus E_{Tiso} and Young's modulus *E*.

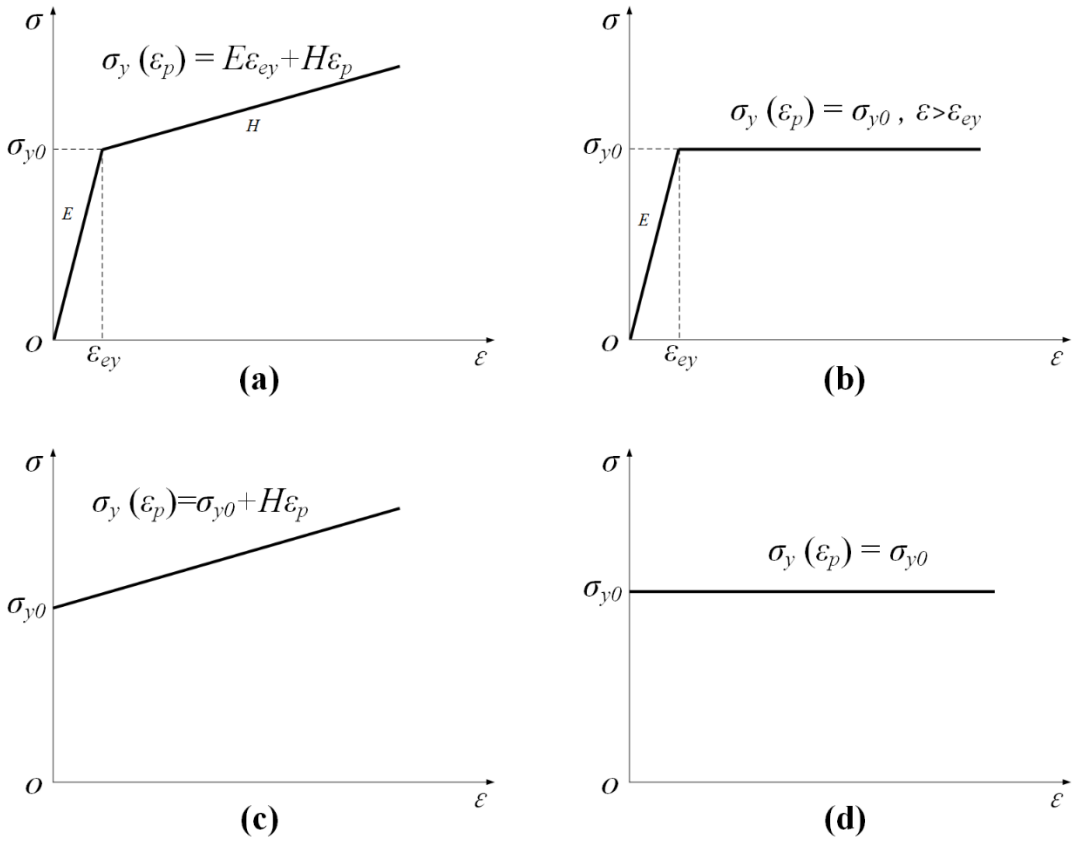

Fig. 3.2. Elastic and plastic deformation models, (a) linear elastoplastic model, (b) elastic perfectly plastic model, (c) rigid linear hardening model, (d) rigid perfectly plastic model [71]**.**

3.2.3.2 Deviatoric stress

It is realized that the yielding of the material is independent of hydrostatic stress due to the incompressible material assumption [71], [72]. Consequently, the deviatoric stress can be calculated by excluding the hydrostatic stress.

$$\begin{bmatrix} \sigma_{xx} & \tau_{yx} & \tau_{zx} \\ \tau_{xy} & \sigma_{yy} & \tau_{zy} \\ \tau_{xz} & \tau_{yz} & \sigma_{yy} \end{bmatrix} = \begin{bmatrix} \sigma_m & 0 & 0 \\ 0 & \sigma_m & 0 \\ 0 & 0 & \sigma_m \end{bmatrix} + \begin{bmatrix} S_{xx} & S_{yx} & S_{zx} \\ S_{xy} & S_{yy} & S_{zy} \\ S_{xz} & S_{yz} & S_{zz} \end{bmatrix} \tag{3.26}$$

The hydrostatic stress is presented as $\sigma_m = (\sigma_{xx+} \sigma_{yy} + \sigma_{zz})/3$ while the deviatoric stress is shown as the second matrix on the right-hand side of the equations. The characteristics of the deviatoric matrix are shown as follows,

$$S^3 - J_1 S^2 - J_2 S - J_3 = 0 \tag{3.27}$$

J_1, J_2, J_3 are represented as deviatoric invariants which are shown as follows,

$$J_1 = S_{xx} + S_{yy} + S_{zz} \tag{3.28}$$

$$J_2 = \frac{1}{6}\left[(S_{xx} - S_{yy})^2 + (S_{yy} - S_{zz})^2 + (S_{zz} - S_{xx})^2\right] + 6({S_{xy}}^2 + {S_{yz}}^2 + {S_{zx}}^2)$$

$$J_3 = S_{xx}S_{yy}S_{zz} - S_{xx}{S_{yz}}^2 - S_{yy}{S_{zx}}^2 - S_{zz}{S_{xy}}^2 + 2S_{xy}S_{yz}S_{xz}$$

J_2 plays an important role because of the von Mises stress yielding criterion which is defined as follows,

$$\sigma_e = \sqrt{\frac{3}{2}S_{ij}S_{ji}} = \sqrt{3J_2} \tag{3.29}$$

3.2.3.3 The criterion of yielding

The von Mises yielding criterion is usually used which can be described as follows [71], [72],

$$f = \partial_e - \partial_y \tag{3.30}$$

$$= \sqrt{\frac{1}{2}\left[\left(\sigma_{xx} - \partial_{yy}\right)^2 + \left(\sigma_{yy} - \sigma_{zz}\right)^2 + (\sigma_{zz} - \sigma_{xx})^2 + 6\left({\tau_{xy}}^2 + {\tau_{yz}}^2 + {\tau_{xz}}^2\right)\right]} - \sigma_y = 0$$

The von Mises yielding criterion is based on strain energy equivalence. The total strain energy can be expressed as follows,

$$E = E_h + E_d = \frac{1}{2}\boldsymbol{\sigma\varepsilon} \tag{3.31}$$

In this equation, E_h is the energy based on volume change, and E_d is the energy based on deformation. E_h can be calculated as follows,

$$E_h = \frac{3(1-2\nu)}{E}\left[\frac{\sigma_{xx}+\sigma_{yy}+\sigma_{zz}}{3}\right]^2 \tag{3.32}$$

The Poisson's ratio is represented by ν, and E is Young's modulus. E_d can be expressed as,

$$E_d = E - E_h = \frac{1+\nu}{3E}\left(\frac{1}{2}\left[\left(\sigma_{xx}-\partial_{yy}\right)^2 + \left(\sigma_{yy}-\sigma_{zz}\right)^2 + (\sigma_{zz}-\sigma_{xx})^2 + 6\left(\tau_{xy}{}^2 + \tau_{yz}{}^2 + \tau_{xz}{}^2\right)\right]\right) \tag{3.33}$$

Consequently, in uniaxial stress-state at yield point where, $\sigma_1 = \sigma_y$, $\sigma_2 = \sigma_3 = 0$, the deformation energy E_d in a uniaxial stress state will be as follows,

$$E_d = E - E_h = \frac{1+\nu}{3E}\sigma_y{}^2 \tag{3.34}$$

where σ_y is the yield stress. Therefore, by comparing Eq. (3.33) and Eq. (3.34), Eq. (3.30) is derived. In this equation, σ_y is the yield stress.

3.2.3.4 The rule of plastic flow

The direction of the flow is determined by the normality hypothesis of plasticity.

$$d\boldsymbol{\varepsilon}^p = d\lambda\frac{\partial f}{\partial \boldsymbol{\sigma}} \tag{3.35}$$

The equivalent plastic strain is calculated as follows,

$$d\bar{\varepsilon}^p = \sqrt{\frac{2}{3}\left[(d\varepsilon_1{}^p)^2 + (d\varepsilon_2{}^p)^2 + (d\varepsilon_3{}^p)^2\right]} \tag{3.36}$$

3.2.3.5 The consistency condition

The stresses should be restricted on the yield surface during the plastic deformation when yielding happens $f(\sigma, \bar{\boldsymbol{\varepsilon}}_p) = 0$.

The consistency condition is expressed as follows,

$$f(\boldsymbol{\sigma} + d\boldsymbol{\sigma}, \bar{\varepsilon}_p + d\bar{\varepsilon}_p) = f(\boldsymbol{\sigma}, \bar{\varepsilon}_p) + (\frac{\partial f}{\partial \boldsymbol{\sigma}})^T d\boldsymbol{\sigma} + \frac{\partial f}{\partial \bar{\varepsilon}_p} d\bar{\varepsilon}_p = 0 \tag{3.37}$$

The consistency condition can be more simplified because of $f(\boldsymbol{\sigma}, \bar{\varepsilon}_p) = 0$, the equation is shown as follows,

$$(\frac{\partial f}{\partial \boldsymbol{\sigma}})^T d\boldsymbol{\sigma} + \frac{\partial f}{\partial \bar{\varepsilon}_p} d\bar{\varepsilon}_p = 0 \tag{3.38}$$

3.2.4 FEM of elastoplasticity

Elastoplastic analysis plays a critical role in LPBF modeling. In two levels the Finite Element Method (FEM) problem can be solved, a) the global level—global load-deflection equations, b) the material level —the incremental stress-strain relations. The equilibrium should be considered in solving the global level while the strain-stress relation should be satisfied in solving the material level. A load increment is implemented in the elastoplastic analysis which results in displacement, strain, and stress increment [71], [74]. The incremental stress-strain relation can be expressed as follows,

$$d\boldsymbol{\sigma} = \boldsymbol{D}(d\boldsymbol{\varepsilon} - d\boldsymbol{\varepsilon_p}) \tag{3.39}$$

$d\varepsilon_p$ is identified by the associated flow rule, as a result, the following equation will be derived,

$$d\boldsymbol{\sigma} = \boldsymbol{D}(d\boldsymbol{\varepsilon} - d\lambda \frac{\partial f}{\partial \boldsymbol{\sigma}}) \tag{3.40}$$

By substituting Eq. (3.40) into Eq. (3.38) the following equation can be derived,

$$d\bar{\varepsilon}_p = \frac{\left(\frac{\partial f}{\partial \boldsymbol{\sigma}}\right)^T \boldsymbol{D} d\boldsymbol{\varepsilon}}{-\frac{\partial f}{\partial \bar{\varepsilon}_p} + \left(\frac{\partial f}{\partial \boldsymbol{\sigma}}\right)^T \boldsymbol{D}(\frac{\partial f}{\partial \boldsymbol{\sigma}})} \tag{3.41}$$

The elastoplastic relation equation can be achieved as follows by substituting the above-mentioned equation into Eq. (3.40),

$$d\boldsymbol{\sigma} = \boldsymbol{D}_{eq} d\boldsymbol{\varepsilon} = \left[\boldsymbol{D} - \frac{\boldsymbol{D}\left(\frac{\partial f}{\partial \boldsymbol{\sigma}}\right)\left(\frac{\partial f}{\partial \boldsymbol{\sigma}}\right)^T \boldsymbol{D}}{-\frac{\partial f}{\partial \bar{\varepsilon}_p} + \left(\frac{\partial f}{\partial \boldsymbol{\sigma}}\right)^T \boldsymbol{D}\left(\frac{\partial f}{\partial \boldsymbol{\sigma}}\right)} \right] d\boldsymbol{\varepsilon} \tag{3.42}$$

where $\boldsymbol{D}_{eq}$ is the elastoplastic constitutive matrix.

3.2.4.1 The global level

Global load-deflection equation can be used at the global level (Eq. (3.22)),

$$\boldsymbol{K}\boldsymbol{U} = \boldsymbol{F} \tag{3.43}$$

In this equation, $\boldsymbol{K}$ is the stiffness matrix and $\boldsymbol{F}$ is the applied load,

$$\boldsymbol{K} = \sum_e \int_{\Omega_e} \boldsymbol{B}^T \boldsymbol{D}_{eq} \boldsymbol{B} d\Omega \tag{3.44}$$

The stiffness matrix $\boldsymbol{K}$ is nonlinear due to its dependency on the stress state. Moreover, the equilibrium conditions (Eq. (3.43)) should be satisfied by incremental solving due to the nonlinear behavior of the material under several load steps. "*t*" represents the number of steps in nonlinear problems [71], [75].

The following equation shows the incremental relationship between force and displacement,

$${}^{t}\boldsymbol{K}\Delta\boldsymbol{U} = {}^{t+\Delta t}\,\Delta\boldsymbol{F} = {}^{t+\Delta t}\,\boldsymbol{R} - {}^{t+\Delta t}\,\boldsymbol{F} \tag{3.45}$$

The stiffness matrix at time *t* is represented by ${}^{t}\boldsymbol{K}$. The externally applied force at time $t+\Delta t$ is expressed by ${}^{t+\Delta t}\boldsymbol{R}$. The nodal forces related to the element stresses at time *t* are represented by ${}^{t+\Delta t}\boldsymbol{F}$.

The displacement increment can be expressed as ΔU and it is equal to ${}^{t+\Delta t}U = {}^{t}U + \Delta U$.

By estimating the displacement corresponds to the time $t+\Delta t$, the strains ${}^{t+\Delta t}\boldsymbol{\varepsilon}$, stresses ${}^{t+\Delta t}\boldsymbol{\sigma}$ and nodal point forces ${}^{t+\Delta t}\boldsymbol{F}$ related to the time $t+\Delta t$ can be obtained.

To prevent generating a significant error, the iterations need to be done until ${}^{t+\Delta t}\boldsymbol{F}$ is sufficiently close to ${}^{t+\Delta t}\boldsymbol{R}$ because the stiffness matrix at time t can be changed at the time $t+\Delta t$.

The classical Newton-Raphson technique is widely used for finite element analysis to conduct iterations [71], [72], [75]. Fig. 3.3a shows the schematic of iteration solving while ϵ is the convergence criterion.

Fig. 3.3b illustrates the modified Newton-Raphson method where the stiffness matrix is only computed at the beginning of each load step.

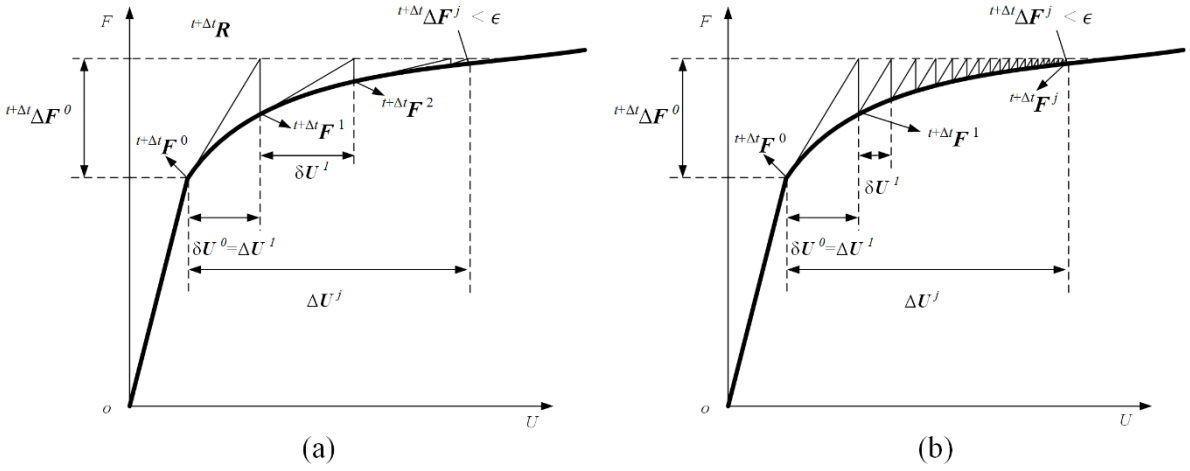

Fig. 3.3. The schematic of iteration solving displacement as a variable, (a) Newton-Raphson method, and (b) Modified Newton-Raphson method [71].

3.2.4.2 The material level

At the material level, the incremental stress-strain relations need to be considered since ${}^{t+\Delta t}\boldsymbol{F}^{j}$ is changed in every increment. The precise stresses define accurate ${}^{t+\Delta t}\boldsymbol{F}^{j}$, therefore the stresses should return to the yielding surface with considering the consistency requirement.

To calculate the stress increment for specific strain increment, two general methods can be implemented including a) implicit method, b) explicit method.

To obtain the increment $\Delta\boldsymbol{\sigma}$ by using the explicit method the integration of the infinitesimal constitutive relation can be calculated. The integration equation is shown as follows,

$$\Delta\boldsymbol{\sigma} = \int_{\boldsymbol{\sigma}_j}^{\boldsymbol{\sigma}_j+\Delta\boldsymbol{\sigma}} d\boldsymbol{\sigma} = \int_{\boldsymbol{\varepsilon}_j}^{\boldsymbol{\varepsilon}_j+\Delta\boldsymbol{\varepsilon}} \boldsymbol{D}_{eq} d\boldsymbol{\varepsilon} \tag{3.46}$$

The integral can be calculated by dividing the range ($\boldsymbol{\sigma}_j$, $\boldsymbol{\sigma}_j + \Delta\boldsymbol{\sigma}$) into the number of sub increments (N). The increase in the number of sub increments results in higher accuracy. However, by calculating $\boldsymbol{D}_{eq}$ several times, the error might still be accumulated which results in violating the stresses beyond the yield surface. On the other hand, in the implicit method, $\boldsymbol{D}_{eq}$ is calculated implicitly by solving a set of equations implementing the Newton-Raphson method.

The following equations are based on Eq. (3.40) and Eq. (3.37) can be summarized as follows,

$$\boldsymbol{P} = \Delta\boldsymbol{\sigma} - \boldsymbol{D}d\boldsymbol{\varepsilon} + \boldsymbol{D}d\lambda \frac{\partial f}{\partial \boldsymbol{\sigma}} \Big|_{\sigma=\sigma_A+\Delta\sigma} = 0 \tag{3.47}$$

$$q = f\left(\boldsymbol{\sigma} + d\boldsymbol{\sigma}, \bar{\varepsilon}_p + d\bar{\varepsilon}_p\right) = 0$$

The following equation can be obtained using the Newton-Raphson method.

$$\begin{bmatrix} \boldsymbol{I} + \boldsymbol{D}d\lambda \dfrac{\partial^2 f}{\partial \boldsymbol{\sigma}^2} & \boldsymbol{D}\dfrac{\partial f}{\partial \boldsymbol{\sigma}} \\ \left(\dfrac{\partial f}{\partial \boldsymbol{\sigma}}\right)^T & \dfrac{\partial f}{\partial \lambda} \end{bmatrix} \begin{bmatrix} \delta\boldsymbol{\sigma}^k \\ \delta\lambda^k \end{bmatrix} = \begin{bmatrix} -\boldsymbol{P}^k \\ -q^k \end{bmatrix} \tag{3.48}$$

The unknown variables are updated after calculation in each sub increment,

$$^{t+\Delta t}\,\Delta\boldsymbol{\sigma}^{k+1} = \Delta\boldsymbol{\sigma}^k + \delta\boldsymbol{\sigma}^k \tag{3.49}$$

$$^{t+\Delta t}\,\Delta\lambda^{k+1} = \Delta\lambda^k + \delta\lambda^k$$

Moreover, the stresses are updated as follows,

$$^{t+\Delta t}\boldsymbol{\sigma} = {}^{t}\boldsymbol{\sigma} + {}^{t+\Delta t}\Delta\boldsymbol{\sigma} \tag{3.50}$$

The nodal point forces at time $t+\Delta t$ can be calculated by using the following equation,

$$^{t+\Delta t}\mathbf{F} = \sum_{e}\int_{\Omega_e} \boldsymbol{B}^{T}\, {}^{t+\Delta t}\boldsymbol{\sigma}\mathrm{d}\Omega \tag{3.51}$$

3.3 Fundamental of heat transfer FEM

In this section, the basic FEM formulation of heat transfer is going to be explained. The fundamentals of solving the heat transfer problem are quite similar to the mechanical one since the FEM enables us to solve partial differential equations (PDF). Initially, the PDF is going to be derived in a weak form. Then, the weak form is going to be discretized in space and time.

Based on the Galerkin method, the domain is discretized into finite elements, and the finite difference approach is implemented for time discretization. Finally, for solving the global system equations the time integration techniques and Gauss quadrature will be employed.

The following equation shows the 3D heat transfer governing equation,

$$\rho c\frac{\partial T}{\partial t} = \nabla.(\boldsymbol{k}\nabla T) + Q(x,y,z,t) \tag{3.52}$$

In this equation, c is the specific heat, ρ is the material density, t is the time, T is the temperature, the x, y, and z are coordinates references, $\boldsymbol{k}$ = {k_x, 0, 0; 0, k_y, 0; 0, 0, k_z}are the thermal conductivity in x, y, and z-axis directions, and Q (x,y,z,t) is the internal heat generation per unit volume. Boundary condition equations are shown as follows,

$$T = T_{base}(x,y,z) \text{ on } \Gamma_1 \tag{3.53}$$

$$q_s = -q_2 \text{ on } \Gamma_2 \tag{3.54}$$

$$q_c = -h_c(T_{\text{sur}} - T_0) \text{ on } \Gamma_3 \tag{3.55}$$

$$q_r = -\varepsilon\sigma\left({T_{\text{sur}}}^4 - {T_0}^4\right) \text{ on } \Gamma_4 \tag{3.56}$$

The preheating of the substrate is represented by T_{base}, as a first Dirichlet boundary condition (Γ_1).

The heat flux on a surface is presented as q_s (Neumann boundary Γ_2). T_{sur} is the surface temperature, h_c is the coefficient of heat convection, q_c is represented as the convection boundary Γ_3. q_r is the radiation heat transfer boundary condition Γ_4; σ is Stefan-Boltzmann constant, and ε is the emissivity coefficient of the powder bed. δT is represented as a virtual temperature vector and the weak form of the governing Eq. (3.52) is shown as follows,

$$\delta \prod\nolimits_{eq} = \int_{\Omega} \delta T \left(-\rho c \frac{\partial T}{\partial t} + \nabla . (\boldsymbol{k} \nabla T) + Q(x, y, z, t) \right) d\Omega = 0 \tag{3.57}$$

By integrating the above equation using Green's theorem, the following equation can be achieved,

$$\delta \prod\nolimits_{eq} = -\int_{\Omega} \delta T \rho c \frac{\partial T}{\partial t} d\Omega - \int_{\Omega} \delta (\nabla T)^T \boldsymbol{k} (\nabla T) d\Omega + \int_{\Omega_Q} \delta T Q d\Omega + \int_{\Gamma} \delta T \boldsymbol{k} \nabla T d\Gamma = 0 \tag{3.58}$$

By substituting all the boundary conditions into the above equation, the final equation will be as follows,

$$\begin{aligned} \delta \prod\nolimits_{eq} = & -\int_{\Omega} \delta T \rho c \frac{\partial T}{\partial t} d\Omega \\ & - \int_{\Omega} \delta (\nabla T)^T \boldsymbol{k} (\nabla T) d\Omega \\ & + \int_{\Omega_Q} \delta T Q d\Omega + \int_{\Gamma_2} \delta T (-q_2) d\Gamma + \int_{\Gamma_3} \delta T (-h_c (T_{\text{sur}} - T_0)) \\ & + \int_{\Gamma_4} \delta T (-\varepsilon \sigma (T_{\text{sur}}{}^4 - T_0{}^4)) d\Gamma = 0 \end{aligned} \tag{3.59}$$

The Galerkin approach can be implemented to solve heat transfer problems using finite element approximation,

$$T(x, y, z) \approx \boldsymbol{N}(x, y, z) \widehat{\boldsymbol{T}} \tag{3.60}$$

Where $\boldsymbol{N}$ is a matrix of shape functions of an element with n node, and $\widehat{\boldsymbol{T}}$ is the temperature vector of an element,

$$\boldsymbol{N} = [N_1 \quad N_2 \quad \dots \quad N_n] \tag{3.61}$$

Consequently, the discretized weak form equation is shown as follows,

$$\begin{aligned}\delta \prod\nolimits_{eq} \approx \sum_e \delta \widehat{\boldsymbol{T}}^T \Bigg(& -\int_{\Omega_e} \rho_e c_e \boldsymbol{N}^T \boldsymbol{N} d\Omega \frac{\partial \widehat{\boldsymbol{T}}}{\partial t} \\ & - \int_{\Omega_e} \boldsymbol{B}^T \boldsymbol{k}_e \boldsymbol{B} d\Omega . \widehat{\boldsymbol{T}} \\ & + \int_{\Omega_{e_Q}} \boldsymbol{N}^T Q(x,y,z,t) d\Omega \\ & + \int_{\Gamma_{e_2}} -\boldsymbol{N}^T q_2 d\Gamma \\ & + \int_{\Gamma_{e_3}} -h_c \boldsymbol{N}^T \left(\boldsymbol{N}\widehat{\boldsymbol{T}} - \boldsymbol{T}_0\right) d\Gamma + \int_{\Gamma_{e_4}} -\varepsilon\sigma \boldsymbol{N}^T \left(\left(\boldsymbol{N}\widehat{\boldsymbol{T}}\right)^{\circ 4} - \boldsymbol{T}_0{}^{\circ 4} \right) d\Gamma \Bigg) = 0 \end{aligned} \tag{3.62}$$

In this equation, $^{\circ}$ is the element-wise power operation. The differential temperature matrix is expressed as $\boldsymbol{B}$ which is shown as follows,

$$\boldsymbol{B} = \boldsymbol{S}\boldsymbol{N} = \begin{bmatrix} \frac{\partial}{\partial x} \\ \frac{\partial}{\partial y} \\ \frac{\partial}{\partial z} \end{bmatrix} [N_1 \quad N_2 \quad \dots \quad N_n] = \begin{bmatrix} \frac{\partial N_1}{\partial x} & \frac{\partial N_2}{\partial x} & \dots & \frac{\partial N_n}{\partial x} \\ \frac{\partial N_1}{\partial y} & \frac{\partial N_2}{\partial y} & \dots & \frac{\partial N_n}{\partial y} \\ \frac{\partial N_1}{\partial z} & \frac{\partial N_2}{\partial z} & \dots & \frac{\partial N_n}{\partial z} \end{bmatrix} \tag{3.63}$$

The expression within the most-outside brackets in Eq. (3.62) is equal to zero since the virtual temperature vector $\delta\widehat{\boldsymbol{T}}$ is arbitratry.

The weak form equation after summing up to all elements will be generated as follows,

$$\boldsymbol{M}\frac{\partial \widehat{\boldsymbol{T}}}{\partial t} + \boldsymbol{K}\widehat{\boldsymbol{T}} = \boldsymbol{R}_Q + \boldsymbol{R}_s + \boldsymbol{R}_c + \boldsymbol{R}_r \tag{3.64}$$

In this equation, $\boldsymbol{R}_Q$ is the internal heat vector, $\boldsymbol{K}$ is the conduction matrix, $\boldsymbol{M}$ is the capacitance matrix, $\boldsymbol{R}_s$ is the external surface flux vector, $\boldsymbol{R}_c$ is the convection vector, and $\boldsymbol{R}_r$ is the radiation vector. The expressions are shown as follows,

$$\begin{aligned}
\boldsymbol{M} &= \sum_e \int_{\Omega_e} \rho_e c_e \boldsymbol{N}^T \boldsymbol{N} d\Omega \\
\boldsymbol{K} &= \sum_e \int_{\Omega_e} \boldsymbol{B}^T \boldsymbol{k}_e \boldsymbol{B} d\Omega \\
\boldsymbol{R}_Q &= \sum_e \int_{\Omega_{e_Q}} \boldsymbol{N}^T Q(x,y,z,t) d\Omega \\
\boldsymbol{R}_s &= \sum_e \int_{\Gamma_{e_2}} -\boldsymbol{N}^T q_2 d\Gamma \\
\boldsymbol{R}_c &= \sum_e \int_{\Gamma_{e_3}} -h_c \boldsymbol{N}^T \left(\boldsymbol{N}\widehat{\boldsymbol{T}} - \boldsymbol{T}_0\right) d\Gamma \\
\boldsymbol{R}_r &= \sum_e \int_{\Gamma_{e_4}} -\varepsilon \boldsymbol{\sigma} \boldsymbol{N}^T \left(\left(\boldsymbol{N}\widehat{\boldsymbol{T}}\right)^{\circ 4} - \boldsymbol{T}_0{}^{\circ 4}\right) d\Gamma
\end{aligned} \tag{3.65}$$

The weak form should be discretized in the time dimension as well. The α-method of time integration can be employed [76] and the following equation is obtained,

$$\begin{aligned}
\boldsymbol{M}\frac{\left({}^{t+\Delta t}\widehat{\boldsymbol{T}} - {}^{t}\widehat{\boldsymbol{T}}\right)}{\Delta t} &= (1-\alpha)^t\left(-\boldsymbol{K}\widehat{\boldsymbol{T}} + \boldsymbol{R}_Q + \boldsymbol{R}_s + \boldsymbol{R}_c + \boldsymbol{R}_r\right) + \alpha^{t+\Delta t}(-\boldsymbol{K}\widehat{\boldsymbol{T}} + \boldsymbol{R}_Q + \boldsymbol{R}_s \\
&\quad + \boldsymbol{R}_c + \boldsymbol{R}_r)
\end{aligned} \tag{3.66}$$

To acquire optimum stability and accuracy the α constant is employed in the equation.

The different procedures may be taken based on the α constant as follows [71], [75],

α = 0, explicit Euler forward method, conditionally stable;

α = 1/2, implicit trapezoidal rule, unconditionally stable;

α = 1, implicit Euler forward method, unconditionally stable;

The temperature gradient can be calculated after obtaining the temperature distribution as follows,

$$\nabla T \approx \begin{Bmatrix} \dfrac{T(x+\Delta x,y,z)-T(x-\Delta x,y,z)}{2\Delta x} \\ \dfrac{T(x,y+\Delta y,z)-T(x,y-\Delta y,z)}{2\Delta y} \\ \dfrac{T(x,y,z+\Delta z)-T(x,y,z-\Delta z)}{2\Delta z} \end{Bmatrix} \tag{3.67}$$

Moreover, the cooling rate can be estimated using the following equation,

$$\frac{\partial T}{\partial t} \approx \frac{T(x,y,z,t+\Delta t)-T(x,y,z,t)}{\Delta t} \tag{3.68}$$

3.4 Fundamentals of thermo-elasto-plasticity FEM

In the LPBF process, the laser fluxes heat into the material which causes thermal stress and elastoplasticity. Therefore, in the LPBF simulation, thermo-elastoplasticity needs to be considered for the analysis.

3.4.1 Basic equations

In the previous sections, all the essential equations for thermo-elastoplastic simulation are explained. The strain term in thermo-elastoplasticity is different compared with the elastoplasticity Eq. (3.39) which is shown as follows,

$$\boldsymbol{\sigma} = \boldsymbol{D}(\boldsymbol{\varepsilon} - \boldsymbol{\varepsilon}_p - \boldsymbol{\varepsilon}_T) \tag{3.69}$$

The thermal strain ε_T can be calculated as follows,

$$\boldsymbol{\varepsilon}_T = \alpha_{CTE}(T - T_0)\boldsymbol{I} \tag{3.70}$$

In this equation, the coefficient of the thermal expansion is represented as α_{CTE}. The current temperature is presented by T which can be calculated from transient heat transfer analysis explained in the previous section and T_0 is the ambient temperature. The mechanical analysis is the same as explained in the previous section.

3.4.2 The workflow of thermo-elastoplastic FEM

Multi-physics such as heat transfer and solid mechanics need to be considered in the LPBF simulation. The thermomechanical problem can be solved fully coupled as shown in Fig. 3.4a.

In other words, the thermal strain generated by heat transfer causes deformation in the printed parts. On the other hand, the created deformation may cause changes in the temperature distribution. Therefore, the two physics can be merged into one multi-physics set of equations to be solved. As a result, by solving each step using the Newton-Raphson method, temperature distribution and deformation with high accuracy can be calculated simultaneously.

However, using this approach is very time-consuming for solving the problem. Generally, in LPBF thermal strain induced by heat transfer is negligible and may not cause any changes in the heat transfer significantly. Thus, the decoupled thermo-mechanical approach is usually implemented for solving the thermo-mechanical problem as shown in Fig. 3.4b. In this method, initially, the heat transfer problem is solved and afterward, the mechanical analysis is done based on the thermal analysis results. Therefore, in each time step, only one physic is solved which leads to acceleration of the computation by solving a smaller matrix. There are a lot of investigations available using this approach [71], [77]–[79].

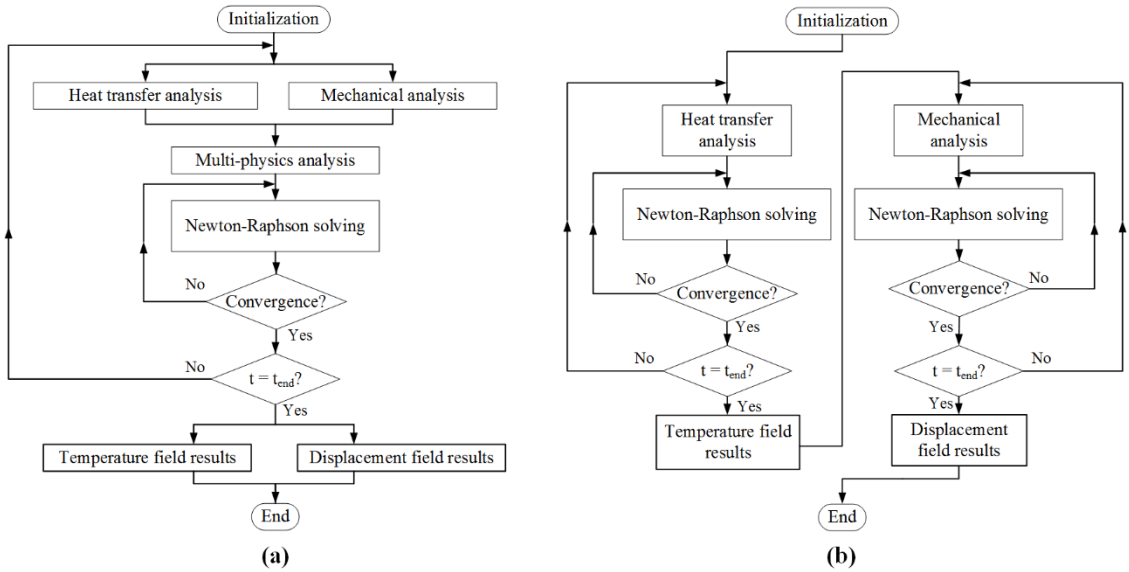

Fig. 3.4. Thermo-elastoplastic FEM workflow, (a) fully coupled method, (b) decoupled method [71].

3.5 Summary

In this chapter, the three categories of LPBF analysis are discussed including, elasto-plastic FEM, heat transfer FEM, and thermo-elastoplastic FEM. The equations for each section are presented. It is realized that using decoupled thermo-mechanical analysis leads to saving computational time significantly.

Chapter 4. Micro/Mesoscale Modeling of Laser Powder-Bed of Fusion*

4.1 Introduction

This chapter presents micro/mesoscale modeling of LPBF. Firstly, in the micro/mesoscale an efficient numerical-experimental approach is introduced to calibrate the parameters of a proposed three-dimensional (3D) conical Gaussian moving laser heat source model. For this purpose, several Hastelloy X single tracks were printed with various process parameters. The melt pool depth and width were measured experimentally, and results were used to calibrate and validate the heat source model. An empirical relationship between heat source parameters and laser energy density was also proposed. In addition, temperature gradients and cooling rates around the melt pool were extracted from the numerical model to be used towards microstructure prediction. Estimated microstructure cell spacing, calculated based on predicted cooling rate during solidification, was in good agreement with experimental measurements, indicating the validity of the heat source model. In addition, the multitrack-multilayer modeling process was conducted for obtaining temperature history from each layer.

To mitigate costs and turnaround time for identifying optimum process parameters and predict the temperature distribution and gradient for further microstructure analysis of printed parts, several numerical analysis methods have been implemented by many researchers [80]–[82].

Many studies on the LPBF modeling have been conducted. However, the literature lacks detailed procedures on calibrating the heat source models to develop a relationship between heat source parameters and melt pool geometries. The authors have previously published a work, in which variable thermal conductivity and absorption factors have been incorporated into the exponentially decaying heat source [59]. In this study, a conical-Gaussian heat source model [83], [84] with a varying depth of penetration along with a variable absorption factor has been implemented for modeling the melt pool depth and width of single tracks of Hastelloy X during LPBF. Numerical results showed excellent agreement with experimental melt pool geometries based on the varying laser power and scanning speed. In addition, temperature gradients and cooling rates due to their critical role in microstructure analysis such as predicting cell size, are also extracted from the numerical results.

* The materials presented in this chapter are adapted from the author's published work [106].

4.2 Experimental approach

In this study, the material choice is Hastelloy X (Nickel-based superalloy) which has an application in manufacturing gas turbine combustion systems due to its good creep resistance, tensile strength, corrosion resistance, and good ductility at high temperatures [84]. Single tracks of Hastelloy X were produced using an EOS M290 (EOS GmbH, Krailling, Germany) machine with a laser spot size of 100 µm. The laser of this system is a Ytterbium fiber laser with a wavelength of 1060 nm. Initially, substrates with dimensions of 25×18.5×5 mm were printed from the same material (Hastelloy X) by using the default EOS process parameters (laser power 195 W, scanning speed 1150 mm/s with hatch distance of 90 µm). Then, an additional layer thickness of powder was spread on top of the printed substrate to manufacture the single tracks with specified process parameters. For this study, various process parameters such as laser power and laser scanning speed were considered. The range of laser power and scanning speed are listed in (Table 4.1) which are used for validation of the numerical model. Fig. 4.1 shows the produced single tracks at different process parameters. The distance between every single track was 2.5 mm. Then, the printed specimens were removed from the build plate and cut perpendicular to single tracks using a Buehler ISOMET 1000 (Buehler, Illinois, USA) precision cutter with a 5 mm distance from the side of samples. Afterward, the specimens were mounted and polished before etching with a Glyceregia solution [85]. Finally, in order to measure the single tracks melt pool geometries, a Keyence VK-X250 confocal laser microscope (Keyence Corporation, Osaka, Japan) was used. In addition, a TESCAN VEGA 3 SEM (TESCAN, Brno, Czech Republic) was used for validating the cooling rate extracted from the numerical results based on cell spacing.

Table 4.1. Process parameters used in the validation of melt pool.

Process parameters	Values
Laser power (W)	150-200-250
Scanning Speed (mm/s)	800-1000-1200-1300
Laser spot diameter (µm)	100
Layer thickness (µm)	20

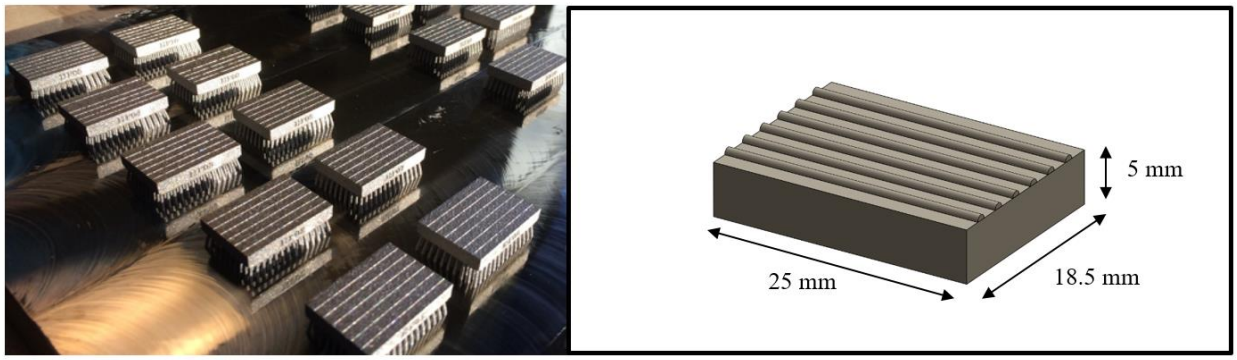

(a) (b)

Fig. 4.1. (a) Produced single tracks on printed substrates (b) Schematic of printed single tracks and the substrate.

4.3 Micro/mesoscale modeling (Single track simulation)

4.3.1 Model geometry and material properties

The commercial software COMSOL Multiphysics® was used to predict the melt pool dimensions, cooling rate, and temperature gradient during LPBF of Hastelloy X samples. In order to capture melt pool geometries in a microscale model, a substrate domain of 1×1×0.5 mm with a powder layer thickness of 0.02 mm on top was modeled. Tetrahedral mesh size (20 μm) with a number of elements 38344 was implemented such that in regions close to the laser-material interaction zone the finer mesh size was created as shown in Fig. 4.2.

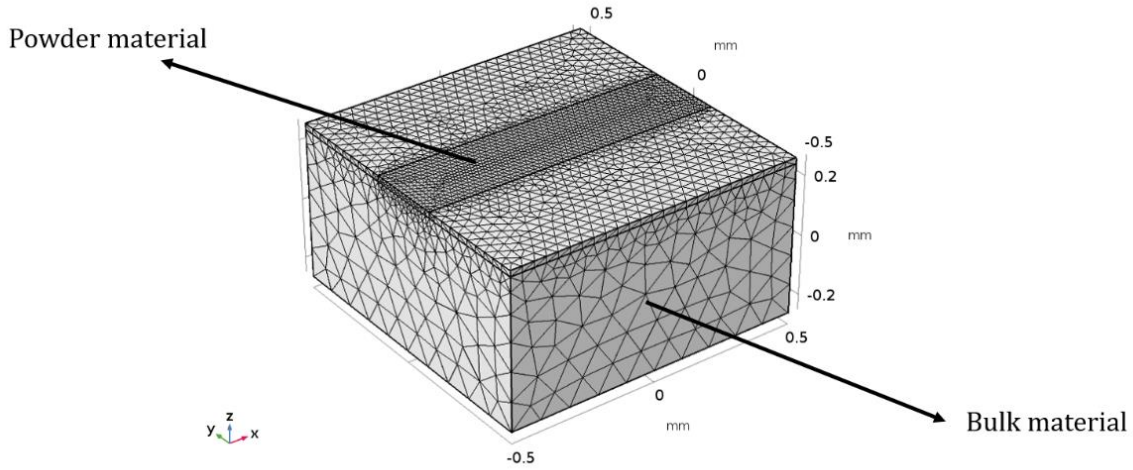

Fig. 4.2. Simulated single-track model geometry and mesh.

The properties of Hastelloy X material (Fig. 4.3) for bulk and powder were assigned to the respective domains. The thermal conductivity of powder material is derived using Eq. (4.1) [56]:

$$\frac{k_e}{k_g} = \left(1-\sqrt{1-\varphi}\right)\left(1+\frac{\varphi k_R}{k_g}\right) + \sqrt{1-\varphi}\left\{(1-\emptyset)\left[\frac{2}{1-\frac{Bk_g}{k_s}}\left(\frac{B}{\left(1-\frac{Bk_g}{k_s}\right)^2}\left(1-\frac{k_g}{k_s}\right)Ln\frac{k_s}{Bk_g} - \frac{B+1}{2} - \frac{B-1}{1-\frac{Bk_g}{k_s}}\right) + \frac{k_R}{k_g}\right] + \emptyset\frac{k_{Contact}}{k_g}\right\} \quad (4.1)$$

where k_e is the effective thermal conductivity of powder bed, k_g is the thermal conductivity of the gas, k_s is the thermal conductivity of solid, φ is the experimentally measured porosity of the powder bed (52%) [86], k_R is thermal conductivity of the powder bed due to radiation, $\emptyset$ is flattened surface fraction between particles (3×10^{-4}), B is deformation parameter of the particle which is assumed to be equal to 1, and $k_{contact}$ can be derived from Eq. (4.2) [87]:

$$\begin{Bmatrix} k_{contact} = 18\,\emptyset\,k_s & \emptyset < 3\times10^{-4} \\ k_{contact} \approx k_s & \emptyset > 0.01 \end{Bmatrix} \quad (4.2)$$

As shown in Fig. 4.3 (a), there is a huge difference between the thermal conductivity of powder and bulk material. The plot depicts that the thermal conductivity of the powder is much less than the bulk material (i.e., 1% of bulk material).

In addition, Fig. 4.3 (b) demonstrates the difference between the density of bulk and powder material which can be calculated based on the porosity of powder bed using Eq. (4.3).

$$\rho_{\text{powder}} = (1-\varphi)\rho_{\text{bulk}} \quad (4.3)$$

In order to consider phase change from solid to liquid, the apparent heat capacity method [31] is implemented (Eq. (4.4)):

$$C_p = \begin{Bmatrix} C_{\text{p, sensible}} & \text{if} \quad T < T_m - 0.5\Delta T_m \quad \text{or} \quad T > T_m + 0.5\Delta T_m \\ C_{\text{p, modified}} = C_{\text{p, sensible}} + \frac{L}{\Delta T_m} & \text{if} \quad T_m - 0.5\Delta T_m < T < T_m + 0.5\Delta T_m \end{Bmatrix} \quad (4.4)$$

where T_m is the melting temperature (1581 K) which is considered as the center point between solidus and liquidus temperature. ΔT_m is the temperature difference between liquidus (1628 K) and solidus temperature (1533 K) and L (227 KJ/Kg) is the latent heat of fusion. As shown in Fig. 4.3 (c), in this method the latent heat of fusion is compensated by increasing the specific heat between solidus and liquidus such that the extra heat absorbed by the material in this interval is equal to the latent heat of

fusion. Therefore, within those ranges of temperatures, the specific heat will be increasing dramatically.

It needs to be mentioned that for simplicity and acceleration of computation, it is assumed that the absorption coefficient is not affected by phase change.

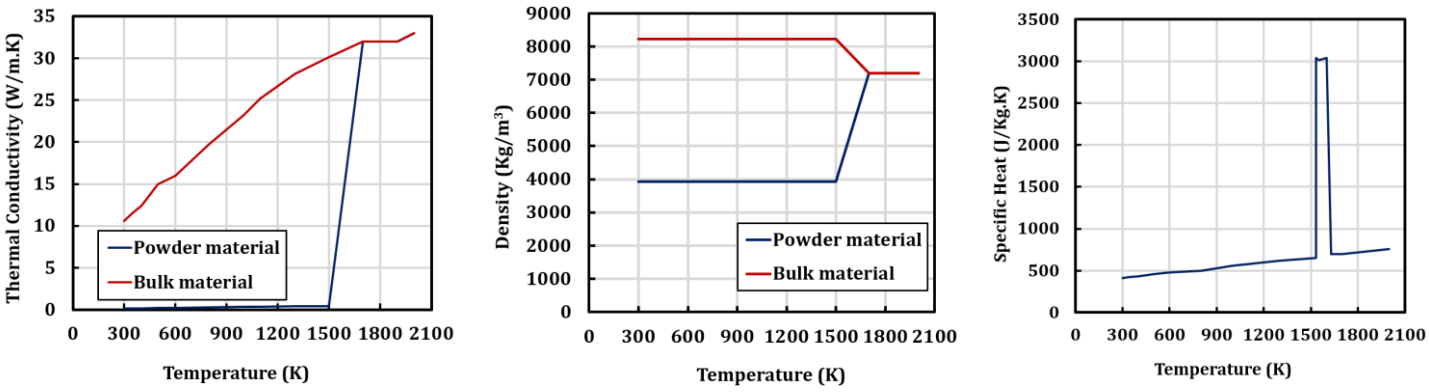

(a) (b) (c)

Fig. 4.3. Temperature properties of bulk and powder material (a) Thermal conductivity (b) Density (c) Specific heat.

4.3.2 Governing equation and boundary conditions

The governing equation of heat transfer can be described as Eq. (4.5) [59]:

$$\rho C_p \frac{\partial T}{\partial t} = \frac{\partial}{\partial x}\left(k_x \frac{\partial T}{\partial x}\right) + \frac{\partial}{\partial y}\left(k_y \frac{\partial T}{\partial y}\right) + \frac{\partial}{\partial z}\left(k_z \frac{\partial T}{\partial z}\right) + Q\ (x, y, z, t) \tag{4.5}$$

where ρ , C_p, k_x, k_y, k_z, T and Q are the density of the material [kg/m^3], specific heat [J/kgK], thermal conductivity [W/mK] of *x*, *y*, and *z* directions, temperature [K], and internal heat generation per unit volume [W/m^3], respectively. The external heat source $I(x, y, z)$ by considering the boundary conditions can be plugged into Eq. (4.5) which generates $Q\ (x, y, z, t)$.

In terms of boundary conditions, the convective heat transfer with the ambient environment based on Newton's law was considered on the top surface of the geometry Eq. (4.6).

$$q_c = -h_c(T_{ext} - T_\infty) \tag{4.6}$$

Above, q_c is heat dissipation, h_c is the heat transfer coefficient [W/m^{2}K], T_{ext} is the geometry temperature, and T_∞ is the ambient temperature (293 K).

In addition, the radiative heat transfer from the top surface of the geometry domain was applied (Eq. (4.7)). The bottom surface of the geometry domain was set as the ambient temperature (293 K).

$$q_r = -\sigma_{sb}\varepsilon({T_{ext}}^4 - {T_\infty}^4) \tag{4.7}$$

Above, σ_{sb} is the Stefan-Boltzmann coefficient [W/m^{2}K^4] and ε is the emissivity coefficient. The boundary conditions can be represented by the following equation [54]:

$$K\frac{\partial T}{\partial n} + h_c(T_{ext} - T_\infty) + \sigma_{sb}\varepsilon({T_{ext}}^4 - {T_\infty}^4) - I = 0 \tag{4.8}$$

where I is the external heat source.

4.3.3 Heat source model calibration

4.3.3.1 Heat source model

A moving heat source with a conical-Gaussian shape was applied for predicting the melt pool dimensions and temperature distributions precisely (Fig. 4.4). The conical-Gaussian heat source is described as [59]:

$$I(x,y,z) = q_0.\exp\left(-2\frac{x^2+y^2}{r_0^2}\right) \tag{4.9}$$

$$r_0(z) = r_e + \frac{z}{H}(r_e - r_i) \tag{4.10}$$

where $I(x,y,z)$, q_0, r_e and r_i are heat intensity distribution, the maximum value of heat intensity, and radius on top and bottom of the heat source profile, respectively.

Based on the thermal energy conservation (Eq. (4.11)):

$$\alpha.P = \int_{-H}^{0}\int_{-\infty}^{\infty}\int_{-\infty}^{\infty} q_0.\exp\left(-2\frac{x^2+y^2}{r_0^2}\right)dxdydz \tag{4.11}$$

where α and P are the laser beam absorptivity and laser power, respectively.

q_0 is derived from Eq. (4.11) and can be calculated (Eq. (4.12)):

$$q_0 = \frac{6\alpha.P}{\pi H(r_e^2 + r_e r_i + r_i^2)} \tag{4.12}$$

where H is the height of the conical-Gaussian heat source.

After replacing q_0 in Eq. (4.9) by Eq. (4.12), the final expression of the intensity distribution can be obtained as follows (Eq. (4.13)):

$$I(x,y,z) = \frac{6\alpha.P}{\pi H(r_e^2 + r_e r_i + r_i^2)}.\exp\left(-2\frac{x^2+y^2}{r_0^2}\right) \quad (4.13)$$

The internal heat generated as a result of the heat input and losses is plugged into Eq. (4.5).

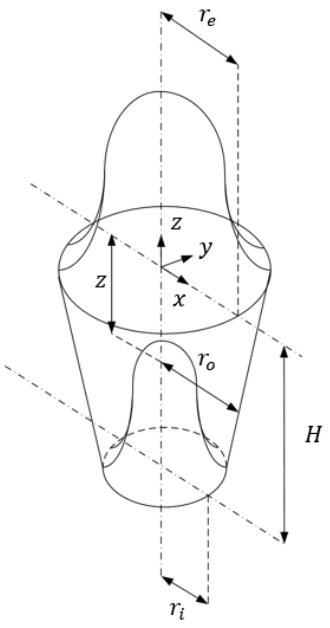

Fig. 4.4. Conical-Gaussian volumetric heat source [88], [89].

4.3.3.2 Calibration procedure

In order to calibrate the numerical model, the heat source parameters such as height (H) and absorption coefficient (α) are altered to minimize the error between the experimental and simulated melt pool dimensions. Since the upper radius of the conical-Gaussian heat source (r_e) is the radius of laser spot size (50 μm), the bottom radius of the heat source has a limited range to be varied. In addition, based on Eq. (4.12) and the calibration iteration, it is found that a lower radius of the heat source r_i does not have a significant influence on the melt pool depth where it has a slight effect on melt pool width, so it has been fixed in the chosen value (30 μm). It is also noted that the height of the conical-Gaussian heat source (H) is the most important parameter and numerical results show that as

the height of the heat source is increased, the width of the melt pool decreases. In order to compensate for the reduction in melt pool width, the absorption coefficient has been modified for acquiring more accurate melt pool shapes. It is realized that the absorption coefficient has a significant effect on the melt pool width and depth at the same time.

Fig. 4.5 demonstrates a flow chart of the procedure implemented for calibrating the heat source model, where W_{ex}, W_{sim}, D_{ex} and D_{sim} are the experimental melt pool width, predicted melt pool width, experimental melt pool depth, and predicted melt pool depth, respectively. The maximum acceptable deviation of model predictions for the melt pool width and height is identified as ε_1 and ε_2, respectively which are set to 15%. As the flow chart shows, in the first step, the initial values of height of heat source and absorption coefficient are selected, and based on those values numerical simulation was carried out. Due to the complexity of the laser powder-bed fusion process, researchers use a lot of underlying assumptions to capture the model accurately [32], [81]. As a result, numerical results have some deviations from experimental and the current studies show a ±30% as a fair and acceptable range [90], [91]. By comparing the experimental and numerical results of melt pool depth and width, the values of the absorption coefficient and height of heat source are modified such that the difference between the numerical with experimental ones is within an acceptable range.

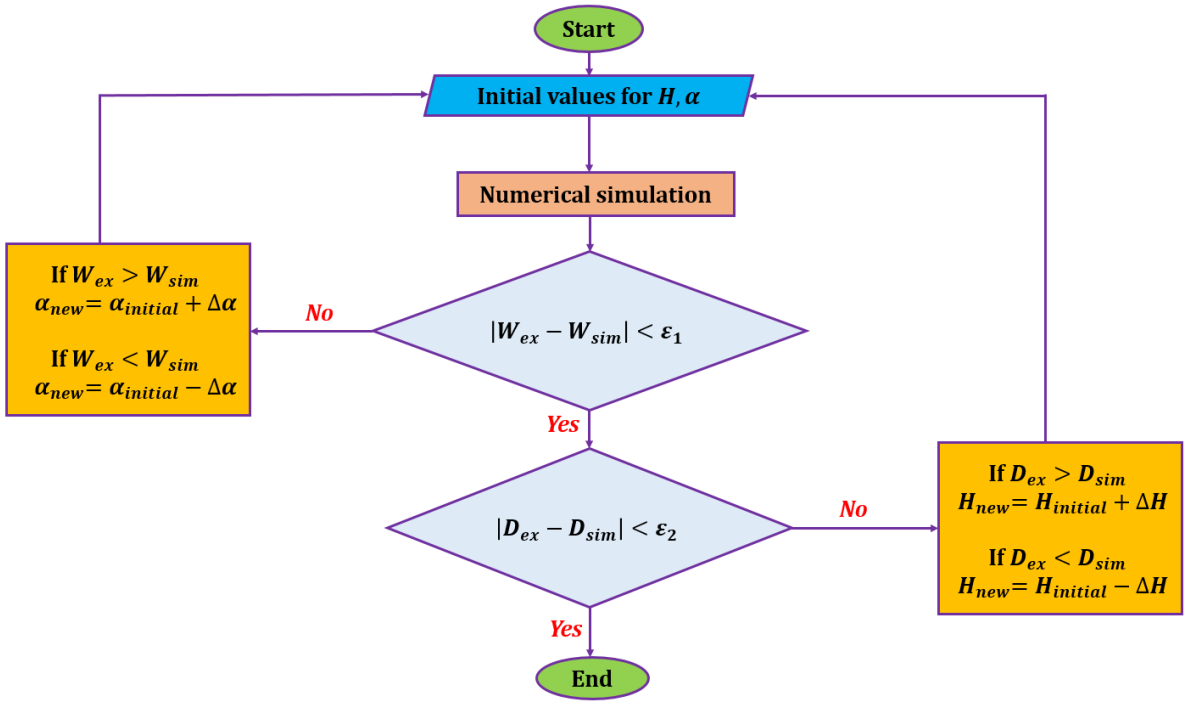

Fig. 4.5. Flow chart showing the calibration procedure for the heat source.

4.3.4 Experimental measurements of the melt pool, calibration, and validation results

Based on Section 4.3.3, the heat source model was calibrated using the power and scanning speed values listed in Table 4.1.

Validation of the melt pool dimensions with experimental measurements is done in such a way that melt pool depth and width below the powder layer are compared with experimental results [56], [59]. Evaporation and shrinkage of the powder layer are ignored due to modeling complexities. Fig. 4.6 illustrates that the experimentally measured melt pool geometries are in good agreement with the numerical results. The average percentage differences between the simulation results and experimental ones for the melt pool depth and width are 13% and 6%, respectively. Based on the literature, it has been reported that the absorbed energy density is proportional to the ratio of the laser power to the root of velocity ($\frac{P}{\sqrt{V}}$), where P is laser power and V is scanning speed [59]. It is realized that the absorption coefficient and height of the conical-Gaussian heat source has a linear relationship with the $\frac{P}{\sqrt{V}}$. The physical reason behind this is due to the fact that as the energy density increases, melt pool depth becomes larger due to higher heat penetration to the powder-bed. On the other hand, by increasing the energy density the material tends to absorb more energy [92]. Therefore, the absorption coefficient and the height of the conical-Gaussian heat source should be adapted based on the $\frac{P}{\sqrt{V}}$. As a result, a higher $\frac{P}{\sqrt{V}}$ will cause a higher absorption coefficient and a larger height of the conical-Gaussian heat source.

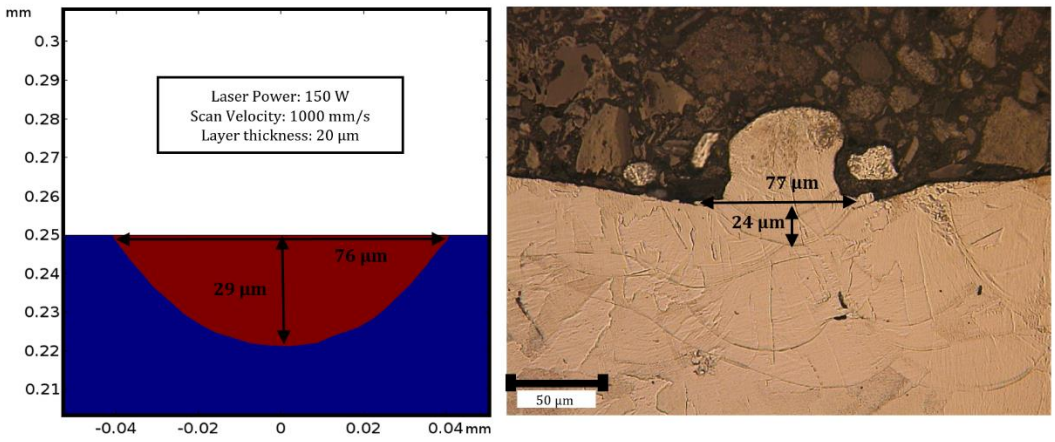

(a)

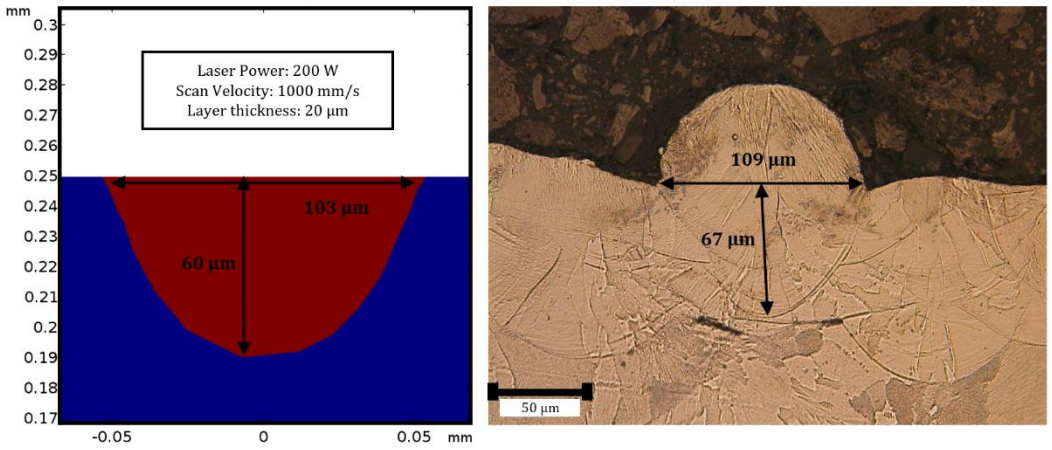

(b)

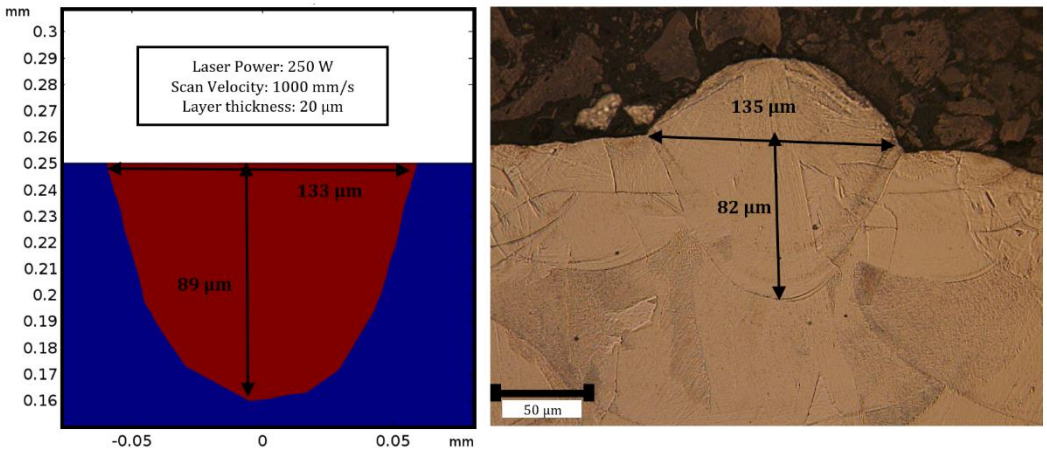

(c)

Fig. 4.6. Experimental and numerical results of melt pool geometries with different process parameters (a) Power: 150 W (b) Power: 200 W (c) Power: 250 W.

Empirical equations Eq. (4.14), and Eq (4.15) show the relationship between the $\frac{P}{\sqrt{V}}$, the height of the conical-Gaussian heat source and absorption coefficient which were derived based on the calibration of the heat source with experimental results. It should be mentioned that this empirical equation would be valid for the energy density within the range of 4.74 to 7.90 ($W/\sqrt{mm/s}$) which falls within the conduction mode of the melt pool and ensures near full dense parts.

$$\alpha = a_1 \frac{P}{\sqrt{V}} + b_1 \tag{4.14}$$

$$H = a_2 \frac{P}{\sqrt{V}} + b_2 \tag{4.15}$$

where $P\ [W], V\left[\frac{mm}{s}\right], H[\mu m]$ and α are the laser power, scanning speed, the height of conical-Gaussian heat source, and absorption coefficient, respectively. a_1, a_2, b_1, and b_2 are also parameters that will be determined by experimental results (Table 4.2).

The porosity of the powder and the convection heat transfer of the melt pool has a significant increase in heat penetration to the powder bed. By doing the calibration procedure the height of the conical Gaussian heat source have been found to be in the range of 50 μm to 100 μm for the energy density range of 4.74 to 7.90 ($W/\sqrt{mm/s}$).

Table 4.2. The coefficient in the empirical equation for deriving absorption coefficient and height of heat source.

a_1	b_1	a_2	b_2
0.126	-0.297	15.82	-24.99

4.3.5 Effect of process parameters on melt pool dimensions

Experimental single tracks with the various range of laser scanning speeds and power were printed, cross-sectioned and polished to measure the melt pool depth and width.

The results show that by increasing the laser power from 150 W to 250 W while keeping other process parameters constant, the depth and width of the melt pool will also elevate whereas, increasing the scanning speed from 800 to 1300 mm/s will cause a decrease in the melt pool dimensions. Fig. 4.7 shows that with the increasing laser power from 150 W to 250 W, the depth and width of the melt pool will increase from 26 μm to 82 μm and 88 μm to 129 μm, respectively. Fig. 4.8 demonstrates the effect of scanning speed on melt pool dimensions. With increasing scanning speed from 800 mm/s to 1300 mm/s, the melt pool depth and width will decrease from 72 μm to 34 μm and 127 μm to 90 μm, respectively. This phenomenon happens due to a changing energy density, which is fluxing into the material. Therefore, as mentioned previously, higher laser power and a lower scanning speed will result in a higher energy density, which is absorbed by the material, consequently, the melt pool geometries including the melt pool depth and width will be increasing. The same scenario will also happen when a lower energy density is given to the material. Therefore, a lower $\frac{P}{\sqrt{V}}$ will cause smaller melt pool dimensions. Fig. 4.9 shows the effect of $\frac{P}{\sqrt{V}}$ on the melt pool

dimensions. It is found that by increasing the $\frac{P}{\sqrt{V}}$ from 4.74 to 7.9, the melt pool depth and width will increase from 26 µm to 82 µm and 88 µm to 129 µm, respectively.

Experimental results demonstrate that increasing scanning speed from 800 [mm/s] to 1300 [mm/s] will lead to a reduction in the melt pool depth by 52%.On the other hand, decreasing the laser power from 250 [W] to 150 [W] causes a reduction in the melt pool depth up to 68%. Therefore, it can be concluded that the laser power has a stronger influence on the melt pool dimensions compared to the laser scanning speed [93].

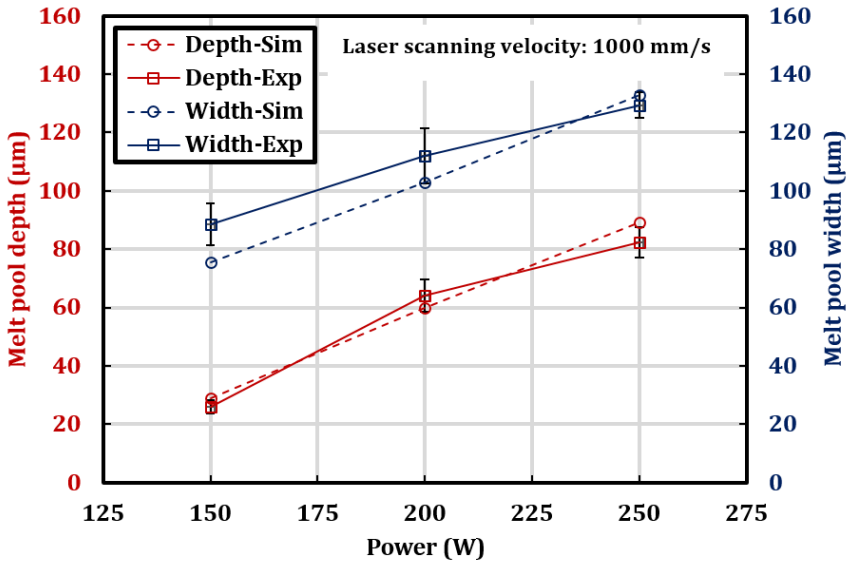

Fig. 4.7. Effect of laser power on melt pool depth and width.

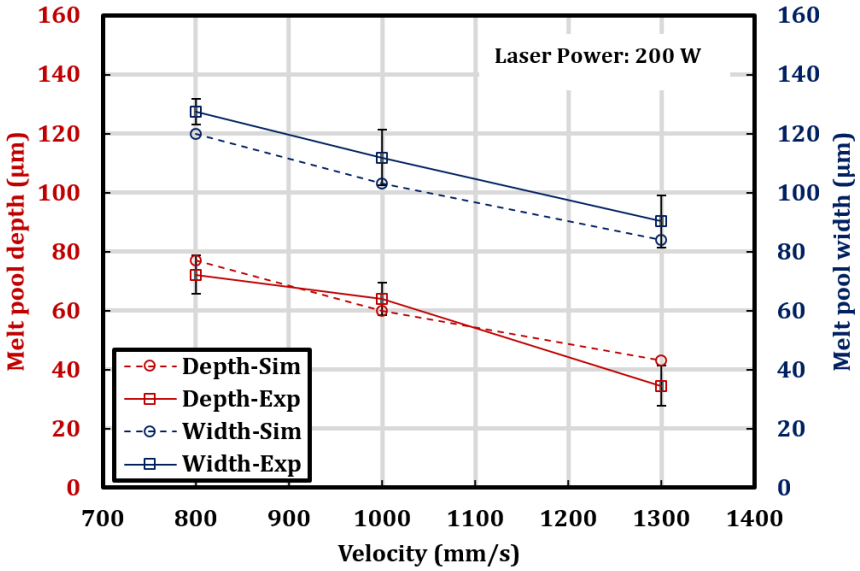

Fig. 4.8. Effect of scanning speed on melt pool depth and width.

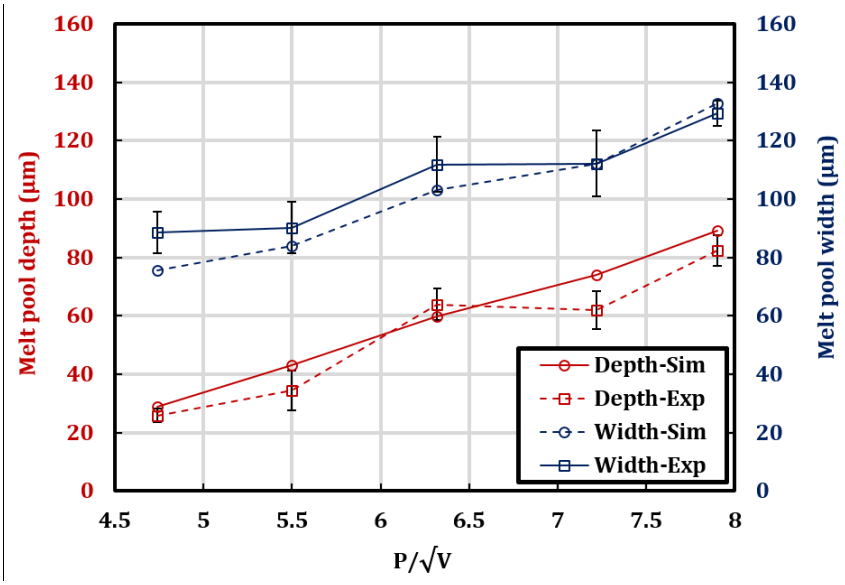

Fig. 4.9. Effect of linear energy density on melt pool depth and width.

4.3.6 Temperature distribution

In order to derive temperature distribution along the X and Y-axis of the melt pool, two paths have been identified on the top of the powder surface where the laser heat source is applied (Fig. 4.10). Fig. 4.11 demonstrates the effect of different scanning speeds on the temperature distribution. By increasing the scanning speed from 1000 mm/s to 1600 mm/s, the laser energy input to the material

will be decreased, which results in decreasing the peak temperatures. On the other hand, the temperature distribution in the X direction illustrates that the maximum temperature occurs in the melt pool front. In addition, the temperature distribution along Y-axis clearly shows the Gaussian distribution of the laser heat source.

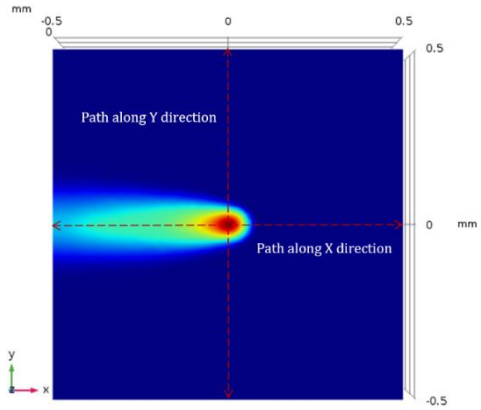

Fig. 4.10. Top view of moving laser heat source with identifying two paths along with X and Y directions.

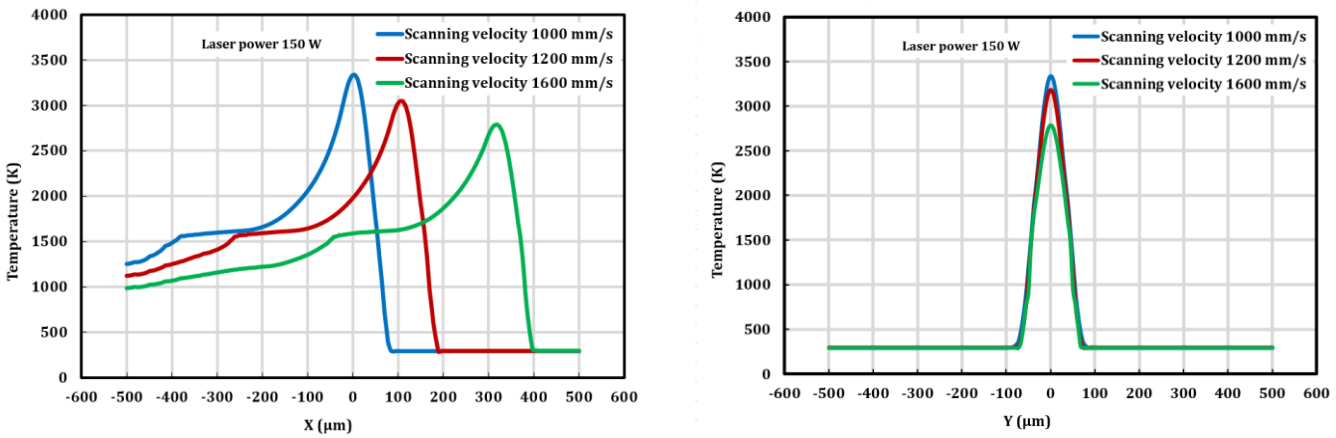

(a) (b)

Fig. 4.11. Effect of laser scanning speed on temperature distribution (a) along X direction (b) along the Y direction.

4.3.7 Temperature gradient

Due to the fast solidification within LPBF [94], the temperature gradient and cooling rates play a crucial role in predicting the microstructure, grain orientation, and growth within the melt pool. In order to extract temperature history from the numerical results, several points were set in the z-axis from the top of the powder layer towards the bulk material at 5 µm intervals as shown in Fig. 4.12.

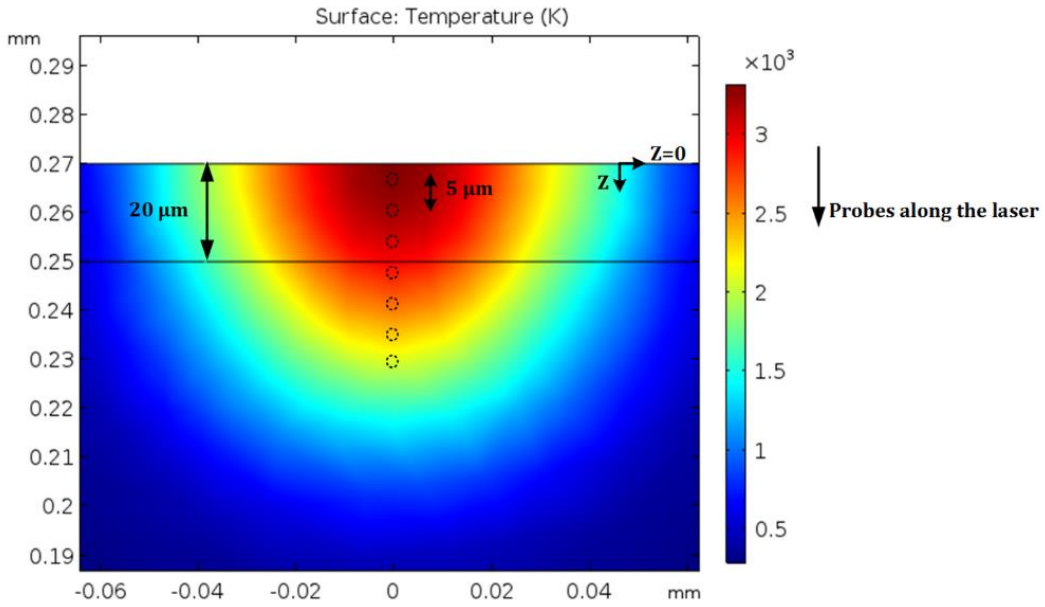

Fig. 4.12. Probes along melt pool depth and model predicted the temperature distribution in melt pool cross-section normal to the laser movement direction.

For obtaining temperature gradient within the melt pool at the specific time from 20 µm under the surface of powder (Z=20 µm) to 150 µm below the surface, the temperature distributions along the Z direction for different scanning speeds are extracted. Fig. 4.13 (a) shows that the temperature will drop from the powder to the bulk material due to the higher thermal conductivity of the bulk region compared to the powder material. Moreover, the heat source is decaying linearly along the Z direction. The results show that a higher scanning speed leads to a reduction in the temperature gradient within the melt pool. This could be due to providing less energy density input to the material so that the peak transient temperature will decrease. As a result, the temperature difference from the top to the bottom surface will be decreasing which means that by increasing the scanning speed, the temperature gradient will be reduced. In addition, it has been found that the maximum temperature gradient for different scanning speeds, 1000 mm/s, 1200 mm/s, 1600 mm/s is 69 K/µm, 63 K/µm, and 52 K/µm, respectively, which has occurred at 52 µm below the powder surface, close to the interface of solid and liquid phase within the melt pool (Fig. 4.13 (b)).

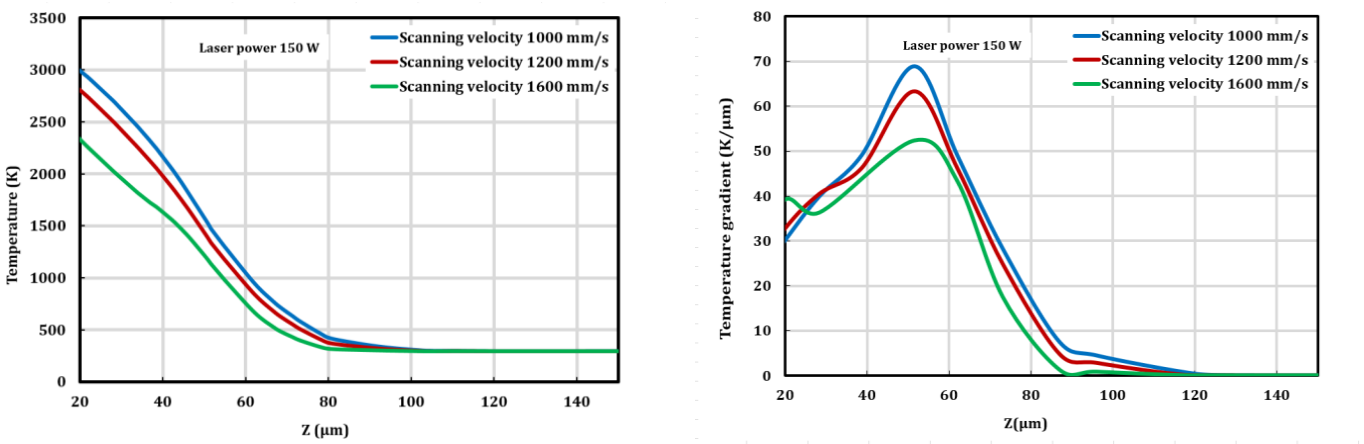

(a) (b)

Fig. 4.13. (a) Temperature distribution along build direction (b) Temperature gradient within the melt pool.

4.3.8 Cooling rate

Fig. 4.14 shows the effect of scanning speed on the transient temperature corresponding to different points within the melt pool. Increasing the scanning speed leads to less amount of energy density that fluxes into the material. Therefore, peak temperatures will be decreasing with increasing the scanning speed. On the other hand, by moving down from the powder to the bulk material along the Z direction, the temperature peak will be reduced. This is happening firstly because the conical-Gaussian heat source is decaying linearly along the Z direction. Secondly, by moving from the powder to the bulk material, the heat conductivity will increase drastically such that heat will dissipate more into the bulk regions, which causes the cooling rate to increase. Fig. 4.14 depicts slope changing when the temperature is below the melting point due to the phase change. In addition, the cooling rate has been derived from different points, which are located within the melt pool, and the effect of laser power on the cooling rate is investigated (Fig. 4.15). It has been found that by increasing the laser power, the cooling rate will be increased. It is attributed to the fact that as the laser power is increased, a higher energy density is given to the material so that the peak transient temperature will be increasing. Therefore, the maximum cooling rate will be increased due to drastically decreasing temperatures. The results illustrate that the maximum cooling rate for a different range of laser power, 150 W,200 W, and 250 W is 1.7×10^7 K/s, 2.5×10^7 K/s, and 3.1×10^7 K/s which occurs at the top surface of the melt pool (Z=20 μm).

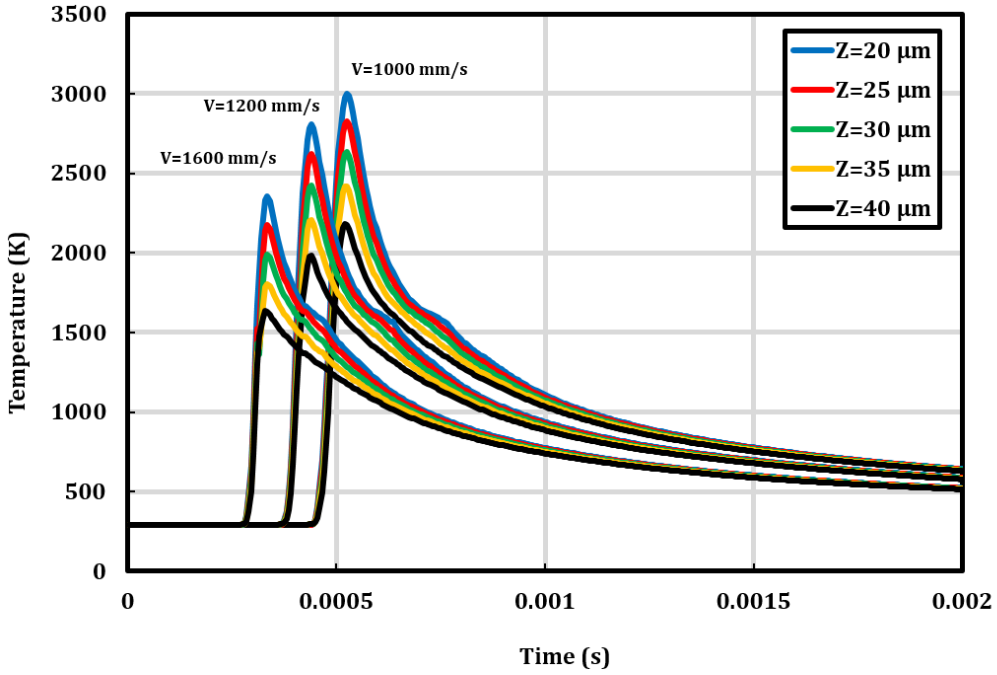

Fig. 4.14. The model-predicted temperature history of probes from powder to the bulk region with fixed laser power of 150 W and different laser scanning speeds of 1000 mm/s, 1200 mm/s, and 1600 mm/s.

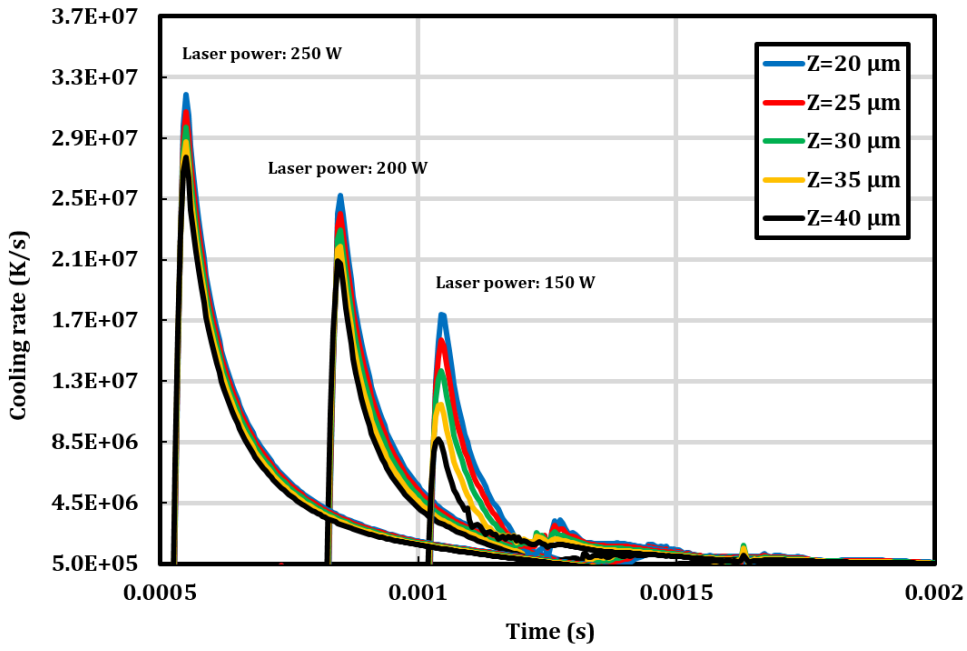

Fig. 4.15. Model-predicted cooling rate for different probes within melt pool with fixed scanning speed 1000 mm/s and varying laser power of 150 W, 200 W, and 250 W.

4.3.9 Experimental validation of cooling rate

Fig. 4.16 (a) displays the simulated melt pool temperature distribution of a produced single track using the laser power of 200 W, the scan speed of 1000 mm/s, and the layer thickness of 20 μm with four points located in the middle of the melt pool with different depths from the surface of the substrate. Fig. 4.16 (b-c) shows low and high magnification Scanning Electron Microscope (SEM) images from the cross-sectioned single track deposited with the same process parameters. More in detail, the cellular structure of the solidified material is shown in Fig. 4.16 (c) where primary cell spacing was measured to be around 320 nm. These fine features in the microstructure are a result of the rapid solidification of molten metal during LPBF [95]–[97]. It is well known that higher cooling rates significantly reduce the feature size of the solidified microstructure. Here in the LPBF, both the high-temperature gradient and solidification rate result in outstandingly high cooling rates [95], [98]. Primary spacing (λ_1) of either cells or dendrites in the microstructure of Ni-base superalloys is directly related to the cooling rate with an empirical Eq. (4.16) reported by [98]:

$$\lambda_1 = 97\left(\dot{T}\right)^{-0.36} \tag{4.16}$$

where $\dot{T}$ is the cooling rate of the interface of solid/liquid during solidification. Considering λ_1 to be around 0.32 μm (Fig. 4.16 (c)), the cooling rate can be calculated ~ 7.82 ×10^6 K/s. On the other hand, a maximum value for the cooling rate related to the probe close to the melt pool boundary has been calculated to be around ~ 8.82 ×10^6 K/s which is very close to what was observed from the obtained cooling rate from the primary cell spacing.

A detailed effect of energy density on primary dendrite spacing is demonstrated in Fig. 4.17. It is found that simulation results are very close to experimental ones for different process parameters and predict dendrite spacing accurately. Increasing the energy density leads to higher cooling rates which cause smaller primary dendrite spacing. Since the SEM images extracted from each grain may be observed from the projection of the image derived from different cutting planes, there were some variations of primary dendrite spacing for each specimen. However, the simulation results were within the range of experimental results.

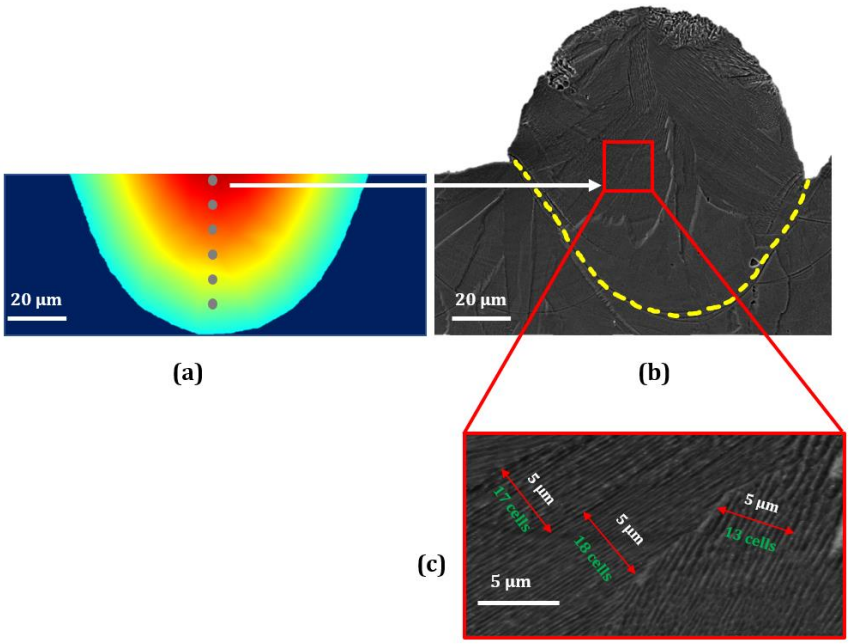

Fig. 4.16. (a) Simulated temperature distribution in the melt pool area, (b) low magnification, and (c) high magnification SEM image from a cross-section of single track deposited by laser power of 200 W and scanning speed of 1000 mm/s.

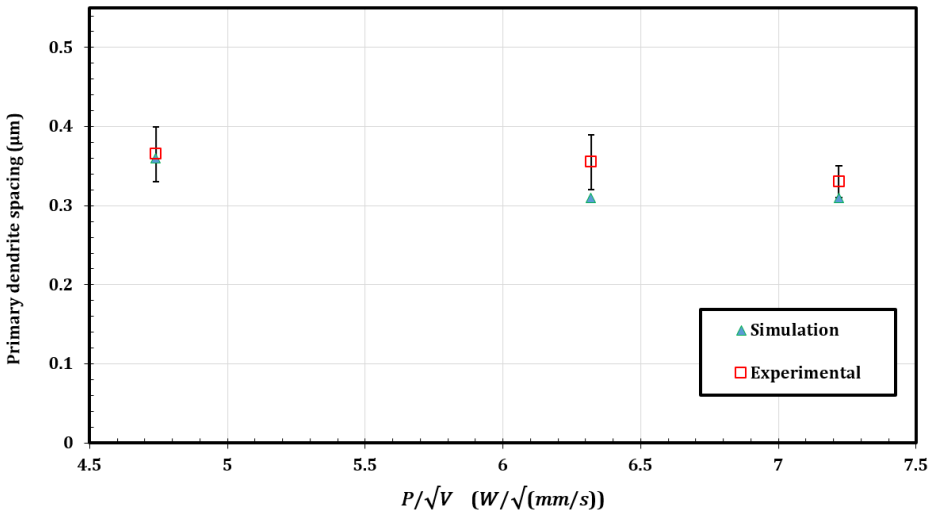

Fig. 4.17. Effect of energy density on the primary dendrite spacing.

Sensitivity analysis on heat source parameter and absorption coefficient is done for confirming the fact that selecting the most optimum parameters for the Conical Gaussian heat source and absorption coefficient results in a more accurate prediction of cooling rate and cell space. These results confirm the strength and accuracy of the model.

The sensitivity plot for various heat source parameters on the cooling rate with fixed process parameter of laser power of 150 W and scanning speed of 1000 mm/s at the interface of solidus and liquidus (Z=40 µm) is shown in Fig. 4.18. It clearly shows that with implementing height of 50 µm and the absorption coefficient of 0.3, the cooling rate is 8.82 $\times 10^6$ K/s which is comparable to the experimental results derived from Eq. (4.16). Otherwise, the cooling rate would be either very higher or lower, which is not close to the experimental results. Therefore, by implementing the calibrated heat source model, the numerical results will predict the microstructure within the melt pool more precisely.

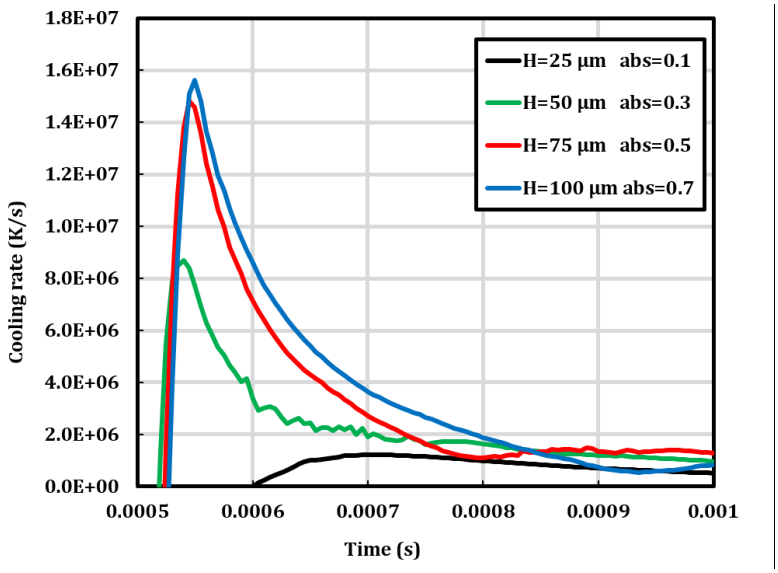

Fig. 4.18. Sensitivity plot of heat source parameter on cooling rate with a laser power of 150 W and scanning speed of 1000 mm/s.

4.4 Micro/mesoscale modeling (multi-track multi-layer simulation)

In order to capture the temperature history of each layer during the build-up process, multitrack-multilayer modeling of LPBF is conducted by using Star CCM+ software (Fig. 4.19). The procedure is in such a way that firstly, the volumetric heat source is applied on top of material assigned to powder properties. Then, after scanning (X-direction scanning pattern) the whole deposited layer, the

properties of the powder are transformed into solid properties and another new powder layer is added on top. Therefore, this process continues until a limited number of layers. In addition, the delay time between spreading each powder layer is considered. Table 4.3 shows the parameters are used for modeling.

Table 4.3. Process parameters used for multitrack-multilayer simulation.

Laser power (W)	Scanning speed (mm/s)	Layer thickness (µm)	Hatch distance (µm)
150	1000	20	100

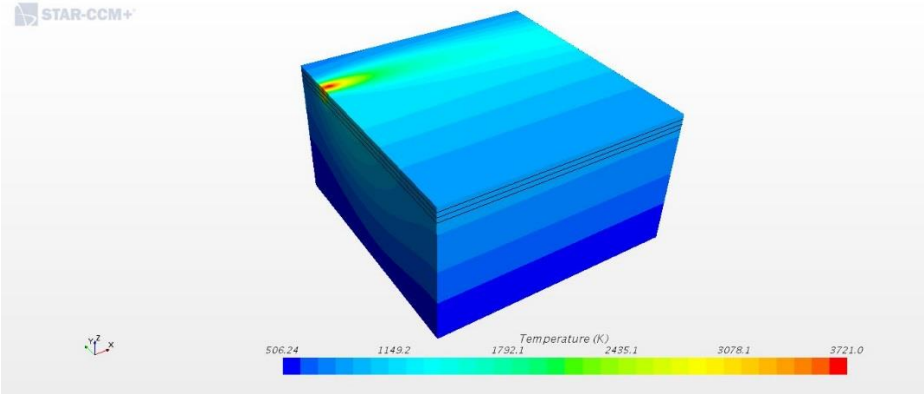

Fig. 4.19. Multi-track multi-layer simulation.

The temperature history of the point on top of the first layer during the build-up process is shown in Fig. 4.20. The results show that by moving up to the next layer during the building process temperature peak is decreasing. In addition, Fig. 4.21 illustrates more detail of temperature history during scanning the first layer. It can be seen that some ripples in the plot demonstrate the effect of the hatch distance of the laser track during the scanning layer.

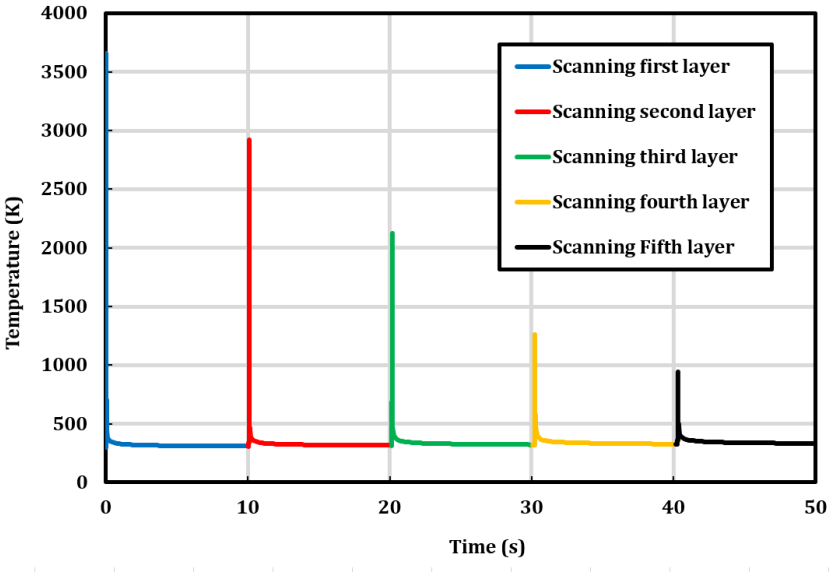

Fig. 4.20. The temperature history of the point on top of the first layer during the building process.

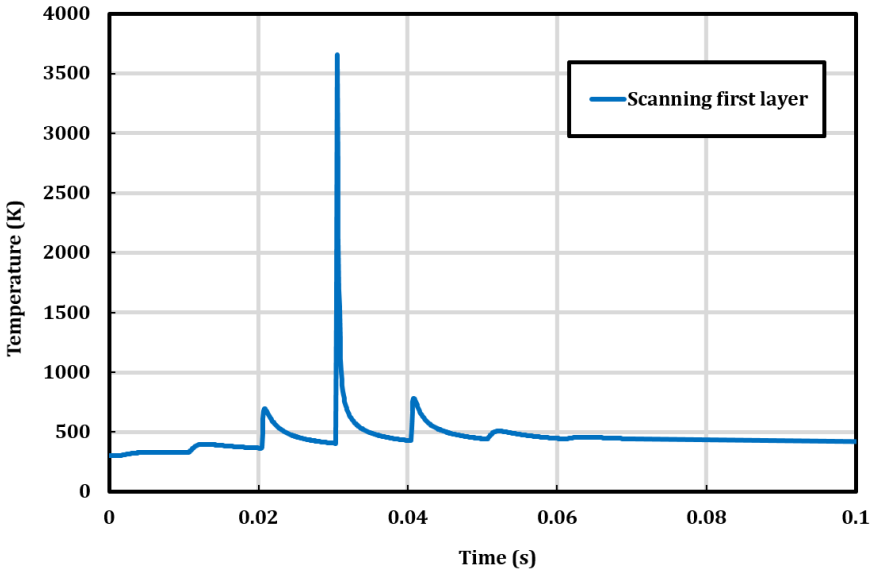

Fig. 4.21. The temperature history of the point on the first layer.

4.5 Summary

In this work, experimental and numerical investigations of single tracks of Hastelloy X made by LPBF were carried out and the melt pool dimensional features were measured experimentally. The main conclusions can be summarized as follows:

1- Based on the experimental results, the heat source model was calibrated and the proposed empirical equations show the relationship between the energy density ($\alpha = a_1 \frac{P}{\sqrt{V}} + b_1, H = a_2 \frac{P}{\sqrt{V}} + b_2$), the height of the heat source and the absorption coefficient. However, these empirical equations are only valid for the specific range of energy density that provides the conduction mode of the melt pool.

2- The simulated results for the melt pool dimensions show a good agreement with the experimental data. The percentage difference between the simulated and experimental melt pool depth and width results is around 13% and 6%, respectively.

3- The influence of laser power and scanning speed on the melt pool depth and width was investigated. By decreasing the laser power from 250 W to 150 W in fixed scanning speed (1000 mm/s), the melt pool depth and width decrease 68% (82 µm to 26 µm) and 32% (129 µm to 88 µm), respectively. On the other hand, by increasing the laser scanning speed from 800 mm/s to 1300 mm/s in fixed laser power (200 W), the melt pool depth and width reduce 53% (72 µm to 34 µm) and 29% (127 µm to 90 µm), respectively. It is concluded that the effect of laser power on the melt pool geometry is more dominant than the scanning speed.

4- It is found that the cooling rate increases with increasing laser power. The results illustrate that the maximum cooling rate is 3.1×107 K/s corresponding to a laser power of 250 W which occurs at the top surface of the melt pool.

5- On the other hand, with increasing the scanning speed, the temperature gradient decreases significantly. Moreover, the maximum temperature gradient of 69 K/µm is achieved by implementing the scanning speed of 1000 mm/s which occurs at 52 µm below the powder surface, close to the interface of solid and liquid phase within the melt pool.

6- The effect of energy density on the primary cell spacing is also studied and numerical results of cooling rates are validated with experimental results. The results show that dendrite cell spacing decreased from 0.365 to 0.330 µm by increasing energy density from 4.74 to 7.22 ($W/\sqrt{mm/s}$).

7- The sensitivity analysis is also carried out which indicates that by implementing the calibrated heat source model, the cooling rate and estimated primary dendrite spacing are predicted more precisely.

8- Moreover, a multi-track multi-layer simulation was done and the temperature history of each layer was derived. The results showed that by increasing the number of layer thicknesses, the peak temperature of previous layers will be decreasing.

In the future, the effect of layer thickness on melt pool dimensions and temperature distribution can be investigated. In addition, it is worth investigating the effect of hatch distance on the temperature distribution and porosity of the final printed parts.

Chapter 5. Micro/Mesoscale Modeling Application - The Effects of Thin-wall Thickness on Melt Pool Dimensions and Developing Process Map for Laser Powder-bed Fusion of Hastelloy X*

5.1 Introduction

In this chapter, a three-dimensional (3D) heat transfer model is developed to investigate the influence of the thickness of the printed thin-walls on melt pool dimensions and temperature distribution. The results indicate that the single track simulation can predict the melt pool dimensions accurately and the calibrated model can be extended to the multi-track simulation for investigating the effect of thin-wall thicknesses on melt pool geometries. The simulation results demonstrate the evolution of melt pool geometries during the process. Due to the existence of heat accumulation during the process, decreasing the thicknesses of the thin-walls leads to enlarging the melt pool width significantly. The validation of the simulation results showed the high capability of the model in predicting the transient temperature profile and melt pool geometries. The percentage difference between simulated and experimental melt pool width for thin-wall thicknesses 0.5 mm, 0.75 mm, and 1 mm are 7%, 7%, and 11%, respectively. Lastly, a process map has been provided to guide the selection of process parameters for printing thin-wall structures.

The melt pool formation and solidification during laser scanning of the powder material are one of the most studied topics in LPBF [93], [99], [100] as it directly affects the part density [99], microstructure [101], and strength of the printed parts [102]. In addition, the LPBF input process parameters have a significant effect on the melt pool shape. Gunenthiram et al. [99] investigated the effect of various process parameters on melt pool instabilities. By utilizing a high-speed camera they concluded that the vaporization during the process had a considerable influence on the instabilities of the process. Keshavarzkermani et al. [93] studied the effect of laser energy density (LED) on melt pool formation and its results on the final microstructure of printed parts. They found out that finer cell structure in the melt pool was obtained by higher laser power due to its higher cooling rate. Staub et al. [103] investigated the effect of using high laser power on residual stress of the final printed parts and its correlation with melt pool shapes. Their results showed that larger and flatter melt pool

* A similar version of this chapter is going to be submitted as: Shahriar Imani Shahabad, Usman Ali, Zhidong Zhang, Ali Keshavarzkermani, Reza Esmaeilizadeh, Ali Bonakdar, Ehsan Toyserkani, The Effects of Thin-wall Thickness on Melt Pool Dimensions and Developing Process Map for Laser Powder-bed Fusion of Hastelloy X

dimensions induced higher residual stress in the fabricated parts due to the larger width of melt pools in comparison to deeper and thinner melt pools. Moreover, Patel and Vlasea [104] defined three regions for melting mode including conduction, transition, and convection modes. In their work, a normalized processing diagram was identified for accelerating the optimization of the process parameters.

Although experimental works have studied various aspects of the melt pool geometries in LPBF, they are time-consuming and costly [4]. Numerical modeling techniques such as Finite Element (FE) analysis provide an effective approach for predicting the influence of input process parameters on melt pool characteristics and transient temperature during the process. Obidigbo et al. [100] investigated the feasibility of printing Invar and found that by implementing a common scanning strategy, the melt pool shapes behave similarly to other common Nickel-based alloys. Yuan et al. [105] investigated the laser scanning speed influence on melt pool formations and categorized different regions of scanning speed based on the stability of melt pool formation. Shahabad et al. [106] studied the effect of process parameters (laser power and speed) on melt pool dimensions and concluded that laser power had a more dominant effect on the melt pool geometries. Huang and Zhang [32] investigated the effect of powder layer density and showed that the maximum melt pool temperature increases by decreasing the density of the powder layer. Li et al. [107] studied the effect of laser power and scanning velocity on melt pool dimensions and found that the width, depth, and length of the molten region had a proportional relationship with laser power which is consistent with other studies [57], [108]. Zhang et al. [59], [109] conducted a comprehensive study on various heat source models for predicting melt pool shape. The effect of process parameters (laser power and scanning speed) was studied, and they proposed and validated a novel heat source for predicting melt pool shape accurately. Moreover, their results showed an insignificant effect of layer thickness on melt pool geometries.

In addition to the laser power and scanning speed, part geometry also plays an important role in the melt pool dimensions, formed microstructure, and mechanical behavior of printed parts. Leicht et al. [110] studied the effect of rib thickness and build angles on the microstructure of 316L parts. They concluded that 0.4 mm and 45˚ build angles as critical thickness and build angle for avoiding large elongated grains. Similarly, Liang et al. [111] found that smaller geometric sizes (less than 1 mm) resulted in poor cooling conditions and affected the elastic modulus and hardness.

To the best knowledge, there is a lack of research on the effect of part geometry on melt pool dimensions. Thus, in this study, the effects of the thin-wall thickness on the melt pool dimensions have been investigated. To this end, a high fidelity numerical model to predict the influences of input process parameters and part geometries on the melt pool dimensions was developed. Then, several Hastelloy X thin-walls were printed with different thicknesses to assess the influence of part geometries on melt pool shapes and microstructures experimentally. The results show melt pool evolution and melt pool stability are parameter and geometry dependent in a multi-track LPBF process. Therefore, a decrease in the thicknesses of the thin-walls results in increasing the melt pool width substantially. Lastly, the process map is developed which is a guide for choosing the proper range of process parameters based on the dimensions of the thin-wall thicknesses for printing the high-quality parts.

5.2 Material and method

To investigate the influence of part geometry on melt pool shapes, three thin-walls of different thicknesses (0.5 mm, 0.75 mm, 1 mm) with three repetitions were printed as shown in Fig. 5.1. EOS M290 machine (EOS GmbH, Krailling, Germany) printed all samples using stripe scanning strategy without any rotation on each layer with a laser power of 200 W, scanning speed of 1000 mm/s, hatch distance of 90 µm, and layer thickness of 40 µm. Hastelloy X powder was selected for this study with a size distribution of D10 < 15.5 µm, D50 < 29.3 µm and D90 < 46.4 µm [85]. Table 5.1 shows the chemical composition of the Hastelloy X powder used in the current investigation. To analyze the morphology of the powder distribution, Zeiss ULTRA Plus (Carl Zeiss Microscopy GmbH, Jena, Germany) Scanning Electron Microscopy (SEM) was used (Fig. 5.2). Besides, for capturing the grain size and Electron Backscatter Diffraction (EBSD) images, VEGA3 (TESCAN ORSAY HOLDING, Kohoutovice, Czech Republic) SEM was utilized.

Table 5.1. Hastelloy X powder chemical composition (in wt. %) [112].

C	Si	Cr	Mn	W	Ti	Cu	Fe	Mo	Co	Al	Ni
<0.1	<1	21.75±1.25	<1	0.6±0.4	<0.15	<0.5	18.5±1.5	9±1	1.5±1	<0.5	balance

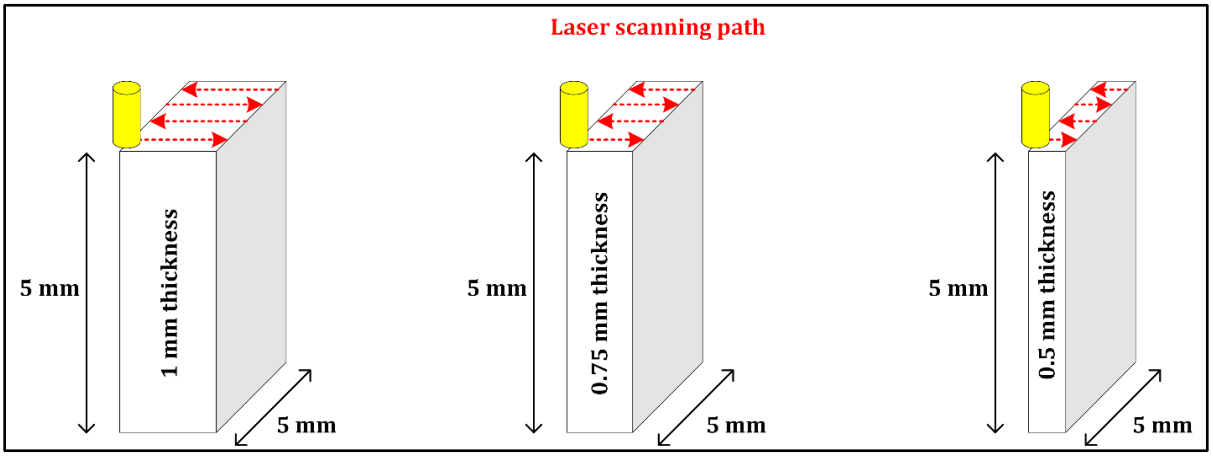

Fig. 5.1. Geometry dimensions of thin-walls.

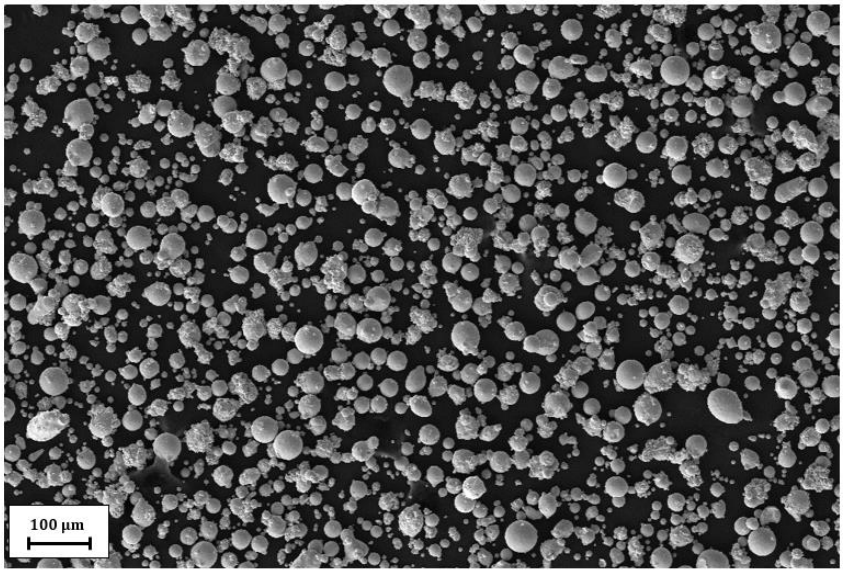

Fig. 5.2. Powder distribution of Hastelloy X material [106].

The printed parts were mounted, polished, and etched using Glyceregia solution for preparing the samples to measure melt pool dimensions. The resulting melt pool geometries were obtained using a Keyence VK-X250 confocal laser microscope (Keyence Corporation, Osaka, Japan).

5.3 Finite element (FE) modeling

Finite element (FE) analysis was conducted to investigate the effect of part geometries on temperature distribution and melt pool evolution during the LPBF process. A three-dimensional transient thermal model was developed using commercial software COMSOL Multiphysics®. Irreversible phase

change transformation, anisotropic thermal conductivity, and volumetric heat source were considered to provide a more accurate prediction of temperature profile and melt pool geometries during the process. The advantages of using anisotropic thermal conductivity and volumetric heat sources have been outlined in a previous work by the authors [59]. The procedure of developing the FE model is described in the following sections.

5.4 Model geometry

Two different LPBF models were developed for the (a) single-track and (b) multi-track simulations as shown in Fig. 5.3. The smaller domain size (1 mm × 0.5 mm × 0.5 mm) with half symmetry was used for capturing the melt pool and calibration of the heat source model in the single-track simulation process. On the other hand, thin-walls with the same geometry as printed parts (5 × 5 × 0.5 mm, 5 × 5 × 0.75 mm, and 5 × 5 × 1 mm) were modeled for simulating the multi-track LPBF process. Calibrated and validated parameters from the single-track simulations were used to model and validate the multi-track simulations.

A uniform cuboid mesh was created for both models in the domain with a maximum element size of 20 µm. The number of elements for the single-track model and multi-track model is 7395 and 25500. The top layer in Fig. 5.3 shows the powder layer with a thickness of 40 µm as a continuous domain.

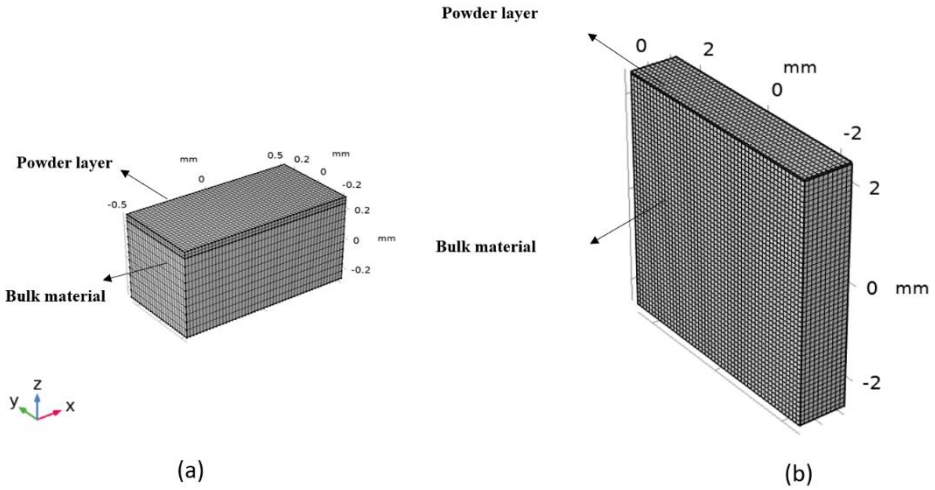

Fig. 5.3. Meshed geometry model, a) Single-track model, b) Example of the multi-track model.

5.5 Material properties

In this model, thermal conductivity, specific heat, and density of Hastelloy X were taken as functions of temperature as discussed below.

5.5.1 Thermal conductivity

One of the most crucial physical properties required for conducting thermal analysis is the thermal conductivity of the powder and bulk material. It is realized that the thermal conductivity of the bulk and powder material is extremely different from each other. Sih and Barlow [87] derived a relationship (Eq. (4.1)) considering the powder compaction factor, particle shapes, and other parameters related to the powder layer, which has a significant effect on the thermal conductivity. The equation of thermal conductivity is presented in Section 4.3.1 of Chapter 4.

5.5.2 Specific heat capacity

The latent heat of fusion plays a crucial role in defining the specific heat capacity of the material. In other words, the phase transformation from powder to liquid requires heat absorption for overcoming the heat capacity of the material and is called the latent heat of fusion. The apparent heat capacity method [113] is utilized for considering the latent heat of fusion during the melting process. The equation of specific heat (Eq. (4.4)) is described in Section 4.3.1 of Chapter 4 [106].

5.5.3 Density

Powder-bed compaction density is acquired experimentally as described in [86]. By considering the powder compaction and the existence of porosities between particles, the density of the powder layer is obtained. The equation of the density (Eq. (4.3)) is presented in Section 4.3.1 of Chapter 4 [106].

5.6 Heat transfer governing equation and boundary conditions

The governing equation of heat transfer (Eq. (4.5)) is based on conduction Fourier's law which is described in Section 4.3.2 of Chapter 4 [16]:

To compensate for the effect of fluid convective heat transfer, anisotropic enhanced thermal conductivity is considered to predict the melt pool dimensions precisely Eq. (5.1) [49], [59], [89], [114].

$$k_x = \lambda_x k, \qquad k_y = \lambda_y k, \qquad k_z = \lambda_z k \tag{5.1}$$

$$\begin{Bmatrix} \lambda_x = \lambda_y = \lambda_z = 1, & T < T_{melting} \\ \lambda_x = 1, \quad \lambda_y = 4 \quad \lambda_z = 20 & T \geq T_{melting} \end{Bmatrix}$$

It should be noted that the enhancement factors can be identified based on the experimental results.

Based on Newton's law, a convective heat transfer to the surrounding area was considered on the top domain surface. The equation of convective heat transfer (Eq. (4.6)) is described in Section 4.3.2 of Chapter 4.

Besides, a radiative heat transfer of the upper domain surface to the ambient was taken into the account based on Eq. (4.7) which is presented in Section 4.3.2 of Chapter 4.

5.7 Volumetric heat source model

To predict the melt pool dimensions and temperature distribution during the process a three-dimensional (3D) conical-Gaussian heat source model was used (Fig. 4.4).

The conical-Gaussian heat source is formulated based on Eq. (4.13) [88] which is described in Section 4.3.3.1 of Chapter 4.

5.8 Results and discussion

In this section, the experimental and simulation results are presented. The effect of part geometry (thin-wall thickness) on the transient temperature profile and melt pool dimensions are investigated numerically and experimentally. Experimental melt pool results are also predicted using a 3D thermal simulation.

5.8.1 Thin-walls experimental melt pool measurements

Fig. 5.4 illustrates the melt pool shapes based on different sample thicknesses. The thickness of thin-walls significantly influenced the shape and dimensions of the melt pool. Results show that decreasing the thickness causes the melt pool dimensions to increase due to the occurrence of heat accumulation during the LPBF process. The thinner the wall thickness, the shorter the time to allow for the heat dissipation, cooling, and solidification of the melt pool during the laser scanning. Therefore, compared to thicker samples, the laser track melts the powder with a shorter distance for thin samples, which does not allow enough time for full melt pool solidification before the next laser scan track. In addition, thin samples provide less surface area resulting in less heat dissipation and

higher heat accumulation, creating larger melt pools. The melt pool dimensions result shows that with increasing thicknesses from 0.5 mm to 0.75 and from 0.5 mm to 1 mm, melt pool width decreases 31% and 45%, respectively. The results did not show any trend of the thin-wall thickness's influence on melt pool depth. It is realized that the thickness of the thin-walls has a stronger influence on melt pool width in contrast with the melt pool depth dimensions. For instance, by changing the thickness from 0.5 mm to 0.75 mm the melt pool depth is changed by 8%.

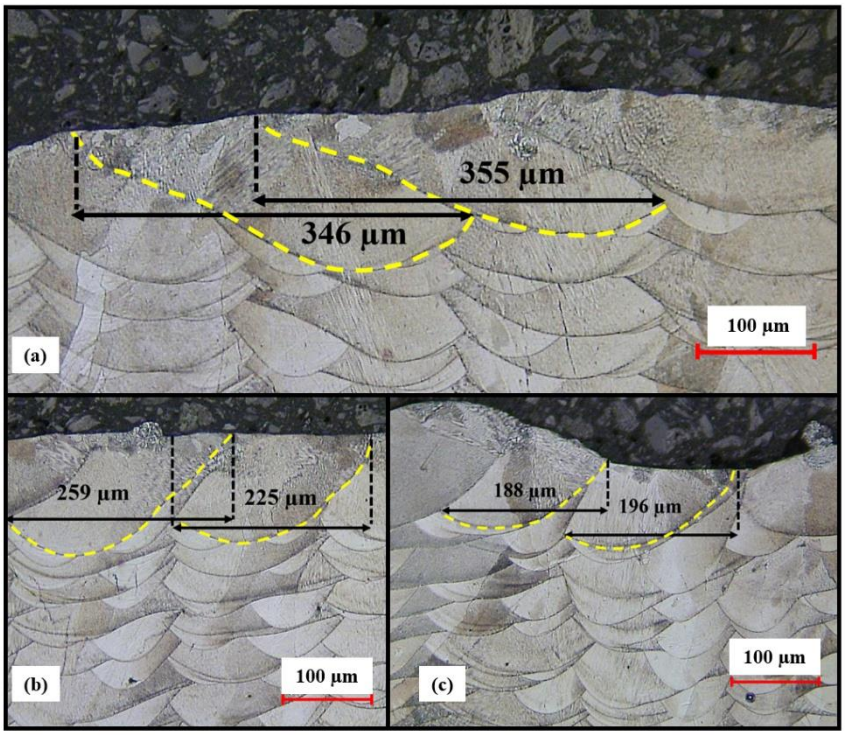

Fig. 5.4. Melt pool shape and dimensions of thin-walls, a) 0.5 mm thickness, b) 0.75 mm thickness, c) 1 mm thickness.

5.8.2 Numerical results

5.8.2.1 Single-track simulation

A three-dimensional FE model was developed to study the influence of thin-wall thicknesses on the melt pool formation during the building process. It is important to test the numerical model on single-track experimental results to validate the model before predicting thin-wall melt pool dimensions. Calibration of the heat source model is carried out based on single-track experiments at laser powers of 150 W, 200 W, and 250 W and scanning speed of 1000 mm/s. Fig. 5.5 shows the schematic of the single track simulation, and Fig. 5.6 demonstrates the corresponding experimental and numerical

results. The melting temperature is shown by the dashed line boundary in the melt pool region derived from simulation results.

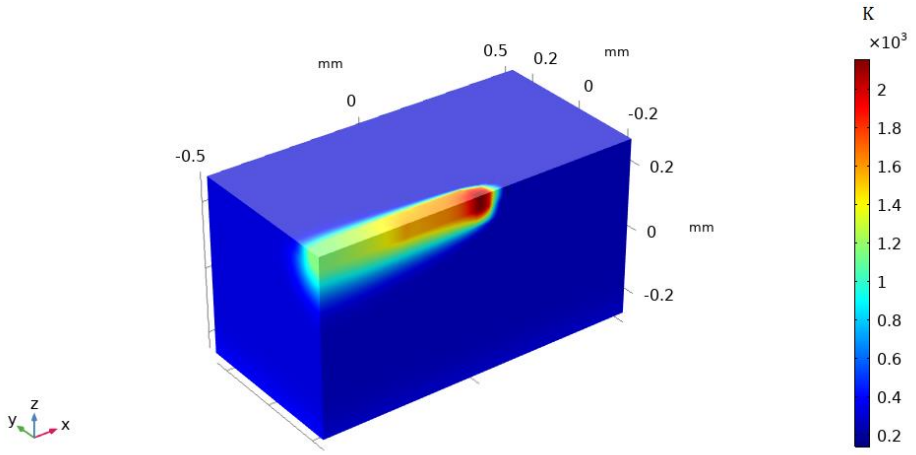

Fig. 5.5. Schematic of moving laser heat source on a single layer of powder (Single track simulation).

The results show that the heat source model was calibrated accurately and, therefore, can predict the effect of part thickness on the melt pool dimensions. It is important to predict the melt pool dimensions when key process parameters are changing. The calibrated model predicts the width and depth of the melt pool precisely. The average percentage difference between calibrated model and experimental results for predicting melt pool width and depth is 14% and 8%, respectively.

On the other hand, experimental results show that melt pool depth and width declined 66% and 27% by reducing the laser power from 250 W to 150 W. Thus, it is observed that laser power has a

more dominant effect on melt pool depth compared to melt pool width dimensions [106].

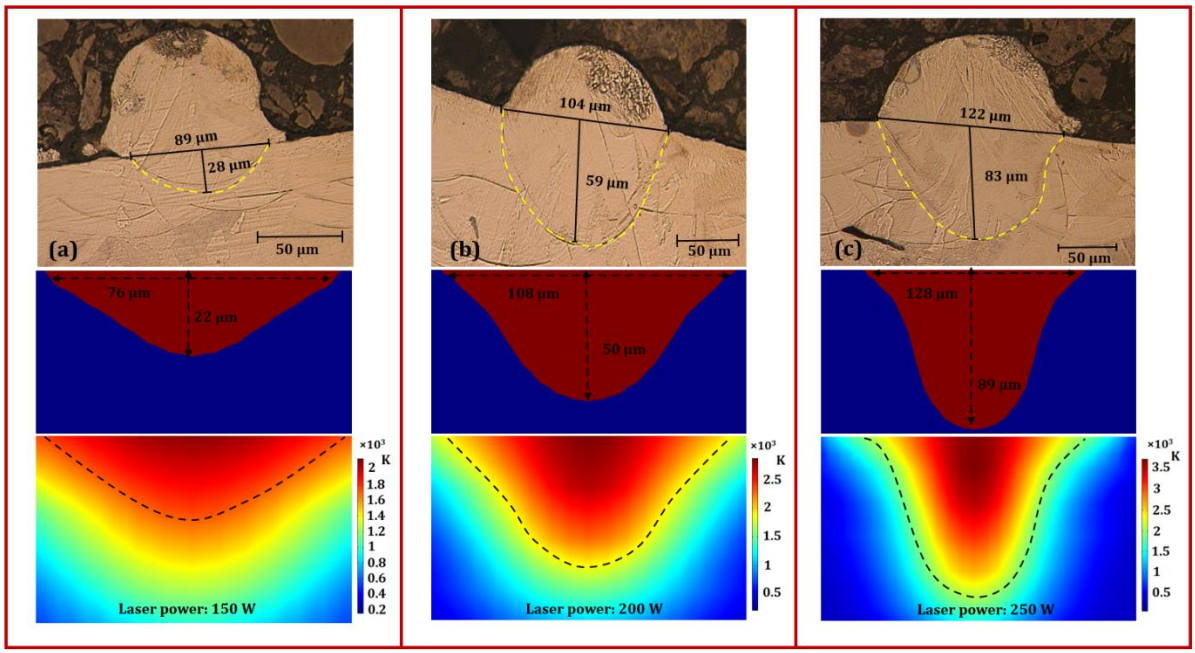

Fig. 5.6. Single-track melt pool dimensions derived from experimental and numerical results for three different conditions, a) Laser power 150 W and scanning speed 1000 mm/s, b) Laser power 200 W and scanning speed 1000 mm/s, c) Laser power 250 W and scanning speed 1000 mm/s.

5.8.2.2 Effect of process parameters on melt pool dimensions

The effect of process parameters (laser power and scanning speed) on melt pool dimensions was investigated as well to ensure the validity of the developed model. It is observed that increasing the laser power results in delivering higher heat intensity to the material for melting. Consequently, bigger melt pool dimensions (melt pool depth and width) are observed. On the other hand, an increase in the laser scanning speed results in smaller melt pools. Fig. 5.7 illustrates the predicted model versus experimental data and the effect of process parameters on melt pool dimensions. The results clearly show that the developed model can predict melt pool dimensions with high precision. The average percentage prediction difference between simulation and experimental ones for melt pool

depth and width is 16% and 5%, respectively.

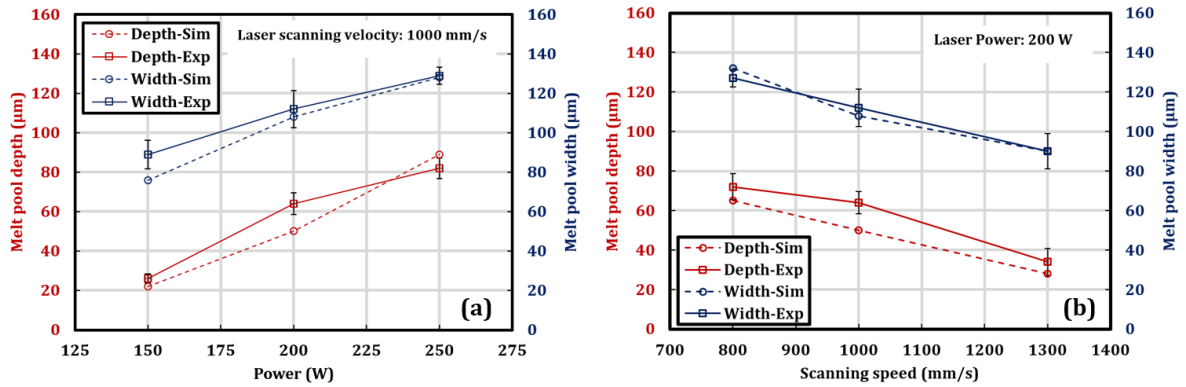

Fig. 5.7. The influence of process parameters on melt pool dimensions, a) The effect of laser power on melt pool depth and width, b) The effect of scanning speed on melt pool depth and width.

5.8.2.3 Multi-track simulation

The calibrated heat source model (Section 5.8.2.1) was used for multi-track simulations to study the effect of wall thickness on melt pool dimensions. The multi-track simulations were conducted using the same scanning strategy with the same geometries as those of the experimentally printed thin-walls (Fig. 5.1). Fig. 5.8 shows the schematic of the three multi-track simulations with different wall thicknesses. The multi-track simulation for 1 layer was carried out by adding 40 µm of Hastelloy X powder on top of the base material followed by laser scanning. Results from Fig. 5.8 show the temperature distribution in the whole part during the laser scanning. A detailed analysis is given below.

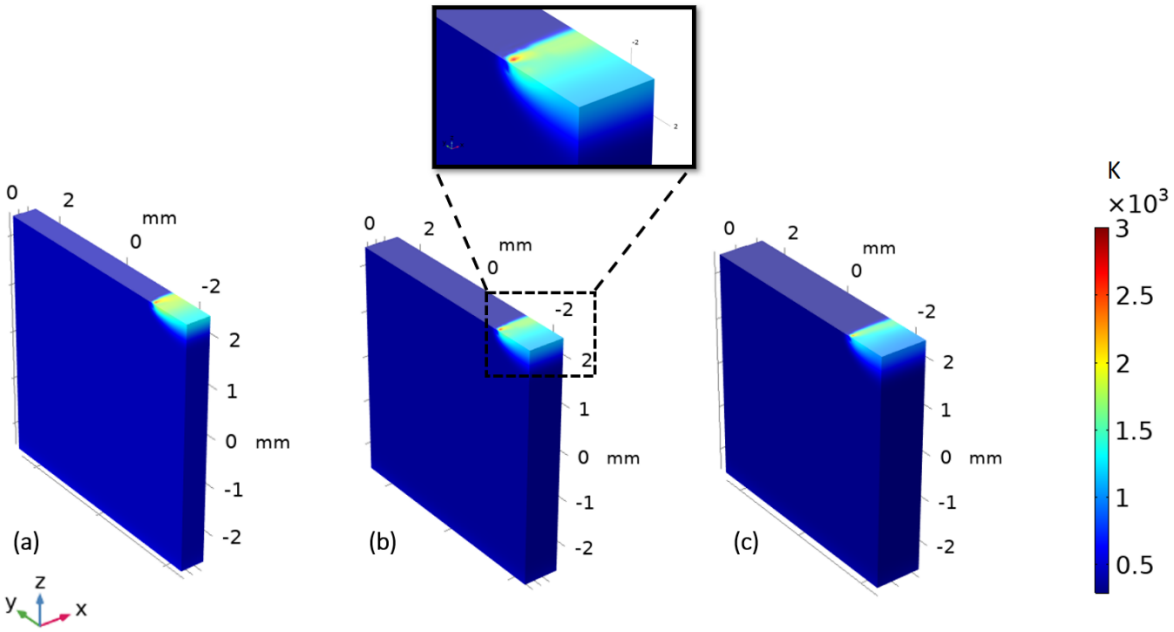

Fig. 5.8. Multi-track simulation of three different conditions of geometry sizes while keeping process parameters constant, laser power 200 W, scanning speed 1000 mm/s and hatch distance 90 µm, a) Thickness 0.5 mm, b) Thickness 0.75 mm, c) Thickness 1 mm.

In order to investigate the influence of the wall thickness on melt pool dimensions, the cross-section plane was created perpendicular to the direction of laser movement. The melt pool geometries from the cut-planes were plotted in the center and near the edge of the printed parts to analyze the effect of geometry and wall thickness on melt pool dimensions. The corresponding melt pool regions are shown in Fig. 5.9 (a) (near the middle of the thin-wall) and Fig. 5.9 (b) (near the edge of the thin-wall).

Derived melt pools from the edge of the thin-walls show that as multiple tracks of laser scan pass adjacent to each other, the melt pool shapes tend to be elongated due to the heat accumulation. This phenomenon happens because the melt pool does not have enough time to solidify as the laser spot melts the adjacent tracks. It can be clearly seen that the melt pool is drastically elongated for the thin-wall thickness of 0.5 mm. Results show that by decreasing the thickness of the thin-walls from 1 mm to 0.5 mm, the stabilized melt pool width enlarges approximately 1.5 and 2 times in the edge and middle cross-section plane, respectively.

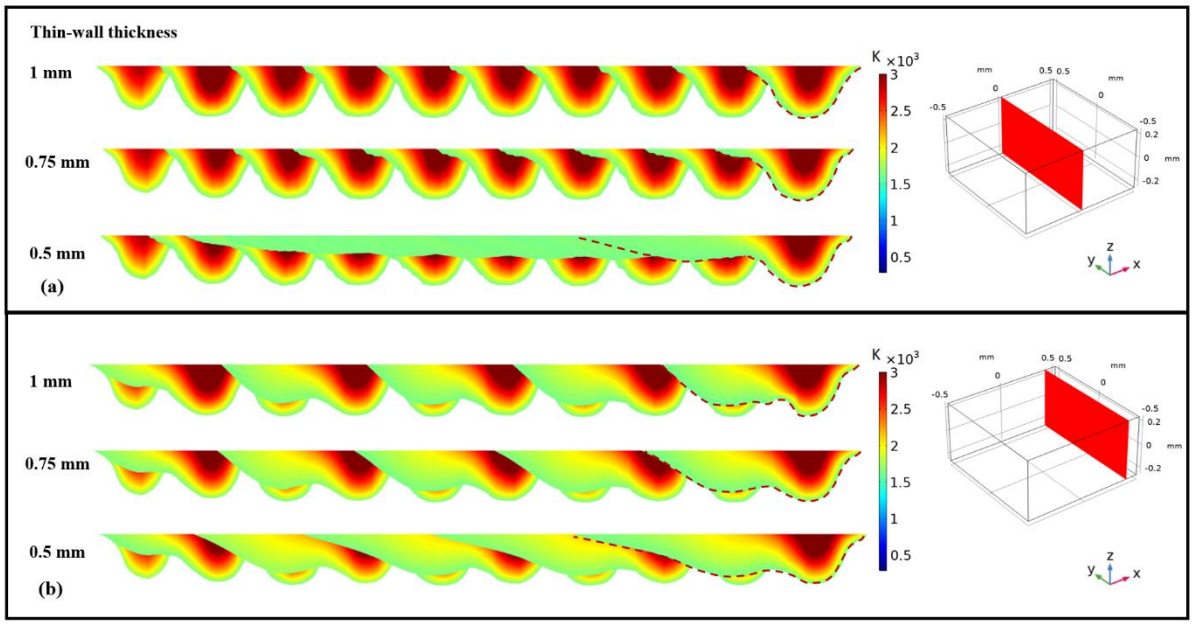

Fig. 5.9. Melt pool geometries of multi-track simulation, a) Melt pools derived from the middle cut plane and, b) the edge of the printed parts for process parameters, laser power 200 W, scanning speed 1000 mm/s and hatch distance 90 µm.

The melt pool geometries derived from two different cut plane sections show that the temperature distribution close to the edge of the geometry domain is higher due to the heat accumulation phenomenon. As a result, the melt pool dimensions extracted from the edge of thin-walls are larger than melt pool dimensions derived from mid-plane cross-sections. For instance, the stabilized melt pool width of thin-wall thicknesses of 0.75 mm and 1 mm for the edge cross-section plane are 1.2 and 1.3 times bigger than the melt pool width derived in the middle domain area, respectively. It can be seen from the results (Fig. 5.9) that the melt pool dimensions seem to stabilize after a few tracks. Therefore, the first track shows the smallest melt pool and does not reflect the real melt pool dimensions. As the process continues, melt pool dimensions enlarge, and after passing several laser tracks, the melt pools stabilize. Besides, thinner walls take a longer time to reach stabilized melt pools due to larger heat accumulation. The melt pool evolution results (Fig. 5.10 (a)) show that the melt pool width for the 0.5 mm, 0.75 mm, and 1 mm wall thickness stabilizes after 10, 8, and 5 laser tracks in the middle section region, respectively. Comparison between the melt pools from the middle and edge of the part shows that melt pool stability is achieved after a larger number of tracks for the edge

of the parts (Fig. 5.10 (b)). The simulation results show that on average, edge melt pools stabilize after 10 tracks.

Fig. 5.10 (a) and (b) show the quantitative melt pool dimensions for middle and edge planes, respectively. It should be noted that, based on the observation from experimental results, the melt pool depth does not change significantly. It is realized from the simulation results that a reduction in the thickness from 1 mm to 0.75 mm leads to a 20% increase in stabilized melt pool width while decreasing the thin-wall thicknesses from 0.75 mm to 0.5 mm enlarges the melt pool width to 40% in the middle section region. On the other hand, a decrease in the thickness from 1 mm to 0.75 mm results in a 10% increase in stabilized melt pool width while a reduction in thickness from 0.75 mm to 0.5 mm leads to an increase of melt pool width by 25% in the edge plane. In addition, the melt pool width dimensions derived from the edge-cross section plane are approximately 20% and 25% larger for thin-wall thicknesses of 0.75 mm and 1 mm, respectively compared with extracted middle-plane melt pool dimensions.

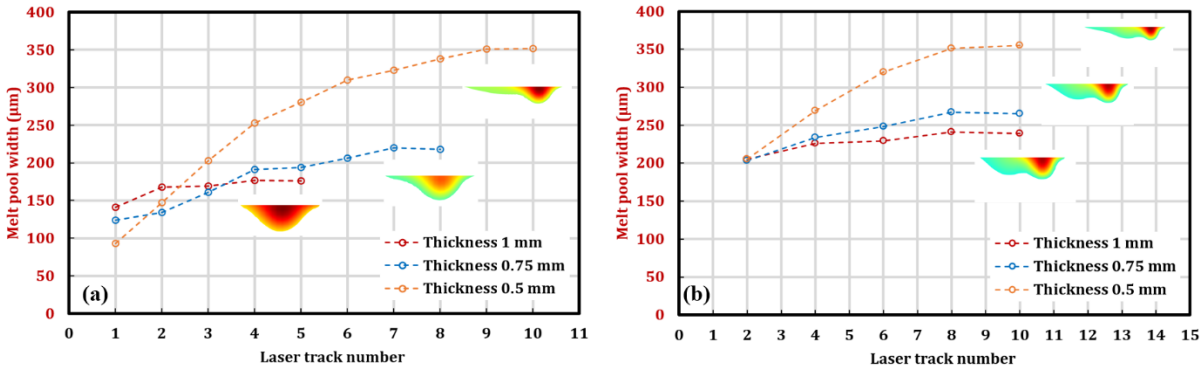

Fig. 5.10. Melt pool evolution during multi-track LPBF process, a) Melt pool derived from the middle plane cross-section, b) Melt pool derived from the edge plane cross-section.

5.8.2.4 Validation of simulation results

The simulation results discussed in Section (5.8.2.3) were also validated with experimental results to highlight the strength of the proposed model (Fig. 5.11). The validation results in Fig. 5.11 show the melt pool evolution at the edge cross-section of the thin-walls with different thicknesses. Simulation results show acceptable agreement with experimental ones. It should be noted that all simulation results fall within the error bars from the experimental results. Fig. 5.11 (a) demonstrates

the experimental and simulated melt pool width dimensions in the middle of thin-wall thickness, while the track results from the edge of the thin-walls are shown in Fig. 5.11 (b). The percentage difference between simulation and mean experimental results for the middle tracks of thin-wall thicknesses of 0.5 mm, 0.75 mm, and 1 mm were found to be 7%, 7%, and 11%, respectively. On the other hand, the percentage difference for the edge tracks of thin-wall thicknesses 0.5 mm, 0.75 mm, and 1 mm were 9%, 7%, and 5%, respectively. It is observed that by increasing the thickness of the thin-walls from 0.5 mm to 1 mm, the melt pool width of middle and edge tracks declined by 30% and 35%, respectively. Besides, the validation results shown in Fig. 5.11 demonstrate that melt pool width dimensions of the edge tracks of thin-wall thickness 0.5 mm, 0.75 mm, and 1 mm are 17%, 4% and, 11% bigger than middle tracks. The melt pool near the edges of the thin-walls has less time to solidify until the next adjacent laser track. As a result, the melt pool width near the edges of the thin-walls is elongated compared to middle tracks.

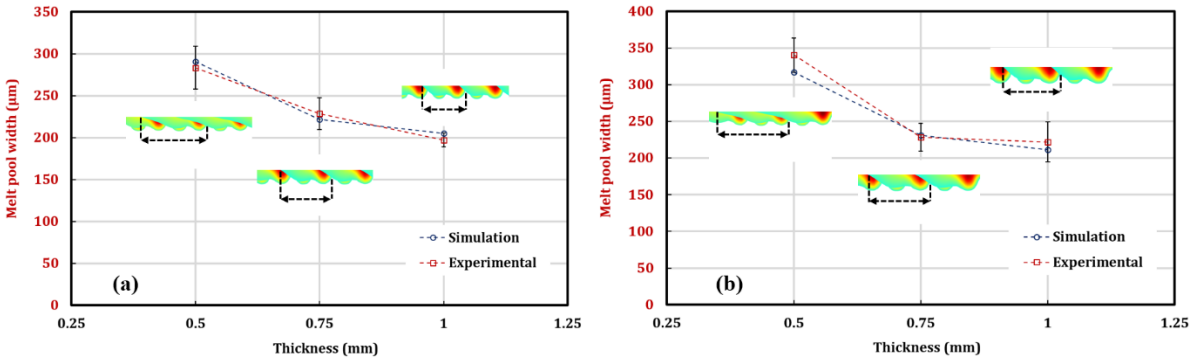

Fig. 5.11. Validation of multi-track simulation results derived from the edge cross-section plane, a) middle tracks and b) edge tracks melt pool width dimensions.

5.8.2.5 Transient temperature profile and temperature gradient results

As mentioned in Section (5.8.2.3), the reason behind elongated melt pool geometries stems from heat accumulation induced during the LPBF process and an increase in the transient temperature profile of thinner parts. For further investigation on the temperature distribution during the process, a probe on the top surface of the three geometries was used for capturing the transient temperature profile. The schematic of the probe's location in the middle of the sample surface is shown in Fig. 5.12. In order to investigate the influence of the locations on the transient temperature profile, another

probe close to the edge of the domain geometry was also located to observe the differences between the transient temperature profile between the middle and edge of the thin-walls.

Fig. 5.12 (a) and (b) show the transient temperature profile of three thin-walls with different thicknesses derived from the probe in the middle and the edge of the domain geometry using the same process parameters (laser power 200 W and scanning speed 1000 mm/s), respectively. Transient temperature profile results illustrate that by decreasing the thickness of the parts, peak temperature gradually increases due to the heat accumulation phenomenon. The maximum temperatures derived from the probe in the center of thin-wall geometries with 1 mm, 0.75 mm, and 0.5 mm thicknesses were found to be 3157 K, 3206 K, and 3265 K, respectively. Similarly, the transient temperatures extracted from the probe near the edge of the thin-wall demonstrate that the peak temperature elevates due to heat accumulation. The maximum temperature derived from the probe in the edge of the thin-wall thicknesses of 1 mm, 0.75 mm, and 0.5 mm are 3221 K, 3268 K, and 3332 K, respectively. The simulation results indicate that by decreasing the thickness of the thin-walls from 1 mm to 0.5 mm the maximum temperature in the center and the edge of the thin-walls increase by 3%. Besides, the maximum temperature near the edge was 2% higher than the center. The reason behind this is that heat dissipation in the middle section area is higher than the edge of the domain part and the laser track near the edge has less time to be cooled down. These results are consistent with the larger melt pool dimensions observed in the edge of the domain geometry in Section (5.8.2.3).

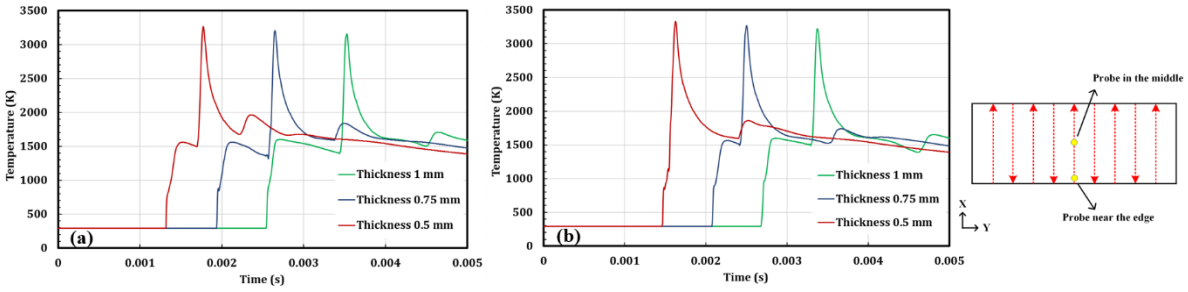

Fig. 5.12. The transient temperature profile of three thin-wall thicknesses, a) probe in the middle, and b) near the edge of the domain geometry.

To further investigate the effect of the transient temperature profile on the final microstructure of the printed parts, the average temperature gradient was extracted from the simulated geometries. As is shown in Fig. 5.13, the derived temperature gradient related to the thinnest fabricated parts was much higher than other thin-walls. The maximum temperature gradient during the process of the thin-walls with different thicknesses of 1 mm, 0.75 mm, and 0.5 mm was found to be 2.7×10^6 (K/m), 3.1×10^6

(K/m), and 3.9×10^6 (K/m), respectively. Thus, the results indicate that by increasing the thickness of the parts from 0.5 mm to 1 mm the temperature gradient decreased by approximately 30 %.

There are numerous studies on the effect of temperature gradient on the microstructure which indicates that temperature gradient has a direct relationship with the cooling rate [11], [14], [115], [116]. The following equation Eq. (5.2) indicates the direct relationship between temperature gradient and cooling rates [49]:

$$\dot{T} = G \times R \tag{5.2}$$

where $\dot{T}$, G and R are cooling rates, temperature gradient, and solidification rate, respectively. Since the temperature gradient is directly proportional to the cooling rate, a significant change in the average G value of a deposited layer can influence the average cooling rate of the entire successive layer. It should be noted that the solidification rate may not be changed significantly for various thin-wall thicknesses as it is mainly depending on laser scanning speed during LPBF [98].

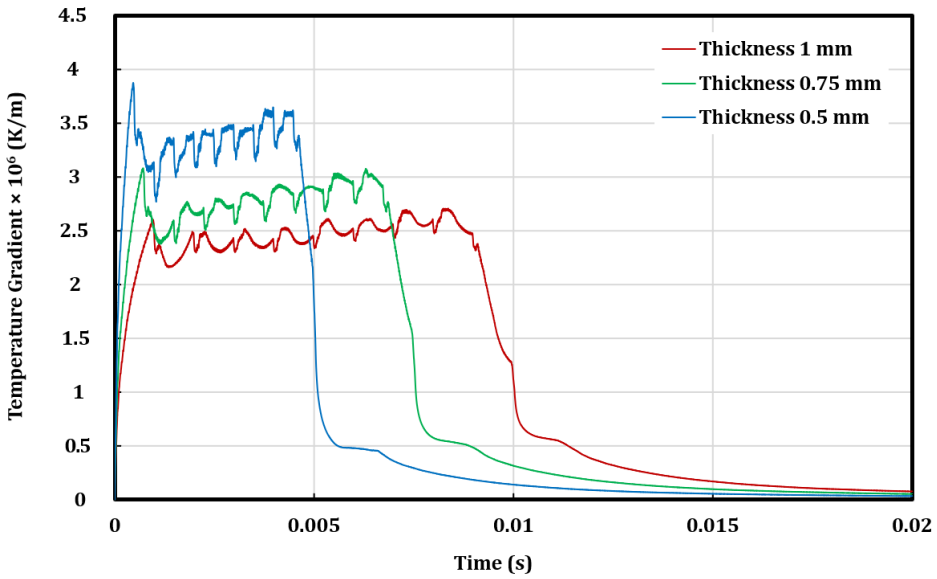

Fig. 5.13. The extracted average temperature gradient during the process for different thin-wall thicknesses.

An Electron Backscatter Diffraction (EBSD) analysis has been performed to investigate the influence of the thin-wall thickness of the microstructure. Specifically, inverse pole-figure (IPF) maps were analyzed to investigate the effect of a transient temperature profile and temperature gradient on the average grain size of printed thin-walls with different thicknesses. Fig. 5.14 depicts the IPF maps of

samples with different thicknesses of 0.5 mm, 0.75 mm, and 1 mm. The results show that the thin-wall with 0.5 mm thickness has a smaller grain size compared to the 1 mm thicknesses. The average grain size of 216 µm, 198 µm, and 167 µm (Fig. 5.15) are observed for the thin-wall thickness of 1 mm, 0.75 mm, and 0.5 mm, respectively. The larger grain size can be attributed to the lower temperature gradient and cooling rate induced during the process due to the sample's larger thickness. Thus, a lower supercooling temperature can result to have lower nucleation rate and coarser grain structure when the thicker wall is compared to the thinner wall. As a result, the simulation results are consistent with experimental ones. As it can be seen from the transient temperature profile the peak temperature is elevated for thinner parts. Consequently, the temperature gradient is increased by decreasing the thicknesses of the parts. Therefore, increasing the temperature gradient leads to a reduction in the grain size of the manufactured parts [116].

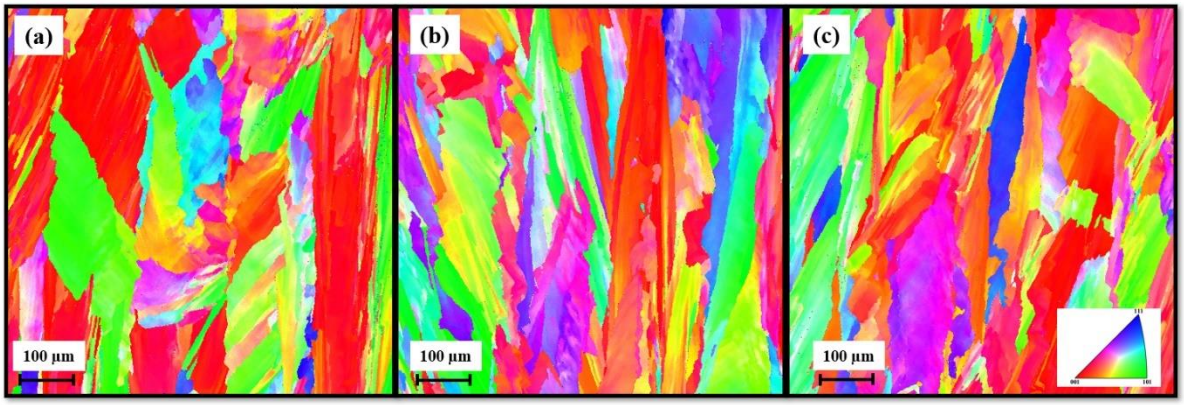

Fig. 5.14. EBSD pictures of printed thin-walls with different thicknesses of a) 1 mm, b) 0.75 mm, and c) 0.5 mm.

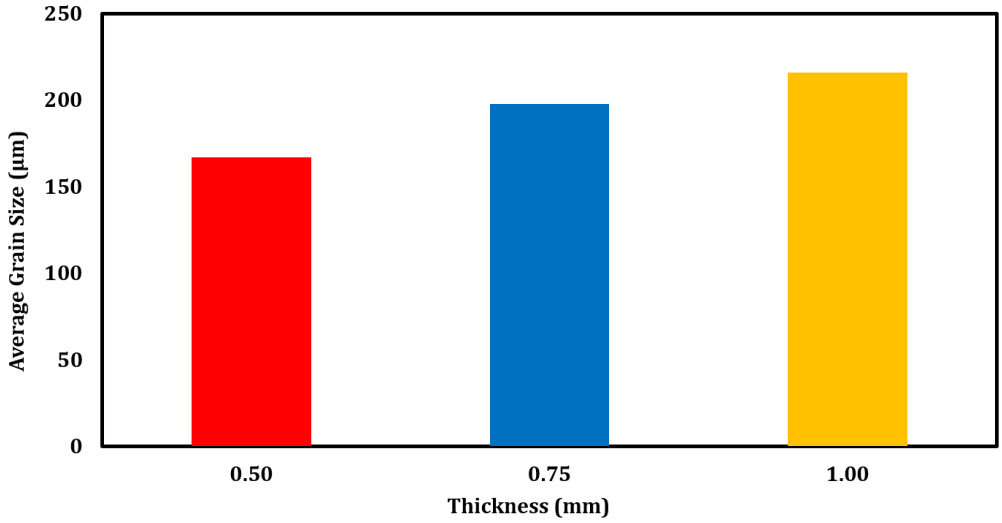

Fig. 5.15. The average grain size relating to different printed thin-wall thicknesses.

5.8.2.6 Process mapping result

The validation of the single track and multi-track results highlights the strength of the LPBF model used in this work. Therefore, the model was used to further investigate the effect of thin-walls thickness and process parameters on melt pool dimensions. Melt pool dimensions were derived for various process parameters (Laser power:150 W, 200 W, and 250 W, Scanning speed:1000 mm/s) which result in acquiring different energy densities $p/\sqrt{v}$ where p (W) is the laser power and v (mm/s) is the scanning speed [106]. Multi-track simulations were run with varying process parameters and different thin-wall thicknesses. Fig. 5.16 demonstrates the influence of different energy densities and thin-wall thicknesses on the melt pool dimensions. Three different regions based on the geometry of melt pools can be identified. The red color zone shows non-overlapping melt pools for low energy density values which would result in a low part density for thicknesses greater than 0.5 mm. However, for thinner walls, the low energy density seems to produce overlapping melt pools which would reduce the porosity. On the other hand, the yellow color zone demonstrates the elongated melt pool shapes due to heat accumulation for thin-wall thicknesses less than 0.5 mm. Generally, elongated melt pools are observed for higher energy density with thinner thin-wall thickness. This larger melt pool width can be detrimental due to inducing higher residual stress of the printed parts [103]. The proper melt pool shapes are represented by the green color region between the energy density range of 6.32 to 7.91 with the thin-wall thicknesses larger than 0.5 mm. Results show that the range of

energy density for the various thin-wall thicknesses carries an important relationship between thin-wall thickness and the proper process parameter selection to print high-quality parts.

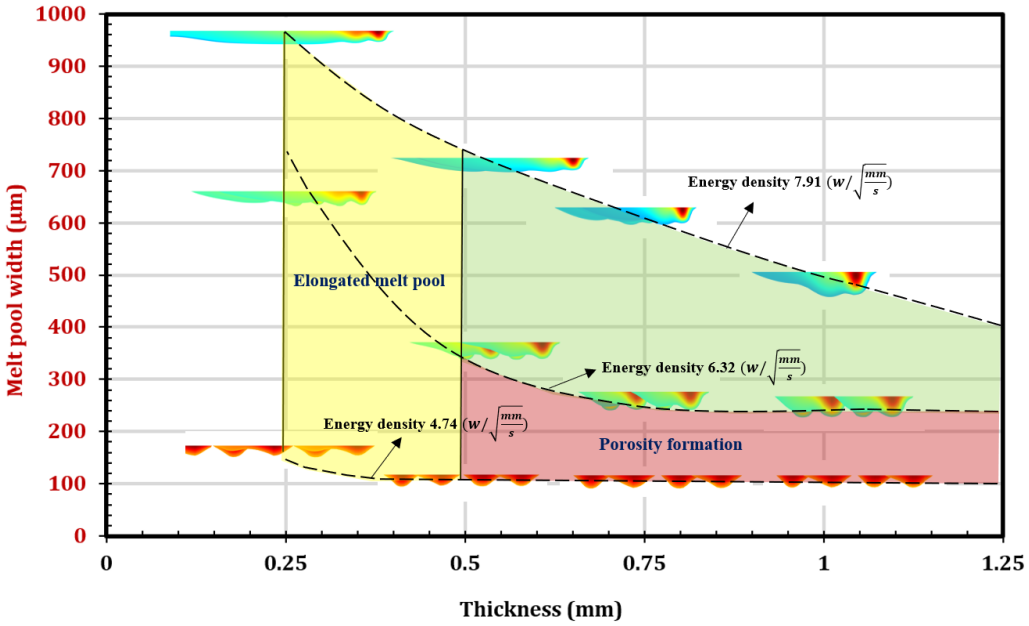

Fig. 5.16. The process mapping results of melt pool width.

5.9 Summary

In this study, the effect of thin-wall thickness is investigated on the melt pool geometries and transient temperature during the LPBF process. A three-dimensional (3D) Finite Element (FE) thermal model is developed for simulating the multi-track LPBF process. Both experimental and simulation results are used to investigate the effect of thin-wall thicknesses on melt pool geometries and transient temperature profiles. The following conclusions are drawn based on this study:

1- Experimental results show that for the same process parameters, a reduction in the thickness increases the melt pool dimensions (melt pool width) significantly. The melt pool dimensions result shows that with increasing thicknesses 0.5 mm to 0.75 and 0.5 mm to 1 mm, melt pool width decreases 31% and 45%, respectively. Besides, the results show that the influence of thin-wall thickness on the melt pool width is more dominant than on the melt pool depth.

2- Single-track simulations were validated with experimental results at a various laser power range of 150 W to 250 W and scanning speed range of 800 mm/s to 1300 mm/s with an average error of

16% and 5% for melt pool depth and width, respectively. Successful validation of the single-track model enables the model to be further implemented towards multi-track simulation.

3- Thin-wall simulation results show a melt pool evolution during the LPBF process resulting in stabilized melt pools after a few laser tracks have been scanned. It is realized that this is due to the high heat accumulation observed in thin-wall samples. Besides, the melt pool geometries near the edge of the part show higher dimensions of melt pool geometries compared to the middle cross-section.

4- Comparison of the experimental and simulated melt pools of thin-wall geometries showed strong reliability. The percentage difference between simulation and mean experimental results for the middle tracks of thin-wall thicknesses of 0.5 mm, 0.75 mm, and 1 mm were found to be 7%, 7%, and 11%, respectively. On the other hand, the percentage difference for the edge tracks of thin-wall thicknesses 0.5 mm, 0.75 mm, and 1 mm were 9%, 7%, and 5%, respectively. These results show the strength of the model proposed in this work.

5- The gradual increase in the peak transient temperature profile shows the heat accumulation phenomenon exists during the LPBF process. As a result, by decreasing the thicknesses of the thin-walls from 1 mm to 0.5 mm the peak transient temperature rises 3% approximately. Besides, the maximum temperature in the edge location is 2% higher than the center of thin-walls which is consistent with the larger melt pool dimensions in the edge of the domain geometry. On the other hand, the simulation results show a higher temperature gradient during the process of thinner parts which results in a smaller grain size of the final microstructure.

6- A process parameter map based on the effective parameter $\frac{p}{\sqrt{v}}$ shows that the conduction melt pool zone relies on the energy densities between 6.32 $W/\sqrt{mm/s}$ to 7.91 $W/\sqrt{mm/s}$ for the thin-wall thicknesses larger than 0.5 mm. Elongated melt pools are observed in higher energy density for thin-wall thickness between 0.25 mm and 0.5 mm. Besides, non-overlapping melt pools are created in the red region with a lower energy density and thickness larger than 0.5 mm. As a result, printed parts in this region may have higher porosity and lower mechanical properties. The results highlight the importance of part thickness-based parameter selection.

Chapter 6. Macroscale Modeling of Laser Powder-Bed Fusion Process

6.1 Introduction

This chapter presents macroscale modeling. The simple equivalent heat source model is introduced and the band-band simulation approach is described for accelerating computational time. Finally, residual stress and distortion are predicted for a limited number of layers.

Researchers have been investigating on implementing various approaches to accelerate the thermo-mechanical LPBF modeling. Irwin and Michaleris [117] developed a line heat source model to accelerate the simulation time. The time increment in their simulation was increased which leads to reduce the computational cost significantly. Soldner and Mergheim [21] proposed a new approach of using multiple time-steps in their modeling for speeding up their simulation. In addition, implementation of using adaptive mesh and line heat source model is carried out. Their developed model is utilized for thermal analysis of the LPBF simulation. However, in their study, the thermo-mechanical analysis was not investigated. Zeng et al. [118] studied the adaptive-mesh approach in LPBF modeling, which uses the finer mesh size in melt pools and heat-affected zones, while the remaining domain area has coarser mesh sizes. Therefore, the computational cost was reduced, and by comparing it with a uniform fine mesh model acceptable accuracy was achieved. Keller et al. [119] conducted a part-level LPBF simulation by implementing the heat flux on a slice of a part at once, which could reduce the computational cost. Seidel et al. [120], [121], introduced four heat-input models for investigating temperature distribution in the LPBF process. Papadakis et al. [122], [123] compared computational time for different accelerated approaches of thermo-mechanical LPBF models including laser-heat input volume-by-volume, layer-by-layer, and vector-by-vector. Chiumenti et al. [80] used the element birth-and-death method for simulating the temperature distributions in LPBF. Three different sizes of the domain including hatch-by-hatch, layer-by-layer, and reduced hatch-by-hatch are implemented for this approach. The temperature distribution was extracted by using thermo-couples embedded in the printed part. The simulation thermal analysis results were compared with experimental ones. However, the residual stress distribution results were not investigated. Neiva et al. [124] developed a parallel finite element framework (FEMPAR-AM), for modeling additive manufacturing at the part scale. In addition, the adaptive mesh was incorporated into the framework.

In this chapter, a thermo-mechanical model in macroscale simulation is carried out for predicting residual stress and deformation. For accelerating simulation in the macroscale model, several bands are created which are applied by a simple equivalent heat source. Laser exposure time for each band is calculated based on a single-track simulation.

6.2 Model geometry and a simple equivalent heat source model

In macroscale simulation, the dimension of geometry becomes larger (5×5×0.5 mm), and several bands with a width of 100 μm are created (Fig. 6.1). The cuboid mesh with the 3364 number of elements is implemented in this model.

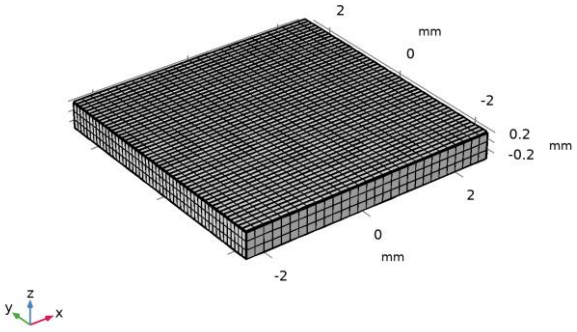

Fig. 6.1. Model geometry in macroscale simulation.

In addition, parameters for calculating an equivalent heat flux are based on the calibrated volumetric heat source (Fig. 6.2). Eq. (6.1) shows an equivalent heat flux that is applied to each band and Eq. (6.2) demonstrates the calibrated parameters used for the calculation of the volume of the cone shape.

$$\text{Equivalent heat flux} = \frac{\text{Laser power}}{\text{Volume of cone}} \tag{6.1}$$

$$\text{Volume of the cone} = \frac{\pi H}{3}(r_0^2 + r_0 r_d + r_d^2) \tag{6.2}$$

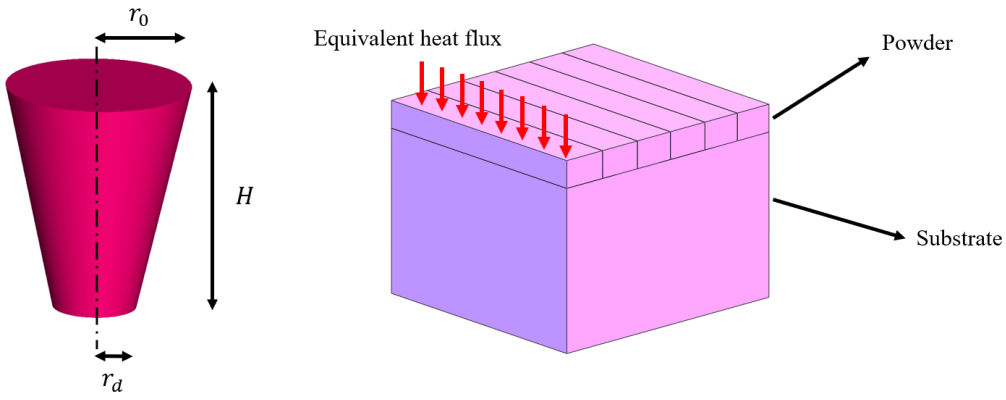

Fig. 6.2. Equivalent heat flux.

Laser exposure time can be derived from the heating cycle of single-track simulation. Therefore, the same heating cycle is applied for each band for replicating the thermal cycle (Fig. 6.3).

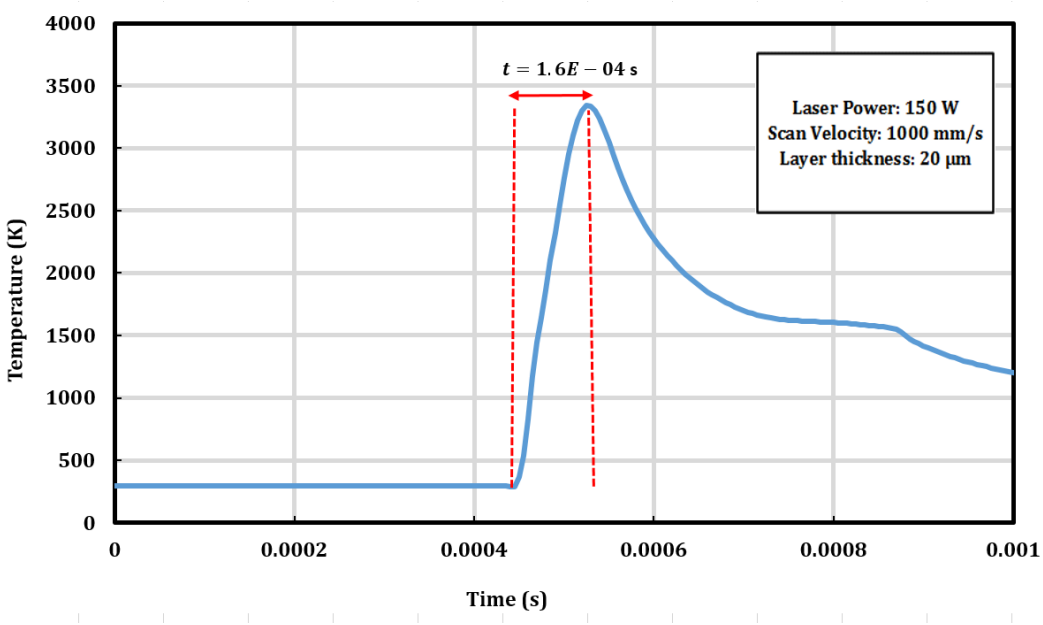

Fig. 6.3. Thermal cycle derived from single track simulation.

6.3 Governing equation and boundary conditions

Thermo-mechanical modeling in macroscale consists of two steps. In the first step, thermal analysis is done for the whole process in order to capture the temperature gradient. In the second step, the results derived from the previous step act as an input of thermal load for the second step. Eventually,

mechanical analysis is carried out and the residual stress and deformation can be estimated for the whole process. The governing equation for mechanical analysis is illustrated as follows [54]:

$$\nabla . \sigma = 0 \tag{6.3}$$

$$\sigma = C\varepsilon_e \tag{6.4}$$

$$\varepsilon_{th} = \alpha . \Delta T \tag{6.5}$$

$$\varepsilon = \varepsilon_e + \varepsilon_p + \varepsilon_{th} \tag{6.6}$$

where σ is the stress which can be calculated from Eq. (6.4). C is stiffness tensor and ε is total strain including elastic strain (ε_e), plastic strain (ε_p), and thermal strain (ε_{th}). Thermal strain also can be calculated from Eq. (6.5), where α, and ΔT are thermal expansion coefficients and temperature change in a specific time.

6.4 Multi-track single layer simulation

The predicted results of residual stress and deformation from the thermo-mechanical model are derived from the first layer (Fig. 6.4).

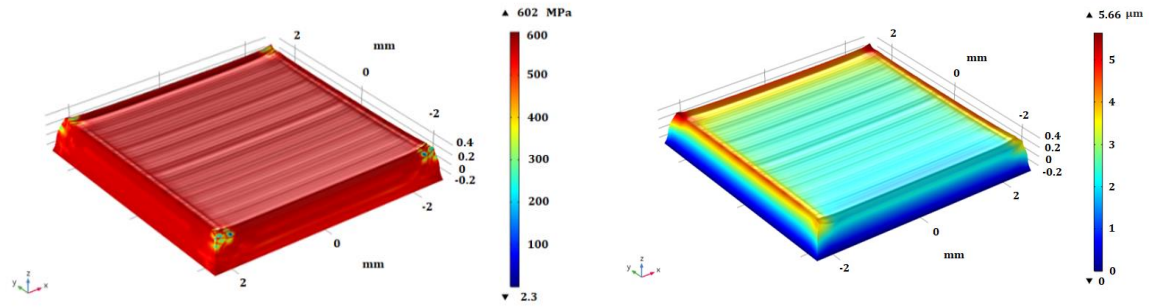

(a) (b)

Fig. 6.4. (a) Residual stress, (b) Displacement for the first layer.

In order to extract residual stress and displacement on the top surface, the specific path along the x-direction is identified as shown in Fig. 6.5.

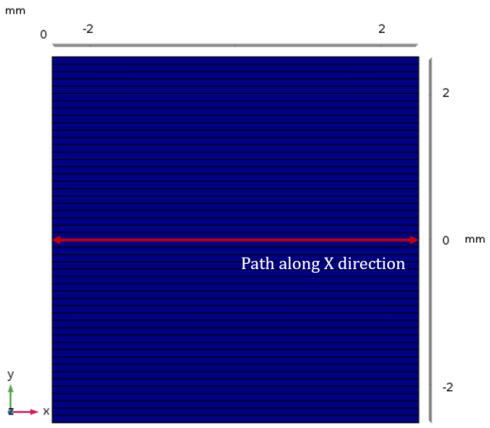

Fig. 6.5. Identifying path along the x-direction.

The results show that maximum residual stress (607.18 MPa) occurs in the middle of the domain, whereas maximum displacement (4.55 μm) happens at the edge of geometry (Fig. 6.6).

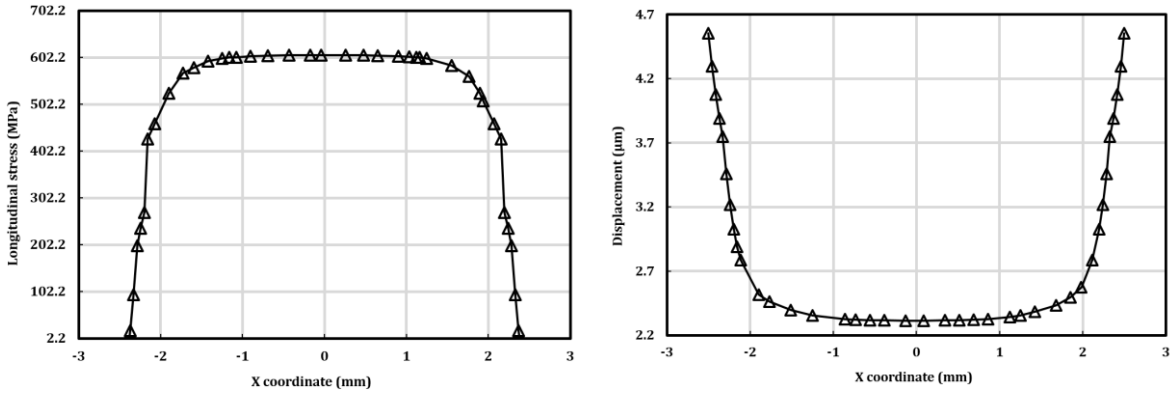

(a) (b)

Fig. 6.6. (a) Residual stress along x-direction on the top surface, (b) Displacement along x-direction on the top surface.

6.5 Multi-track multi-layer simulation

In addition, multi-track multi-layer simulation was conducted for a limited number of layers. The element activation and deactivation method were implemented for modeling the building-up process. Once a powder layer was scanned by equivalent heat flux the material property was solidified and the

new powder layer was activated on top. This modeling process was repeated for a limited number of layers. The evolution of deformation and residual stress was predicted during the process simulation. Fig. 6.7 demonstrates that the top layer has the highest residual stress and deformation. The reason behind this is that the temperature gradient on the top layer was increased due to dissipating heat into the ambient.

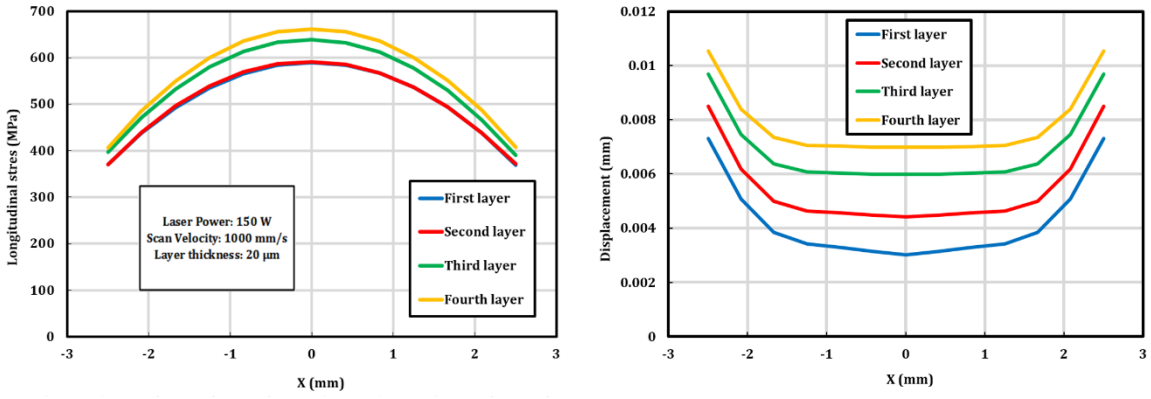

(a) (b)

Fig. 6.7. (a) Residual stress along x-direction for different layers, (b) Displacement along x-direction for different layers.

6.6 Summary

In macroscale simulation, a simple equivalent heat source model is proposed for accelerating simulation. Based on laser exposure time derived from a single track and calibrated heat source parameters, equivalent heat flux was calculated and applied to each band. Finally, residual stress and deformation are predicted for the first layer. The results show that residual stress has the highest value in the middle of the part due to heat accumulation. On the other hand, deformation on the edges of the part is larger compared to other regions, due to the small feature of edges. In addition, the thermo-mechanical analysis modeling of multi-track multi-layer was carried out. It is found that longitudinal residual stress and deformation on the top layer have the highest value relative to other layers. This could be explained by higher heat dissipation on the top layers to the ambient. Therefore, the temperature gradient and the cooling rate will be higher on the top layers. One of the challenging issues in macroscale modeling is predicting residual stress and deformation efficiently. Since modeling large-scale parts need a huge number of layer thickness, as a result, computational time will

be extremely expensive. Combining several layers and heating them together (lumped model) is one of the effective approaches for accelerating simulation. However, determining equivalent heat flux for larger layer thickness is another challenging issue that needs to be addressed. Therefore, in the future, equivalent heat flux for larger-scale layer thickness is going to be determined, and similar heating and cooling cycles from microscale modeling are going to be deployed in macroscale simulation. Ultimately, an approach for fast predicting residual stress of cube geometry is going to be proposed and the validation with experimental results will be conducted.

Chapter 7. Macroscale Modeling Application - Cube Building Process Simulation

7.1 Introduction

In this chapter, the thermo-mechanical model in macroscale is developed for simulating simple geometry (cube) samples time-efficiently. The aim is to accelerate the FE analysis of the LPBF process for predicting the residual stress and deformation of the fabricated parts. To achieve this goal, a fast thermo-mechanical model using an effective heat source is developed. Implementing a decoupled thermo-mechanical while using an effective heat source can reduce the computational cost significantly. Residual stress of the printed cubes is measured experimentally and compared with simulation results. The results of the developed model show a good agreement with experimental ones and can predict the residual stress of the parts precisely and time-efficiently.

Researchers have tried to develop various methodologies for fast predicting residual stress and deformation. There are multiple commercial software available for simulating the LPBF process. However, their methodologies are not close to the reality of evolving the process. Here are some available approaches for addressing the issues:

1- Implementing the inherent strain method is one of the most common methodologies which is widely used in the most available commercial software such as AutoDesk Netfabb, ANSYS, MSC Simufact, GE GeonX, Amphyon Works, Siemens NX [50], [63], [125]–[128]. Li et al. [129] developed a multiscale model including microscale, mesoscale, and macroscale simulation by implementing initial residual stress, to accelerate the prediction of part deformation in LPBF. Keller et al. [62] implemented the inherent strain technique to develop a fast simulation model for predicting deformation and residual stresses of AM parts. Siewert et al. [130] conducted a comprehensive validation for the inherent strain method, in which both the residual stresses and deformation are validated by experiments. However, this methodology lacks transient thermal analysis in its approach. It means that only mechanical analysis is carried out for predicting residual stress and deformation which is not the case of the LPBF process.

2- Implementing a lumped model is another approach for accelerating the simulation. In this methodology, an equivalent volume of heat flux is applied to each layer. However, laser scanning strategies cannot be considered in this approach. Another drawback of this methodology is that the

real cooling rate and temperature gradient cannot be modeled. On the other hand, some researchers use an effective heat flux which is a simple heat source without having a Gaussian profile. Therefore, by using this heat flux the precise cooling rate and temperature gradient cannot be captured in their model. In addition, they did not consider powder material properties in most of their model. Consequently, their model lacks phase transformation which is extremely critical for thermo-mechanical analysis [60], [66], [129], [131], [132].

7.2 Experimental methodology

Several cubes of Hastelloy X material are printed using EOS M290 (EOS GmbH, Krailling, Germany) 3D printer machine. Different process parameters are chosen for further investigation of their influence on the final residual stresses. Table 7.1 indicates the selected process parameters for printing cubes samples. Each set of process parameters had three repetitions. Therefore, 9 samples with different laser process parameters are selected for the validation of the simulation results.

Table 7.1. Process parameters used for printing cube samples.

Process parameters	Values
Laser power (W)	150-200-250
Scanning Speed (mm/s)	1000
Laser spot diameter (µm)	100
Layer thickness (µm)	40

X-Ray residual stress analyzer machine µ-X360s (Pulstec Industrial Co., Ltd, Hamamatsu, Japan) is used for measuring the residual stresses of the samples. The µ-X360s residual stress measurement device is based on cos α. This method utilizes a single fixed angle of incident X-rays, usually 35˚to the sample surface. All the 360˚omnidirectional diffracted X-rays are sampled by a 2-dimensional detector in a single exposure, producing an image of the complete Debye-Scherrer ring, for which the final residual stress measurement result is automatically determined. Fig. 7.1 and Fig. 7.2 show the X-Ray residual stress analyzer machine and printed cube samples on the substrate, respectively.

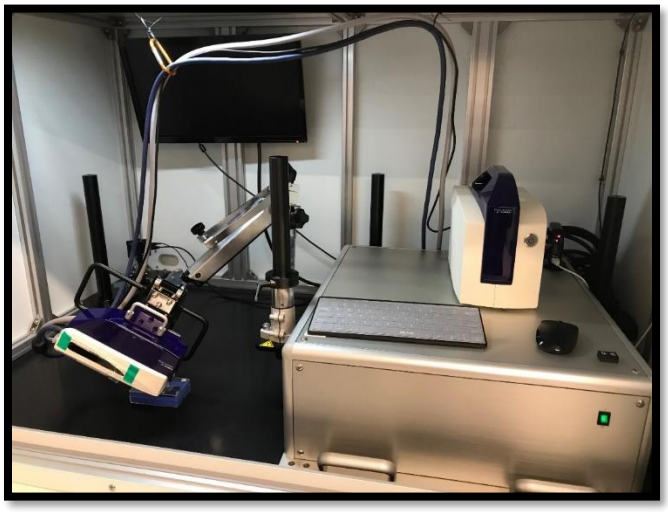

Fig. 7.1. X-Ray residual stress analyzer machine.

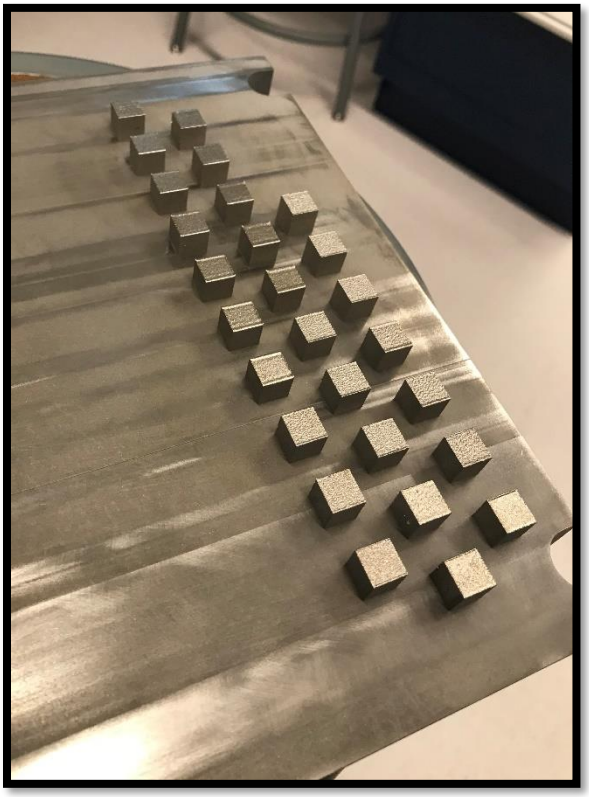

Fig. 7.2. Printed cube samples on the substrate.

7.3 Numerical approach

A 3-dimensional thermo-mechanical model using commercial COMSOL Multiphysics® software is developed for predicting the residual stresses of the cube samples. The following workflow (Fig. 7.3) is proposed for accelerating the simulation.

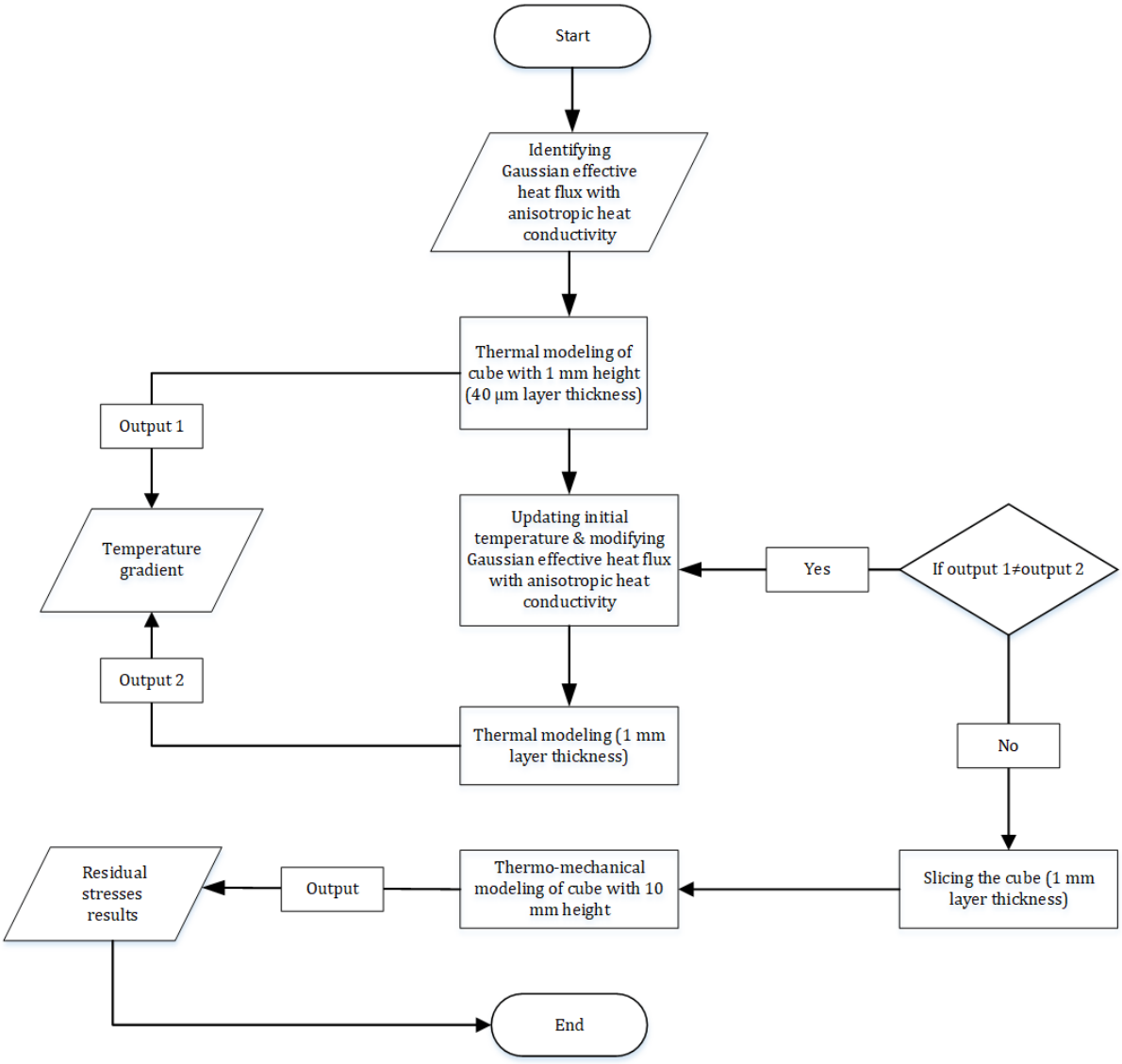

Fig. 7.3. The workflow of cube simulation.

7.3.1 A novel effective heat source model

The novel effective heat source model is proposed for accelerating the simulation of the cube samples. This heat source has a Gaussian profile which helps to accurately estimate the cooling rate

and temperature gradient during the process. Since the temperature gradient is the main cause of the induced residual stress within the fabricated sample [133], this heat source model provides an accurate prediction of the residual stress and deformation of the printed sample. Fig. 7.4 demonstrates the schematic of this heat source model.

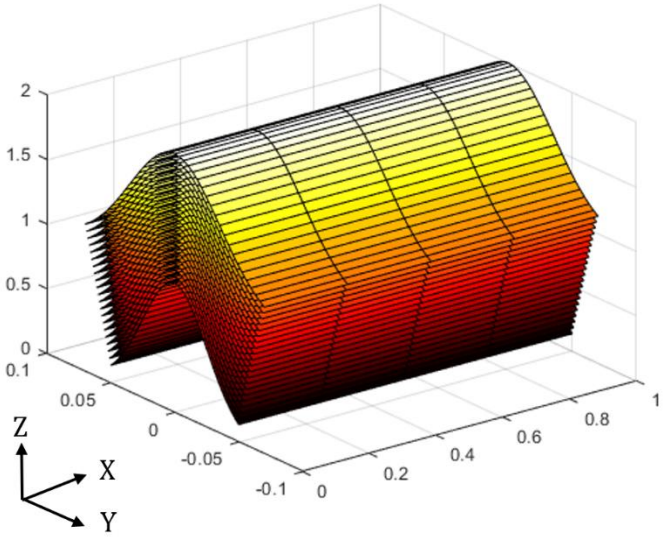

Fig. 7.4. Schematic of Gaussian effective heat flux.

In the following equation, the intensity distribution of the Gaussian effective heat flux is derived.

$$I(x,y,z) = q_0.\ exp\left[-2\frac{y^2}{r_0^2}\right] \tag{7.1}$$

$$r_0(z) = r_e + \frac{z}{H}(r_e - r_i) \tag{7.2}$$

Assuming the length of effective heat flux (L) is equal to the length of each heated band. Based on the energy conversation the following equation can be calculated. Moreover, the laser interaction time can be calculated based on the laser spot diameter (d) and scanning speed (V).

$$\beta.P.\frac{L}{V} = \frac{d}{V}.\int_0^H \int_{-\infty}^{\infty} \int_0^L q_0.\ \exp\left[-2\frac{y^2}{{r_0}^2}\right] dxdydz \tag{7.3}$$

By solving this integration the unknown parameter of q_0 will be derived as follows:

$$q_0 = \frac{\beta . P}{\sqrt{\pi/2}\, H \left[r_i + \frac{(r_e - r_i)}{2} \right] . d} \tag{7.4}$$

As a result, the final equation of the heat intensity distribution of the Gaussian effective heat source will be as follows:

$$I(x, y, z) = \frac{\beta . P}{\sqrt{\pi/2}\, H \left[r_i + \frac{(r_e - r_i)}{2} \right] . d} . \; exp\left[-2 \frac{y^2}{r_0^2} \right] \tag{7.5}$$

7.3.2 Thermal modeling of a cube with 1 mm

Simulation of the cube with 10 mm height based on 40 µm layer thickness is extremely time-consuming due to the huge number of layers (250 layers). Therefore, the problem is split into a simpler one considering the smaller domain size of a cube with 1 mm height. As a consequence, the building process simulation of the cube with 1 mm height is feasible, since only 25 layers are needed to be scanned. In the following Fig. 7.5 the simulation process of the cube with 1 mm height using the Gaussian effective heat flux with 90 µm hatch distance is shown.

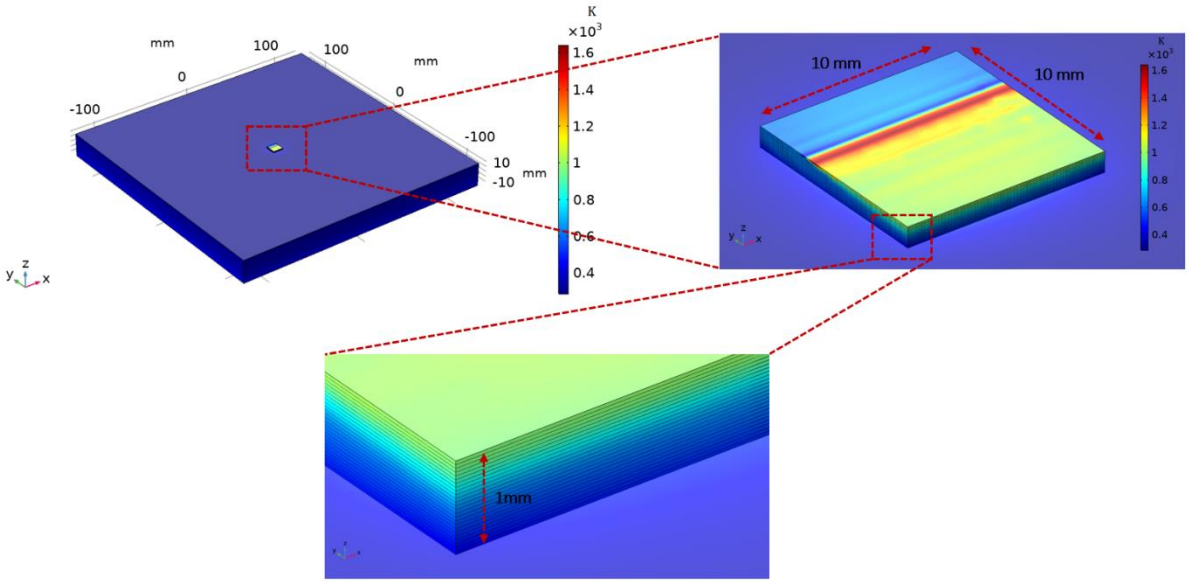

Fig. 7.5. The simulation process of building a cube with 1 mm height.

7.3.3 Enlarging layer thickness to 1 mm

In this step, for the acceleration of the simulation process, the layer thickness is enlarged to 1 mm. As a result, the number of layers for simulating the cube with 10 mm height is declined to 10 layers. To ensure the accuracy of the simulation and guaranty that a similar temperature gradient is achieved by enlarging the layer thickness, the comparison of the resultant temperature gradient between the simulation process of using 40 µm layer thickness and 1 mm layer thickness is conducted. Fig. 7.6 shows the simulation process of a cube with 1 mm height using 1 mm layer thickness and Fig. 7.7 demonstrates the resultant temperature gradient comparison between the simulation process of the cube with 1 mm height using 40 µm layer thickness and 1 mm layer thickness. However, in order to use a larger layer thickness some parameters of the heat source model should be modified. The height of the heat source model (H) and enhanced anisotropic heat conductivity coefficient λ are adjusted for acquiring a similar temperature gradient. As it is reported in the literature, the LPBF process induces anisotropic heat transfer in the Z direction which is along with the building direction [134]. Therefore, the enhanced anisotropic heat conductivity coefficient is used in modeling [59].

$$K_Z = \lambda . K \tag{7.6}$$

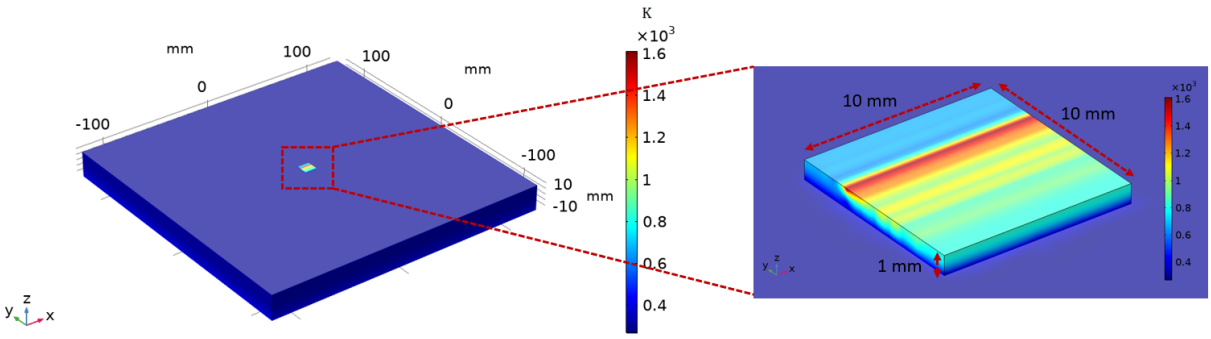

Fig. 7.6. The simulation process of the cube with 1 mm height using 1 mm layer thickness.

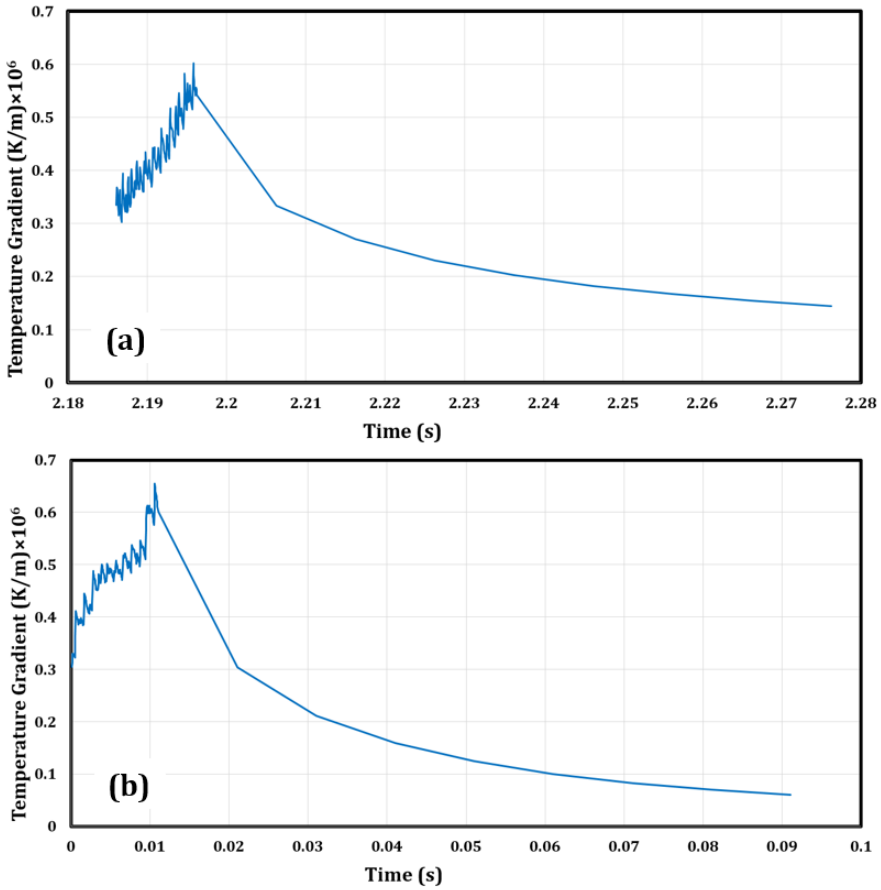

Fig. 7.7. Comparison between resultant temperature gradient between using a) 40 µm layer thickness and, b) 1 mm layer thickness.

As it is shown in Fig. 7.7, the temperature gradient provided by both simulations of the cube using 40 µm and 1 mm layer thickness has the same value. The maximum temperature gradient using 40 µm and 1 mm layer thickness is 5.9 $\times 10^5$ K/m and 6.5 $\times 10^5$ K/m, respectively which are close to each other and have the same trend.

7.3.4 Thermo-mechanical simulation of the cube with 10 mm height

Thermo-mechanical modeling of the cube with 10 mm height is developed using a Gaussian effective heat source. Besides, implementing a decoupled approach provides the benefit of decreasing the computational cost. Implementing active and deactivation of each layer is a common approach for simulating the LPBF process [90]. This approach is conducted using MATLAB code which is linked to the COMSOL software. Fig. 7.8 illustrates the schematic of the cube building process simulation.

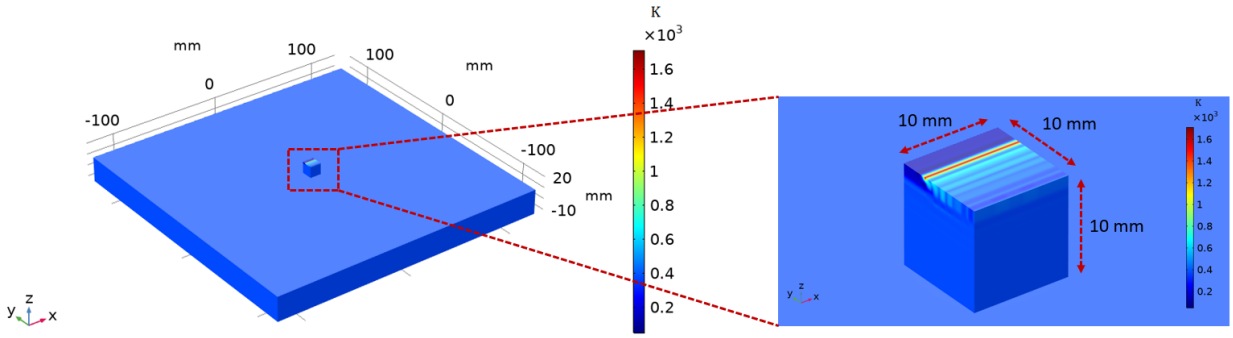

Fig. 7.8. The simulation of the cube building process with 10 mm height.

7.3.5 Mesh sensitivity analysis

To ensure the results are reliable depending on the number of elements, the mesh sensitivity analysis is conducted. Based on the analysis the number of elements 2761 is implemented which provides less computational time and sufficient accuracy. Fig. 7.9 shows three models have been created with a different number of elements to investigate the mesh sensitivity on the residual stress results.

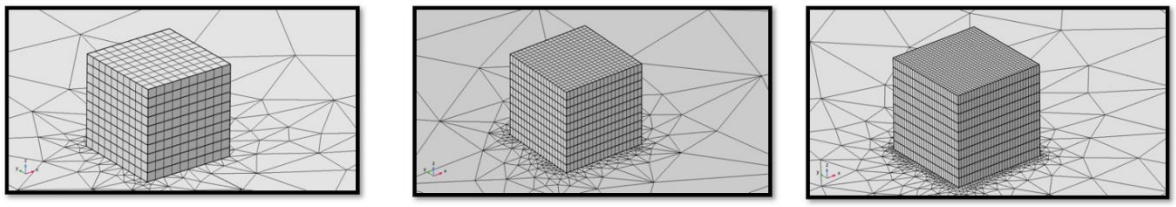

(a) (b) (c)

Fig. 7.9. The number of elements for mesh sensitivity analysis is a) 2761, b) 9018 and c) 18568.

Fig. 7.10 illustrates the residual stress results associated with using the different number of elements. Fig. 7.10 (a), (b), and (c) results are related to the number of elements 2760, 9018, and 18568 respectively. Based on the computational time and von Mises results, it is realized that using the 2761 number of elements would provide acceptable accuracy while saving computational time.

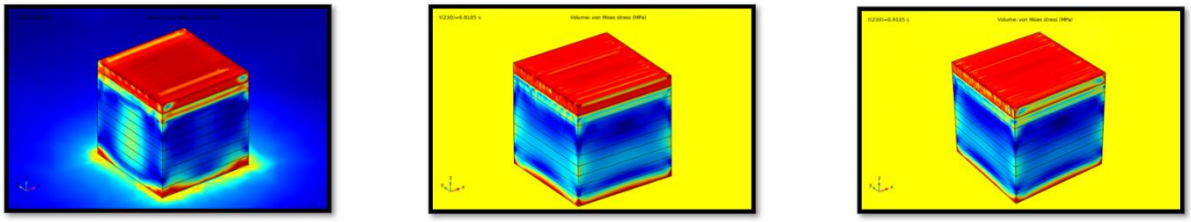

(a) (b) (c)

Fig. 7.10. The average residual stress results and computational time for mesh sensitivity analysis are a) 495 MPa, 1 h, and 30 min, b) 510 MPa, 10 h, and c) 518 MPa, 24 h.

7.3.6 Numerical results

The residual stresses in X (parallel to the laser scanning direction) and Y directions (transverse to the laser scanning direction) are obtained from numerical modeling. Also, the effect of laser process parameters on the induced residual stresses is investigated. In this case, different laser power 150 W, 200 W, and 250 W are used to study the effect of laser power on the residual stresses. The results show that by increasing the laser power the energy density provided by the laser heat source is elevated. As a result, the higher temperature gradient created during the process leads to the higher induced residual stresses within the printed parts. Besides, as reported in the literature, higher residual stresses occurred in the direction parallel to the laser scanning, which means that residual stresses in the X direction are higher than residual stresses in the Y direction [60], [135], [136]. The reason behind this is that, due to the higher heat flow in the longitudinal direction of the laser scanning, a higher temperature gradient is provided compared to the transverse direction.

The numerical results of the cube-building process simulation are shown in Fig. 7.11. The longitudinal residual stresses are much higher than the transverse residual stresses. Also, the residual stresses associated with laser power 250 W are significantly higher than the induced residual stresses of using lower laser power.

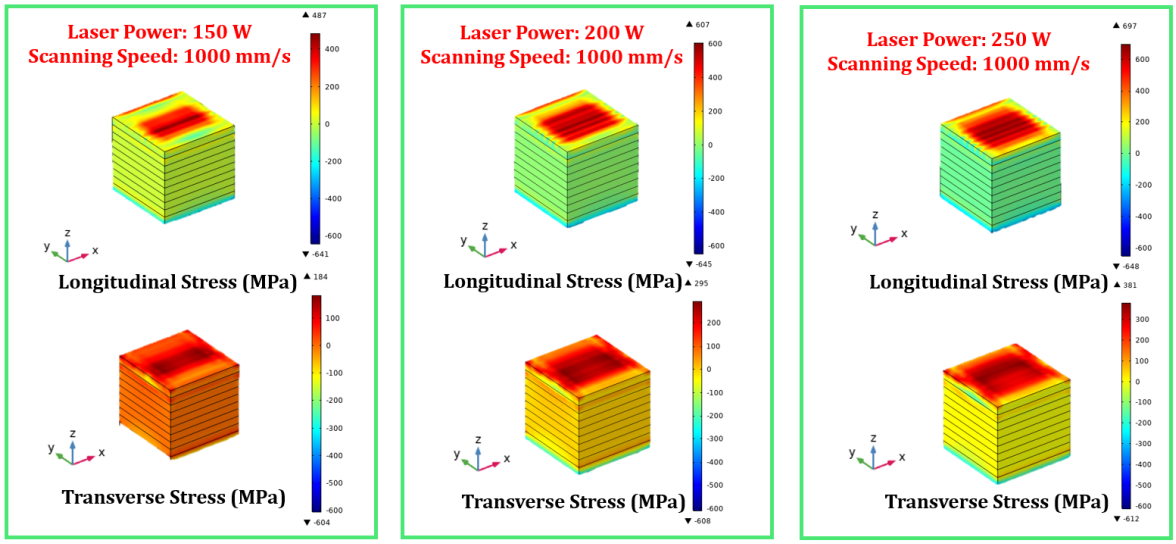

Fig. 7.11. Longitudinal and transverse residual stresses.

The residual stresses in X and Y directions are plotted along the specific line in the middle of the top surface of the cube sample. The maximum residual stresses in the X and Y directions are occurred in the middle area of the top surface due to the higher existence of the temperature gradient. The maximum residual stresses for the laser power 150 W, 200 W, and 250 W in the X direction are 362 MPa, 443 MPa, and 567 Mpa, respectively whereas, the maximum residual stresses for the laser power 150 W, 200 W and, 250 W in the Y direction are 189 MPa, 251 MPa and, 300 MPa. The residual stress plots in the longitudinal and transverse directions are shown in Fig. 7.12.

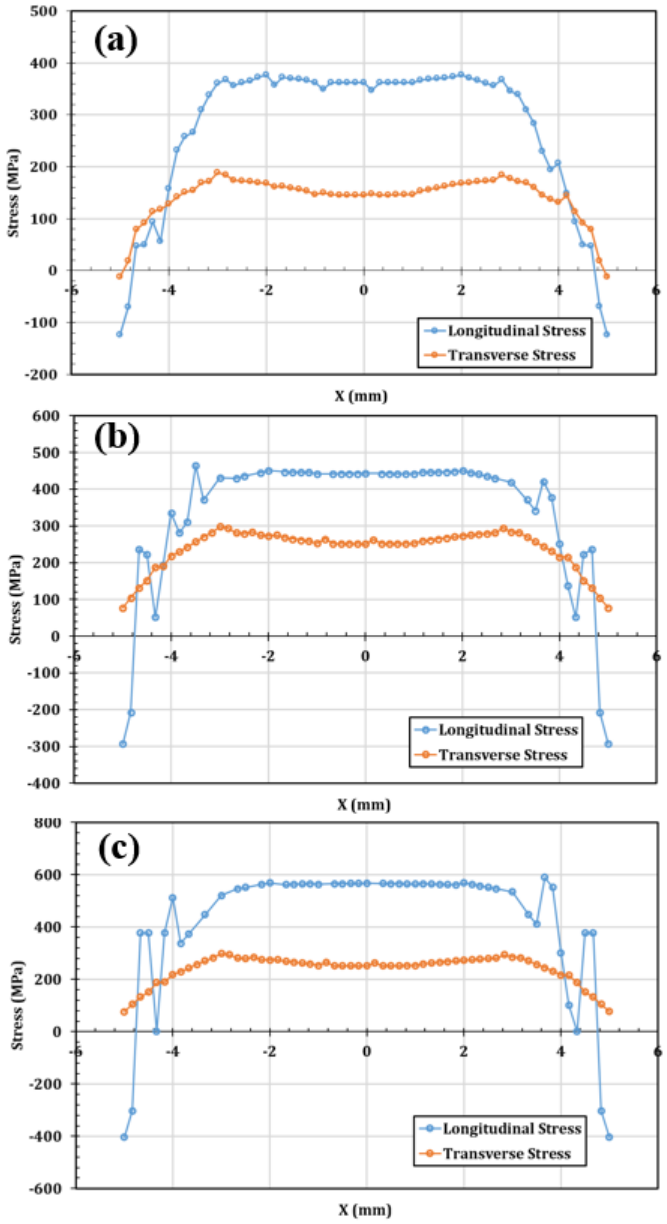

Fig. 7.12. Longitudinal and transverse residual stresses for different process parameters a) laser power 150 W, b) laser power 200 W and, c) laser power 250 W.

7.3.7 Validation of the simulation results

The accelerated thermo-mechanical model is validated with experimental results. The simulation results are in good agreement with experimental ones (Fig. 7.13). On the other hand, the total computational time for simulating a cube with 10 mm height is 1 h and 30 minutes. Therefore, this

developed thermo-mechanical model can predict residual stresses with high accuracy and less computational cost.

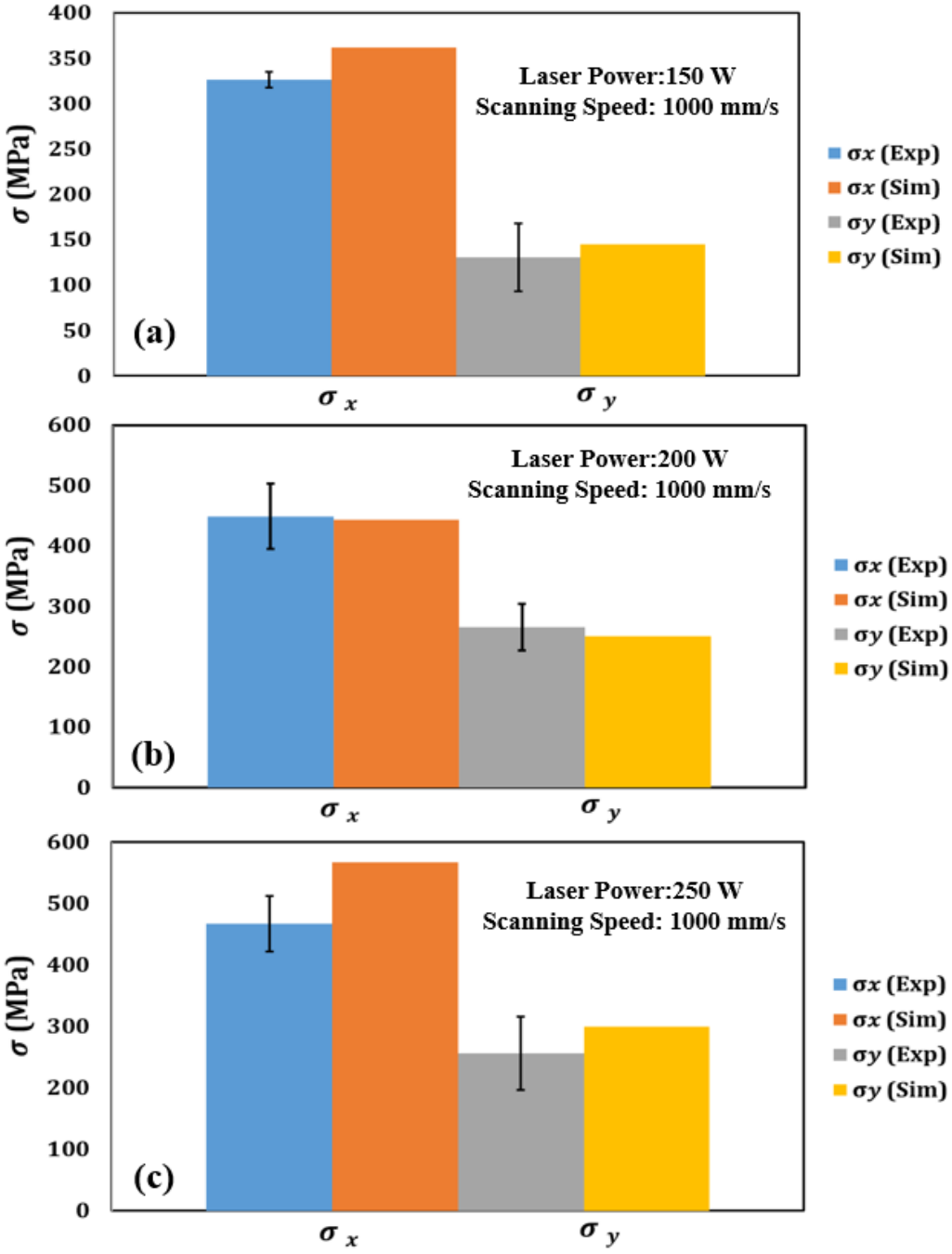

Fig. 7.13. The validation of the simulation results.

As discussed previously, the residual stresses in X directions are much higher than residual stresses in Y directions. On the other hand, by increasing the laser power while the scanning speed is constant at 1000 mm/s, the residual stresses are elevated due to providing higher energy density to the material. The percentage difference between simulation results and experimental ones for laser power 150 W, 200 W and, 250 W in the X direction are 11%, 1%, and 21%, respectively, whereas the percentage difference between simulation results and experimental ones for laser power 150 W, 200 W and, 250 W in the Y direction are 11%, 6%, and 17%.

7.4 Summary

In this chapter, an accelerated thermo-mechanical model is developed. A novel Gaussian effective heat source model is proposed which can reduce the computational cost significantly. Moreover, a decoupled approach of thermo-mechanical simulation is conducted which provides further acceleration of the numerical analysis. The procedure workflow of the cube simulation is proposed which includes enlarging the layer thickness while obtaining the accurate temperature gradient during the simulation process. This methodology enables to conduct fast cube-building process simulation which takes 1 h and 30 minutes and can predict the residual stress in the longitudinal and transverse directions accurately. The results show that the highest residual stress occurs in the middle region of the top surface due to the existence of a higher temperature gradient. In addition, the simulation and experimental results indicate that residual stresses in the longitudinal direction which is parallel to the laser scanning direction are much higher than residual stress in the transverse directions. The validation of the simulation results is conducted using different process parameters. The effect of the laser power on the residual stresses is investigated. It is concluded that increasing the laser power provides a higher energy density to the material. As a consequence, a higher temperature gradient is going to be generated during the process which results in higher residual stresses. The results show that by elevating the laser power from 150 W to 250 W residual stresses in the X rise 46%, whereas the residual stresses in the Y direction increase two times approximately. The developed thermo-mechanical model enables us to predict residual stresses with high accuracy and low computational cost. The percentage difference between simulation results and experimental ones for laser power 150 W, 200 W and, 250 W in the X direction are 11%, 1%, and 21%, respectively, whereas the percentage difference between simulation results and experimental ones for laser power 150 W, 200 W and, 250 W in the Y direction are 11%, 6%, and 17%.

Chapter 8. Conclusions and Future work

8.1 Conclusions

In this work, the LPBF modeling is categorized into two different groups of micro/mesoscale and macroscale. In the micro/mesoscale simulation, the thermal fields such as temperature distribution, cooling rate, temperature gradient within the melt pool are extracted to be used for microstructure analysis, such as predicting the cell size. On the other hand, due to inducing high-temperature gradients during the process, high residual stresses and deformation can cause the failure of the manufactured part. Therefore, in the macroscale simulation, the residual stress and deformation are predicted for avoiding trial-and-error experimental tests leading to a reduction in the development and manufacturing costs. However, there are some challenges in the modeling process, such as high computational costs and acquiring an acceptable accuracy for predicting residual stress and deformation. Therefore, novel effective heat flux is proposed for accelerating thermo-mechanical simulation.

Based on the developed model following conclusions can be drawn:

1- Implementing a volumetric heat source model (Conical-Gaussian) provides a more accurate temperature distribution during the process.

2- The heat source parameters are calibrated based on a comparison between simulation and experimental melt pool dimensions. The percentage difference between simulated and experimental melt pool depth and width results are around 13% and 6%, respectively.

3- It is concluded that the effect of laser power on the melt pool geometry is more dominant than the scanning speed, and by elevating the energy density, the melt pool dimensions are increased.

4- The experimental results show that by decreasing the thicknesses of thin-walls melt pool dimensions (melt pool width) are increased significantly. The melt pool dimensions result shows that with increasing thicknesses 0.5 mm to 1 mm, the melt pool width decreases 45%.

5- The simulation results showed strong reliability as they were comparable to experimental ones. the percentage difference for the edge tracks of thin-wall thicknesses 0.5 mm, 0.75 mm, and 1 mm were 9%, 7%, and 5%, respectively.

6- The thermo-mechanical analysis modeling of multi-track multi-layer was carried out. It is found that the highest longitudinal residual stress and deformation is induced on the top layer of the geometry.

7- A novel Gaussian effective heat source model is proposed which can reduce the computational cost significantly. By using this methodology, the cube building process simulation only takes 1 h and 30 minutes and can predict the residual stress in the longitudinal and transverse directions accurately.

8- The results show that the highest residual stress occurs in the middle region of the top surface of the cube due to the existence of a higher temperature gradient. In addition, the simulation and experimental results indicate that residual stresses in the longitudinal direction, which is parallel to the laser scanning direction, are much higher than residual stress in the transverse directions.

9- The effect of the laser power on the residual stresses is investigated. It is concluded that increasing the laser power provides a higher energy density to the material. As a consequence, a higher temperature gradient is going to be generated during the process, which results in higher residual stresses.

10- The percentage difference between cube building process simulation results and experimental ones for laser power 150 W, 200 W and, 250 W in the X direction are 11%, 1%, and 21%, respectively, whereas the percentage difference between simulation results and experimental ones for laser power 150 W, 200 W and, 250 W in the Y direction are 11%, 6%, and 17%.

8.2 Future work

In the future the following tasks can be pursued:

1- The effect of layer thickness on melt pool dimensions and temperature distribution can be investigated. In addition, it is worth investigating the effect of hatch distance on the temperature distribution and porosity of the final printed parts.

2- Implementing adaptive mesh while using a volumetric heat source can be developed in the future to further accelerate the simulation in the microscale model.

3- Different scanning strategies can be implemented in the modeling to investigate the effect of different scanning patterns on final residual stresses and deformations.

4- Thermo-mechanical modeling can be validated by measuring the deformation of the printed parts. Simulation of the building process of cantilever parts can be investigated for predicting deformations.

5- An accelerated thermo-mechanical model using an effective heat flux can be programmed (C++ language) in open source software such as Deal II which can be utilized in parallel computing for further acceleration.

Letter of Copyright Permission

CCC | RightsLink®

Home | Help | Live Chat | Shahriar Imani Shahabad

SPRINGER NATURE

Heat source model calibration for thermal analysis of laser powder-bed fusion

Author: Shahriar Imani Shahabad et al
Publication: The International Journal of Advanced Manufacturing Technology
Publisher: Springer Nature
Date: Jan 5, 2020

Order Completed

Thank you for your order.

This Agreement between University of Waterloo -- Shahriar Imani Shahabad ("You") and Springer Nature ("Springer Nature") consists of your license details and the terms and conditions provided by Springer Nature and Copyright Clearance Center.

Your confirmation email will contain your order number for future reference.

License Number	5100830270830
License date	Jul 02, 2021

Printable Details

CCC | RightsLink®

Home | Help | Live Chat | Shahriar Imani Shahabad

Mesoscopic simulation model of selective laser melting of stainless steel powder

Author: Saad A. Khairallah,Andy Anderson
Publication: Journal of Materials Processing Technology
Publisher: Elsevier
Date: November 2014

Order Completed

Thank you for your order.

This Agreement between University of Waterloo -- Shahriar Imani Shahabad ("You") and Elsevier ("Elsevier") consists of your license details and the terms and conditions provided by Elsevier and Copyright Clearance Center.

Your confirmation email will contain your order number for future reference.

License Number	5100850258088
License date	Jul 02, 2021

Printable Details

References

[1] S. Waqar, K. Guo, and J. Sun, “FEM analysis of thermal and residual stress profile in selective laser melting of 316L stainless steel,” *J. Manuf. Process.*, vol. 66, no. November 2020, pp. 81–100, 2021.

[2] R. Esmaeilizadeh *et al.*, “Customizing mechanical properties of additively manufactured Hastelloy X parts by adjusting laser scanning speed,” *J. Alloys Compd.*, vol. 812, p. 152097, 2020.

[3] B. Ahmad, S. O. van der Veen, M. E. Fitzpatrick, and H. Guo, “Residual stress evaluation in selective-laser-melting additively manufactured titanium (Ti-6Al-4V) and inconel 718 using the contour method and numerical simulation,” *Addit. Manuf.*, vol. 22, no. June, pp. 571–582, 2018.

[4] Z. Li, S. Yang, B. Liu, W. Liu, Z. Kuai, and Y. Nie, “Simulation of temperature field and stress field of selective laser melting of multi-layer metal powder,” *Opt. Laser Technol.*, vol. 140, no. November 2020, 2021.

[5] M. Shiomi, K. Osakada, K. Nakamura, T. Yamashita, and F. Abe, “Residual stress within metallic model made by selective laser melting process,” *CIRP Ann. - Manuf. Technol.*, vol. 53, no. 1, pp. 195–198, 2004.

[6] Y. Liu, Y. Yang, and D. Wang, “A study on the residual stress during selective laser melting (SLM) of metallic powder,” *Int. J. Adv. Manuf. Technol.*, vol. 87, no. 1–4, pp. 647–656, 2016.

[7] B. Liu, G. Fang, and L. Lei, “An analytical model for rapid predicting molten pool geometry of selective laser melting (SLM),” *Appl. Math. Model.*, vol. 92, pp. 505–524, 2021.

[8] Y. Tian, L. Yang, D. Zhao, Y. Huang, and J. Pan, “Numerical analysis of powder bed generation and single track forming for selective laser melting of SS316L stainless steel,” *J. Manuf. Process.*, vol. 58, no. July, pp. 964–974, 2020.

[9] W. Zhang, M. Tong, and N. M. Harrison, “Scanning strategies effect on temperature, residual stress and deformation by multi-laser beam powder bed fusion manufacturing,” *Addit. Manuf.*, vol. 36, no. July, p. 101507, 2020.

[10] Z. C. Fang, Z. L. Wu, C. G. Huang, and C. W. Wu, “Review on residual stress in selective laser melting additive manufacturing of alloy parts,” *Opt. Laser Technol.*, vol. 129, no. 15, p.

106283, 2020.

[11] P. Köhnen, S. Ewald, J. H. Schleifenbaum, A. Belyakov, and C. Haase, “Controlling microstructure and mechanical properties of additively manufactured high-strength steels by tailored solidification,” *Addit. Manuf.*, vol. 35, no. May, p. 101389, 2020.

[12] Z. Zhang, P. Ge, X. X. Yao, T. Li, and W. W. Liu, “Numerical studies of residual states and scaling effects in laser-directed energy deposition additive manufacturing,” *Int. J. Adv. Manuf. Technol.*, vol. 108, no. 4, pp. 1233–1247, 2020.

[13] M. Ghasri-Khouzani *et al.*, “Experimental measurement of residual stress and distortion in additively manufactured stainless steel components with various dimensions,” *Mater. Sci. Eng. A*, vol. 707, no. September, pp. 689–700, 2017.

[14] A. Keshavarzkermani *et al.*, “Static recrystallization impact on grain structure and mechanical properties of heat-treated Hastelloy X produced via laser powder-bed fusion,” *Mater. Charact.*, vol. 173, no. February, p. 110969, 2021.

[15] M. Liu *et al.*, “A characteristic time-based heat input model for selective laser melting,” *Addit. Manuf.*, vol. 44, no. May, p. 102026, 2021.

[16] P. Stavropoulos and P. Foteinopoulos, “Modelling of additive manufacturing processes : a review and classi fi cation,” *Manuf. Rev.*, vol. 2, 2018.

[17] H. Fayazfar *et al.*, “A critical review of powder-based additive manufacturing of ferrous alloys: Process parameters, microstructure and mechanical properties,” *Mater. Des.*, vol. 144, pp. 98–128, 2018.

[18] “Additive Manufacturing: 3D printed gas turbine blades.” [Online]. Available: https://www.digitalengineering247.com/article/siemens-3d-prints-power-turbine-blades/.

[19] J. Ning, M. Praniewicz, W. Wang, J. R. Dobbs, and S. Y. Liang, “Analytical modeling of part distortion in metal additive manufacturing,” *Int. J. Adv. Manuf. Technol.*, vol. 107, no. 1–2, pp. 49–57, 2020.

[20] K. H. Lee and G. J. Yun, “A novel heat source model for analysis of melt Pool evolution in selective laser melting process,” *Addit. Manuf.*, vol. 36, no. July, p. 101497, 2020.

[21] D. Soldner and J. Mergheim, “Thermal modelling of selective beam melting processes using heterogeneous time step sizes,” *Comput. Math. with Appl.*, vol. 78, no. 7, pp. 2183–2196,

2019.

[22] C. Li, M. F. Gouge, E. R. Denlinger, J. E. Irwin, and P. Michaleris, “Estimation of part-to-powder heat losses as surface convection in laser powder bed fusion,” *Addit. Manuf.*, vol. 26, no. August 2018, pp. 258–269, 2019.

[23] Y. Yang, F. van Keulen, and C. Ayas, “A computationally efficient thermal model for selective laser melting,” *Addit. Manuf.*, vol. 31, no. November 2019, p. 100955, 2020.

[24] W. C. McGaghie, “A critical review of simulation,” pp. 1–3, 2018.

[25] M. Galati, A. Snis, and L. Iuliano, “Powder bed properties modelling and 3D thermo-mechanical simulation of the additive manufacturing Electron Beam Melting process,” *Addit. Manuf.*, vol. 30, no. April, p. 100897, 2019.

[26] Z. Luo and Y. Zhao, “Efficient thermal finite element modeling of selective laser melting of Inconel 718,” *Comput. Mech.*, no. 0123456789, 2019.

[27] P. S. Cook and A. B. Murphy, “Simulation of melt pool behaviour during additive manufacturing : Underlying physics and progress,” *Addit. Manuf.*, vol. 31, no. May 2019, p. 100909, 2020.

[28] S. Saxena, R. Sharma, and A. Kumar, “A Microscale Study of Thermal Field and Stresses during Processing of Ti6Al4V Powder Layer by Selective Laser Melting,” *Lasers Manuf. Mater. Process.*, vol. 5, no. 4, pp. 335–365, 2018.

[29] S. Ancellotti *et al.*, “Numerical/experimental strategies to infer enhanced liquid thermal conductivity and roughness in laser powder-bed fusion processes,” *Addit. Manuf.*, vol. 27, no. April, pp. 552–564, 2019.

[30] R. Yavari *et al.*, “Thermal modeling in metal additive manufacturing using graph theory – Application to laser powder bed fusion of a large volume impeller,” *Addit. Manuf.*, vol. 41, no. October 2020, p. 101956, 2021.

[31] P. Promoppatum, S. Yao, P. C. Pistorius, and A. D. Rollett, “A Comprehensive Comparison of the Analytical and Numerical Prediction of the Thermal History and Solidification Microstructure of Inconel 718 Products Made by Laser Powder-Bed Fusion,” *Engineering*, vol. 3, no. 5, pp. 685–694, 2017.

[32] W. Huang and Y. Zhang, “Finite element simulation of thermal behavior in single-track

multiple-layers thin wall without-support during selective laser melting," *J. Manuf. Process.*, vol. 42, no. April, pp. 139–148, 2019.

[33] M. J. Ansari, D. S. Nguyen, and H. S. Park, "Investigation of SLM process in terms of temperature distribution and melting pool size: Modeling and experimental approaches," *Materials (Basel).*, vol. 12, no. 8, 2019.

[34] Y. M. Arısoy, L. E. Criales, and T. Özel, "Modeling and simulation of thermal field and solidification in laser powder bed fusion of nickel alloy IN625," *Opt. Laser Technol.*, vol. 109, no. June 2018, pp. 278–292, 2019.

[35] C. Körner, E. Attar, and P. Heinl, "Mesoscopic simulation of selective beam melting processes," *J. Mater. Process. Technol.*, vol. 211, no. 6, pp. 978–987, 2011.

[36] C. Körner, A. Bauereiß, and E. Attar, "Fundamental consolidation mechanisms during selective beam melting of powders," *Model. Simul. Mater. Sci. Eng.*, vol. 21, no. 8, 2013.

[37] F. J. Gürtler, M. Karg, K. H. Leitz, and M. Schmidt, "Simulation of laser beam melting of steel powders using the three-dimensional volume of fluid method," *Phys. Procedia*, vol. 41, no. July 2017, pp. 881–886, 2013.

[38] S. A. Khairallah and A. Anderson, "Mesoscopic simulation model of selective laser melting of stainless steel powder," *J. Mater. Process. Technol.*, vol. 214, no. 11, pp. 2627–2636, 2014.

[39] S. A. Khairallah, A. T. Anderson, A. M. Rubenchik, and W. E. King, "Laser powder-bed fusion additive manufacturing: Physics of complex melt flow and formation mechanisms of pores, spatter, and denudation zones," *Addit. Manuf. Handb. Prod. Dev. Def. Ind.*, vol. 108, pp. 613–628, 2017.

[40] C. Panwisawas *et al.*, "Mesoscale modelling of selective laser melting: Thermal fluid dynamics and microstructural evolution," *Comput. Mater. Sci.*, vol. 126, pp. 479–490, 2017.

[41] Y. C. Wu *et al.*, "Numerical modeling of melt-pool behavior in selective laser melting with random powder distribution and experimental validation," *J. Mater. Process. Technol.*, vol. 254, pp. 72–78, 2018.

[42] M. A. Russell, A. Souto-Iglesias, and T. I. Zohdi, "Numerical simulation of Laser Fusion Additive Manufacturing processes using the SPH method," *Comput. Methods Appl. Mech. Eng.*, vol. 341, pp. 163–187, 2018.

[43] Z. Wang, W. Yan, W. K. Liu, and M. Liu, “Powder-scale multi-physics modeling of multi-layer multi-track selective laser melting with sharp interface capturing method,” *Comput. Mech.*, 2018.

[44] K. Antony, N. Arivazhagan, and K. Senthilkumaran, “Numerical and experimental investigations on laser melting of stainless steel 316L metal powders,” *J. Manuf. Process.*, vol. 16, no. 3, pp. 345–355, 2014.

[45] Y. Li and D. Gu, “Parametric analysis of thermal behavior during selective laser melting additive manufacturing of aluminum alloy powder,” *Mater. Des.*, vol. 63, pp. 856–867, 2014.

[46] L. E. Loh *et al.*, “Numerical investigation and an effective modelling on the Selective Laser Melting (SLM) process with aluminium alloy 6061,” *Int. J. Heat Mass Transf.*, vol. 80, pp. 288–300, 2015.

[47] Y. Huang, L. J. Yang, X. Z. Du, and Y. P. Yang, “Finite element analysis of thermal behavior of metal powder during selective laser melting,” *Int. J. Therm. Sci.*, vol. 104, pp. 146–157, 2016.

[48] A. Foroozmehr, M. Badrossamay, E. Foroozmehr, and S. Golabi, “Finite Element Simulation of Selective Laser Melting process considering Optical Penetration Depth of laser in powder bed,” *Mater. Des.*, vol. 89, pp. 255–263, 2016.

[49] S. Liu, H. Zhu, G. Peng, J. Yin, and X. Zeng, “Microstructure prediction of selective laser melting AlSi10Mg using finite element analysis,” *Mater. Des.*, vol. 142, pp. 319–328, 2018.

[50] E. R. Denlinger, V. Jagdale, G. V. Srinivasan, T. El-Wardany, and P. Michaleris, “Thermal modeling of Inconel 718 processed with powder bed fusion and experimental validation using in situ measurements,” *Addit. Manuf.*, vol. 11, pp. 7–15, 2016.

[51] S. Roy, M. Juha, M. S. Shephard, and A. M. Maniatty, “Heat transfer model and finite element formulation for simulation of selective laser melting,” *Comput. Mech.*, pp. 1–12, 2017.

[52] H. Hu, X. Ding, and L. Wang, “Numerical analysis of heat transfer during multi-layer selective laser melting of AlSi10Mg,” *Opt. - Int. J. Light Electron Opt.*, vol. 127, no. 20, pp. 8883–8891, 2016.

[53] Y. Fu, C and Guo, *3-Dimensional finite element modeling of selective laser melting Ti-6Al-4V alloy*. 25th Annual International Solid Freeform Fabrication Symposium, 2014.

[54] Y. Liu, J. Zhang, and Z. Pang, “Numerical and experimental investigation into the subsequent thermal cycling during selective laser melting of multi-layer 316L stainless steel,” *Opt. Laser Technol.*, vol. 98, pp. 23–32, 2018.

[55] H. Ali, H. Ghadbeigi, and K. Mumtaz, “Residual stress development in selective laser-melted Ti6Al4V : a parametric thermal modelling approach Residual stress development in selective laser-melted Ti6Al4V : a parametric thermal modelling approach,” no. May, 2018.

[56] E. Kundakc *et al.*, “Thermal and molten pool model in selective laser melting process of Inconel 625,” *Int. J. Adv. Manuf. Technol.*, 2018.

[57] Y. Du, X. You, F. Qiao, L. Guo, and Z. Liu, “A model for predicting the temperature field during selective laser melting,” *Results Phys.*, vol. 12, no. November 2018, pp. 52–60, 2019.

[58] A. K. Mishra and A. Kumar, “Numerical and experimental analysis of the effect of volumetric energy absorption in powder layer on thermal-fluidic transport in selective laser melting of Ti6Al4V,” *Opt. Laser Technol.*, vol. 111, no. July 2018, pp. 227–239, 2019.

[59] Z. Zhang *et al.*, “3-Dimensional heat transfer modeling for laser powder-bed fusion additive manufacturing with volumetric heat sources based on varied thermal conductivity and absorptivity,” *Opt. Laser Technol.*, vol. 109, pp. 297–312, Jan. 2019.

[60] M. F. Zaeh and G. Branner, “Investigations on residual stresses and deformations in selective laser melting,” *Prod. Eng.*, vol. 4, no. 1, pp. 35–45, 2010.

[61] L. Papadakis and A. Loizou, “A thermo-mechanical modeling reduction approach for calculating shape distortion in SLM manufacturing for aero engine components,” *Int. Conf. Adv. Res. Virtual Rapid Prototyp.*, pp. 613–618, 2013.

[62] N. Keller and V. Ploshikhin, “New Method for Fast Predictions of Residual Stress and Distortions of AM Parts,” *Solid Free. Fabr. Symp.*, pp. 1229–1237, 2014.

[63] E. R. Denlinger, J. Irwin, and P. Michaleris, “Thermomechanical Modeling of Additive Manufacturing Large Parts,” *J. Manuf. Sci. Eng.*, vol. 136, no. 6, p. 061007, 2014.

[64] C. Li, J. F. Liu, X. Y. Fang, and Y. B. Guo, “Efficient predictive model of part distortion and residual stress in selective laser melting,” *Addit. Manuf.*, vol. 17, no. October, pp. 157–168, 2017.

[65] S. Jayanath and A. Achuthan, “A Computationally Efficient Finite Element Framework to

Simulate Additive Manufacturing Processes," *J. Manuf. Sci. Eng.*, vol. 140, no. 4, p. 041009, 2018.

[66] C. Li, Z. Y. Liu, X. Y. Fang, and Y. B. Guo, "On the Simulation Scalability of Predicting Residual Stress and Distortion in Selective Laser Melting," *J. Manuf. Sci. Eng.*, vol. 140, no. 4, p. 041013, 2018.

[67] L. Cheng, Q. Chen, A. C. To, X. Liang, and Q. Yang, "A modified method for estimating inherent strains from detailed process simulation for fast residual distortion prediction of single-walled structures fabricated by directed energy deposition," *Addit. Manuf.*, vol. 23, no. July, pp. 471–486, 2018.

[68] Y. Zhang, G. Guillemot, M. Bernacki, and M. Bellet, "Macroscopic thermal finite element modelling of additive metal manufacturing by selective laser melting process," *Comput. Methods Appl. Mech. Eng.*, 2017.

[69] P. Promoppatum *et al.*, "Numerical modeling and experimental validation of thermal history and microstructure for additive manufacturing of an Inconel 718 product," *Prog. Addit. Manuf.*, vol. 3, no. 1–2, pp. 15–32, 2018.

[70] M. Schänzel, D. Shakirov, A. Ilin, and V. Ploshikhin, "Coupled thermo-mechanical process simulation method for selective laser melting considering phase transformation steels," *Comput. Math. with Appl.*, no. xxxx, 2019.

[71] Z. Zhang, "Coupled Topology and Process Optimization for Laser Powder-Bed Fusion Additive Manufacturing," *UWSpace*, 2019.

[72] O. C. Zienkiewicz and R. L. Taylor, *The finite element method for solid and structural mechanics*. Elsevier, 2005.

[73] P. Kelly, "Mechanics Lecture Notes: Engineering Solid Mechanics. Available from http://homepages.engineering.auckland.ac.nz/~pkel015/SolidMechanicsBooks/index.html." .

[74] K. KRABBENHØFT, "BASIC COMPUTATIONAL PLASTICITY," 2002.

[75] K. J. Bathe, *Finite element procedures*. 2006.

[76] M. Mozaffar, E. Ndip-Agbor, S. Lin, G. J. Wagner, K. Ehmann, and J. Cao, "Acceleration strategies for explicit finite element analysis of metal powder-based additive manufacturing processes using graphical processing units," *Comput. Mech.*, vol. 64, no. 3, pp. 879–894,

2019.

[77] J. Wu, L. Wang, and X. An, “Numerical analysis of residual stress evolution of AlSi10Mg manufactured by selective laser melting,” *Optik (Stuttg).*, vol. 137, pp. 65–78, 2017.

[78] P. Tan, F. Shen, B. Li, and K. Zhou, “A thermo-metallurgical-mechanical model for selective laser melting of Ti6Al4V,” *Mater. Des.*, vol. 168, p. 107642, Apr. 2019.

[79] D. Ramos, F. Belblidia, and J. Sienz, “New scanning strategy to reduce warpage in additive manufacturing,” *Addit. Manuf.*, vol. 28, pp. 554–564, Aug. 2019.

[80] M. Chiumenti *et al.*, “Numerical modelling and experimental validation in Selective Laser Melting,” *Addit. Manuf.*, vol. 18, pp. 171–185, 2017.

[81] C. Luo, J. Qiu, Y. Yan, J. Yang, C. Uher, and X. Tang, “Finite element analysis of temperature and stress fields during the selective laser melting process of thermoelectric SnTe,” *J. Mater. Process. Technol.*, vol. 261, no. February, pp. 74–85, 2018.

[82] H. Peng *et al.*, “Fast prediction of thermal distortion in metal powder bed fusion additive manufacturing: Part 2, a quasi-static thermo-mechanical model,” *Addit. Manuf.*, vol. 22, no. 2010, pp. 869–882, 2018.

[83] C. S. Wu, H. G. Wang, and Y. M. Zhang, “A new heat source model for keyhole plasma arc welding in FEM analysis of the temperature profile,” *Weld. J.*, vol. 85, no. 12, p. 284, 2006.

[84] A. Bonakdar, M. Molavi-Zarandi, A. Chamanfar, M. Jahazi, A. Firoozrai, and E. Morin, “Finite element modeling of the electron beam welding of Inconel-713LC gas turbine blades,” *J. Manuf. Process.*, vol. 26, pp. 339–354, 2017.

[85] R. Esmaeilizadeh, U. Ali, A. Keshavarzkermani, Y. Mahmoodkhani, E. Marzbanrad, and E. Toyserkani, “On the effect of spatter particles distribution on the quality of Hastelloy X parts made by laser powder-bed fusion additive manufacturing,” *J. Manuf. Process.*, vol. 37, no. November 2018, pp. 11–20, 2019.

[86] U. Ali *et al.*, “On the measurement of relative powder-bed compaction density in powder-bed additive manufacturing processes,” *Mater. Des.*, vol. 155, pp. 495–501, Oct. 2018.

[87] S. S. Sih and J. W. Barlow, “The prediction of the emissivity and thermal conductivity of powder beds,” *Part. Sci. Technol.*, vol. 22, no. 4, pp. 427–440, 2004.

[88] S. I. Shahabad, G. Karimi, and E. Toyserkani, “An Extended Rosenthal ’ s Model for Laser Powder-Bed Fusion Additive Manufacturing : Energy Auditing of Thermal Boundary Conditions,” *Lasers Manuf. Mater. Process.*, pp. 1–24, 2021.

[89] M. S. Khan, S. I. Shahabad, M. Yavuz, W. W. Duley, E. Biro, and Y. Zhou, “Numerical modelling and experimental validation of the effect of laser beam defocusing on process optimization during fiber laser welding of automotive press-hardened steels,” *J. Manuf. Process.*, vol. 67, no. February, pp. 535–544, 2021.

[90] M. Gouge and P. Michaleris, *Thermo-mechanical modeling of additive manufacturing*, First edit. Elsevier Inc., 2017.

[91] B. M. Kreith F, Manglik RM, *Principles of heat transfer*. Cengage Learning, 2012.

[92] J. Trapp, A. M. Rubenchik, G. Guss, and M. J. Matthews, “In situ absorptivity measurements of metallic powders during laser powder-bed fusion additive manufacturing,” *Appl. Mater. Today*, vol. 9, pp. 341–349, 2017.

[93] A. Keshavarzkermani *et al.*, “An investigation into the effect of process parameters on melt pool geometry, cell spacing, and grain refinement during laser powder bed fusion,” *Opt. Laser Technol.*, vol. 116, no. January, pp. 83–91, 2019.

[94] R. Acharya, J. A. Sharon, and A. Staroselsky, “Prediction of microstructure in laser powder bed fusion process,” *Acta Mater.*, vol. 124, pp. 360–371, 2017.

[95] K. Darvish, Z. W. Chen, M. A. L. Phan, and T. Pasang, “Materials Characterization Selective laser melting of Co-29Cr-6Mo alloy with laser power 180 – 360 W : Cellular growth , intercellular spacing and the related thermal condition,” *Mater. Charact.*, vol. 135, no. November 2017, pp. 183–191, 2018.

[96] W. Kurz and R. Trivedi, “Rapid solidification processing and microstructure formation,” vol. 17, pp. 46–51, 1994.

[97] S. Kou, *Welding Metallurgy*. 2002.

[98] N. J. Harrison, I. Todd, and K. Mumtaz, “Reduction of micro-cracking in nickel superalloys processed by Selective Laser Melting: A fundamental alloy design approach,” *Acta Mater.*, vol. 94, pp. 59–68, 2015.

[99] V. Gunenthiram, P. Peyre, M. Schneider, M. Dal, F. Coste, and R. Fabbro, “Analysis of laser–

melt pool–powder bed interaction during the selective laser melting of a stainless steel," *J. Laser Appl.*, vol. 29, no. 2, p. 022303, 2017.

[100] C. Obidigbo, E. P. Tatman, and J. Gockel, "Processing parameter and transient effects on melt pool geometry in additive manufacturing of Invar 36," *Int. J. Adv. Manuf. Technol.*, vol. 104, no. 5–8, pp. 3139–3146, 2019.

[101] L. Thijs, F. Verhaeghe, T. Craeghs, J. Van Humbeeck, and J. P. Kruth, "A study of the microstructural evolution during selective laser melting of Ti-6Al-4V," *Acta Mater.*, vol. 58, no. 9, pp. 3303–3312, 2010.

[102] Q. Chen, G. Guillemot, C. A. Gandin, and M. Bellet, "Three-dimensional finite element thermomechanical modeling of additive manufacturing by selective laser melting for ceramic materials," *Addit. Manuf.*, vol. 16, no. August, pp. 124–137, 2017.

[103] A. Staub, A. B. Spierings, and K. Wegener, "Correlation of meltpool characteristics and residual stresses at high laser intensity for metal lpbf process," *Adv. Mater. Process. Technol.*, vol. 5, no. 1, pp. 153–161, 2019.

[104] S. Patel and M. Vlasea, "Melting modes in laser powder bed fusion," *Materialia*, vol. 9, no. November 2019, 2020.

[105] W. Yuan, H. Chen, T. Cheng, and Q. Wei, "Effects of laser scanning speeds on different states of the molten pool during selective laser melting: Simulation and experiment," *Mater. Des.*, vol. 189, p. 108542, 2020.

[106] S. I. Shahabad *et al.*, "Heat source model calibration for thermal analysis of laser powder-bed fusion," *Int. J. Adv. Manuf. Technol.*, vol. 106, no. 7–8, pp. 3367–3379, 2020.

[107] J. Li *et al.*, "Finite element analysis of thermal behavior and experimental investigation of Ti6Al4V in selective laser melting," *Optik (Stuttg).*, no. November, p. 163760, 2019.

[108] M. Bayat, S. Mohanty, and J. H. Hattel, "A systematic investigation of the effects of process parameters on heat and fluid flow and metallurgical conditions during laser-based powder bed fusion of Ti6Al4V alloy," *Int. J. Heat Mass Transf.*, vol. 139, pp. 213–230, 2019.

[109] Z. Zhang *et al.*, "Experimental and numerical investigation on the effect of layer thickness during laser powder-bed fusion of stainless steel 17-4PH," *Int. J. Rapid Manuf.*, vol. 9, no. 2/3, p. 212, 2020.

[110] A. Leicht, U. Klement, and E. Hryha, “Effect of build geometry on the microstructural development of 316L parts produced by additive manufacturing,” *Mater. Charact.*, vol. 143, no. January, pp. 137–143, 2018.

[111] H. Liang *et al.*, “The size effect on forming quality of Ti–6Al–4V solid struts fabricated via laser powder bed fusion,” *Metals (Basel).*, vol. 9, no. 4, 2019.

[112] EOS GmbH - Electro Optical Systems, “Material data sheet EOS NickelAlloy HX Material data sheet Technical data,” 2015.

[113] P. Promoppatum, S. C. Yao, P. C. Pistorius, and A. D. Rollett, “A Comprehensive Comparison of the Analytical and Numerical Prediction of the Thermal History and Solidification Microstructure of Inconel 718 Products Made by Laser Powder-Bed Fusion,” *Engineering*, vol. 3, no. 5, pp. 685–694, 2017.

[114] A. M. Kamara, W. Wang, S. Marimuthu, and L. Li, “Modelling of the melt pool geometry in the laser deposition of nickel alloys using the anisotropic enhanced thermal conductivity approach,” *Proc. Inst. Mech. Eng. Part B J. Eng. Manuf.*, vol. 225, no. 1, pp. 87–99, 2011.

[115] R. Esmaeilizadeh *et al.*, “On the effect of laser powder-bed fusion process parameters on quasi-static and fatigue behaviour of Hastelloy X: A microstructure/defect interaction study,” *Addit. Manuf.*, vol. 38, no. November 2020, p. 101805, 2021.

[116] H. Qin, V. Fallah, Q. Dong, M. Brochu, M. R. Daymond, and M. Gallerneault, “Solidification pattern, microstructure and texture development in Laser Powder Bed Fusion (LPBF) of Al10SiMg alloy,” *Mater. Charact.*, vol. 145, no. August, pp. 29–38, 2018.

[117] J. Irwin and P. Michaleris, “A Line Heat Input Model for Additive Manufacturing,” *J. Manuf. Sci. Eng. Trans. ASME*, vol. 138, no. 11, pp. 1–9, 2016.

[118] K. Zeng, D. Pal, H. J. Gong, N. Patil, and B. Stucker, “Comparison of 3DSIM thermal modelling of selective laser melting using new dynamic meshing method to ANSYS,” *Mater. Sci. Technol. (United Kingdom)*, vol. 31, no. 8, pp. 945–956, 2015.

[119] N. Keller, F. Neugebauer, H. Xu, and V. Ploshikhin, “Thermo-mechanical Simulation of Additive Layer Manufacturing of Titanium Aerospace structures,” *Light. Conf.*, no. Volume 3, Number 5, 2013.

[120] J. Schilp, C. Seidel, H. Krauss, and J. Weirather, “Investigations on temperature fields during

laser beam melting by means of process monitoring and multiscale process modelling," *Adv. Mech. Eng.*, vol. 2014, 2014.

[121] C. Seidel, M. F. Zaeh, M. Wunderer, J. Weirather, T. A. Krol, and M. Ott, "Simulation of the laser beam melting process-approaches for an efficient modelling of the beam-material interaction," *Procedia CIRP*, vol. 25, no. C, pp. 146–153, 2014.

[122] L. Papadakis, A. Loizou, J. Risse, and J. Schrage, "Numerical computation of component shape distortion manufactured by Selective Laser Melting," *Procedia CIRP*, vol. 18, pp. 90–95, 2014.

[123] L. Papadakis, A. Loizou, J. Risse, S. Bremen, and J. Schrage, "A computational reduction model for appraising structural effects in selective laser melting manufacturing: A methodical model reduction proposed for time-efficient finite element analysis of larger components in Selective Laser Melting," *Virtual Phys. Prototyp.*, vol. 9, no. 1, pp. 17–25, 2014.

[124] E. Neiva, S. Badia, A. F. Martín, and M. Chiumenti, "A scalable parallel finite element framework for growing geometries. Application to metal additive manufacturing," *Int. J. Numer. Methods Eng.*, vol. 6, no. October, 2019.

[125] Q. Chen *et al.*, "An inherent strain based multiscale modeling framework for simulating part-scale residual deformation for direct metal laser sintering," *Addit. Manuf.*, vol. 28, no. July, pp. 406–418, 2019.

[126] E. R. Denlinger, M. Gouge, J. Irwin, and P. Michaleris, "Thermomechanical model development and in situ experimental validation of the Laser Powder-Bed Fusion process," *Addit. Manuf.*, vol. 16, pp. 73–80, 2017.

[127] E. J. Street, H. K. Rafi, K. Zeng, A. Hicks, D. Beeler, and B. Stucker, "A Generalized Feed Forward Dynamic Adaptive Mesh Refinement and Derefinement Finite Element Framework for Metal Laser Sintering — Part I : Formulation and Algorithm Development," vol. 137, no. August, pp. 1–15, 2015.

[128] K. Zeng, A. Hicks, D. Beeler, and B. Stucker, "A Generalized Feed-Forward Dynamic Adaptive Mesh Refinement and Derefinement Finite-Element Framework for Metal Laser Sintering — Part II : Nonlinear Thermal Simulations," vol. 138, no. June, pp. 1–10, 2016.

[129] C. Li, C. H. Fu, Y. B. Guo, and F. Z. Fang, "A multiscale modeling approach for fast

prediction of part distortion in selective laser melting," *J. Mater. Process. Technol.*, vol. 229, pp. 703–712, 2015.

[130] M. Siewert, F. Neugebauer, J. Epp, and V. Ploshikhin, "Validation of Mechanical Layer Equivalent Method for simulation of residual stresses in additive manufactured components," *Comput. Math. with Appl.*, 2018.

[131] H. Peng, D. B. Go, R. Billo, S. Gong, M. R. Shankar, and B. A. Gatrell, "Part-scale model for fast prediction of thermal distortion in DMLS additive manufacturing ; Part 2 : a quasi-static thermomechanical model," pp. 382–397, 2016.

[132] S. Afazov, W. A. D. Denmark, B. Lazaro Toralles, A. Holloway, and A. Yaghi, "Distortion prediction and compensation in selective laser melting," *Addit. Manuf.*, vol. 17, pp. 15–22, 2017.

[133] R. K. Ganeriwala *et al.*, "Evaluation of a thermomechanical model for prediction of residual stress during laser powder bed fusion of Ti-6Al-4V," *Addit. Manuf.*, vol. 27, no. December 2018, pp. 489–502, 2019.

[134] A. Keshavarzkermani *et al.*, "Controlling mechanical properties of additively manufactured hastelloy X by altering solidification pattern during laser powder-bed fusion," *Mater. Sci. Eng. A*, vol. 762, no. June, p. 138081, 2019.

[135] Y. Li, K. Zhou, P. Tan, S. B. Tor, C. K. Chua, and K. F. Leong, "Modeling temperature and residual stress fields in selective laser melting," *Int. J. Mech. Sci.*, vol. 136, no. November 2017, pp. 24–35, 2018.

[136] N. C. Levkulich, S. L. Semiatin, J. E. Gockel, J. R. Middendorf, A. T. DeWald, and N. W. Klingbeil, "The effect of process parameters on residual stress evolution and distortion in the laser powder bed fusion of Ti-6Al-4V," *Addit. Manuf.*, vol. 28, pp. 475–484, Aug. 2019.

[137] H. Suzuki, K. Akita, and H. Misawa, "X-ray stress measurement method for single crystal with unknown stress-free lattice parameter," *Japanese J. Appl. Physics, Part 1 Regul. Pap. Short Notes Rev. Pap.*, vol. 42, no. 5 A, pp. 2876–2880, 2003.

[138] J. Wu, J. Zhao, H. Qiao, Y. Zhang, X. Hu, and Y. Yu, "Evaluating methods for quality of laser shock processing," *Optik (Stuttg).*, vol. 200, no. June 2019, p. 162940, 2020.

[139] M. Gelfi, E. Bontempi, R. Roberti, and L. E. Depero, "X-ray diffraction Debye Ring Analysis

for STress measurement (DRAST): A new method to evaluate residual stresses," *Acta Mater.*, vol. 52, no. 3, pp. 583–589, 2004.

[140] J. Lin, N. Ma, Y. Lei, and H. Murakawa, "Measurement of residual stress in arc welded lap joints by cosα X-ray diffraction method," *J. Mater. Process. Technol.*, vol. 243, pp. 387–394, 2017.

[141] T. Sasaki, K. Koda, Y. Fujimoto, S. Ejiri, T. Suzuki, and Y. Kobayashi, "X-Ray Residual Stress Analysis of Stainless Steel Using cos$α$ Method," in *THERMEC 2013 Supplement*, 2014, vol. 922, pp. 167–172.

Appendix A. Theoretical calculation of residual stress using X-ray analyzer machine

A.1 Residual stress

In this section, the formation of the residual stress is described. Fig. A.1 shows the schematic of the residual stress formation in the iron bar. The external force (thermal force created by laser heat source) is applied to the material. This force results in bending the iron bar which generates tensile and compressive plastic deformation in the upper and lower surface regions of the bar, respectively. In addition, in some regions within the bar, there is no plastic deformation, marking the transition between the tensile and compressive induced stresses. After removing the external force, the bar may not recover to its original shape, therefore, these localized plastic deformed areas within the surface regions induce stresses in the non-plastically deformed regions of the bar. The remaining stresses can be defined as the residual stresses.

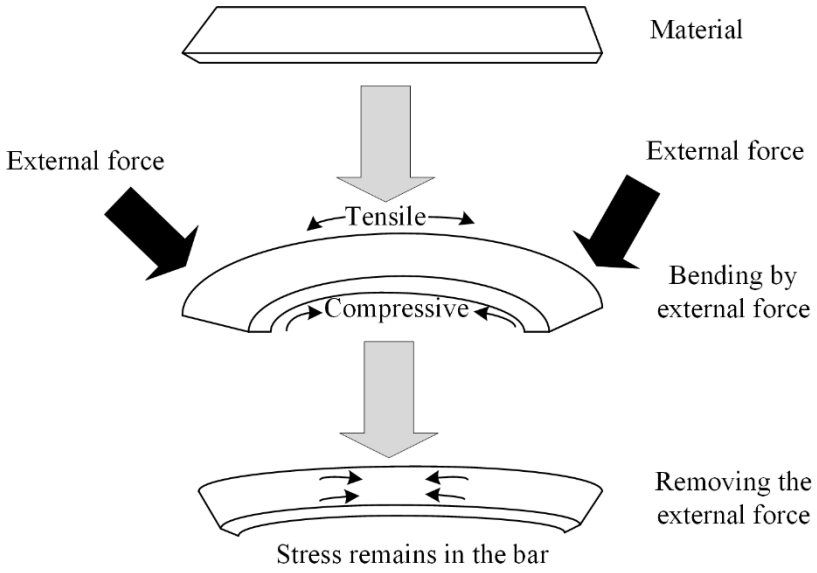

Fig. A.1. Schematic of residual stresses formation.

A.2 X-ray residual stress measurements

The crystal grains of polycrystalline metals that have no residual stress are contained of atoms in their thermal positions creating highly ordered planes that form the crystal lattice. The force is spread amongst the crystal grain when the external force is imposed. The crystal lattice's interplanar distances can be whether increased or decreased depending on the direction and angle of the stress

with respect to the crystal planes [137]. By identifying the variation of the lattice interplanar distance and the elastic constants of the metal, the residual stress measurements can be conducted. The smaller lattice interplanar distance can be achieved when the direction of the external force is close to the parallel direction of the crystal plane's orientation. On the other hand, the distance becomes larger as the external force's direction is close to the direction perpendicular to the crystal plane's orientation. In addition, by applying the tensile force, the lattice interplanar distance increases, whereas the distance decreases as the compressive force is applied.

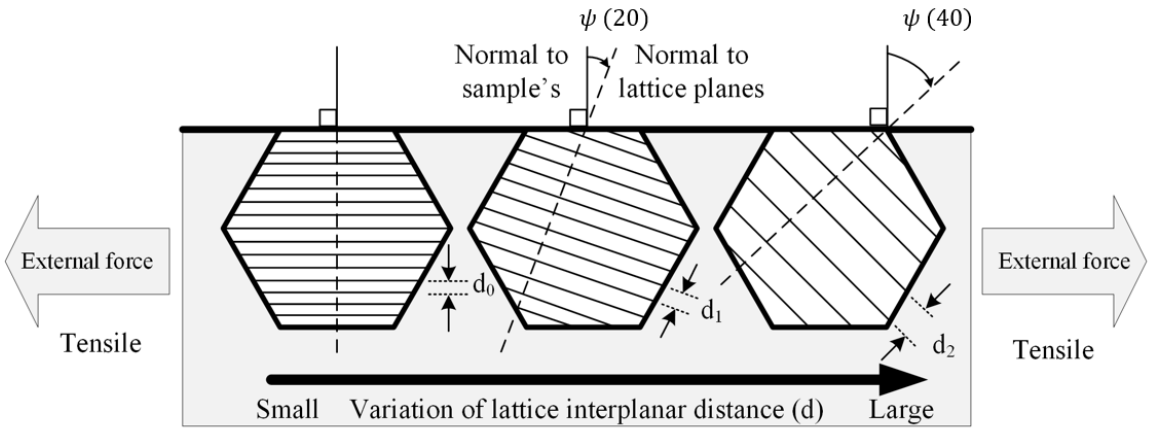

Fig. A.2. Schematic of the variation of lattice interplanar distance.

The atoms in the crystal lattice planes scatter the X-rays as they irradiate the metal sample. The scattered X-rays with the coherent phase relationship strengthen each other boosting the scattered X-rays, whereas X-rays with an incoherent phase relationship lessens the X-ray scattering. This phenomenon is called diffraction (as defined by Bragg's law). By using the relationship between X-ray wavelength and the knowledge of the metal's interplanar distance, the X-ray diffraction angle which is called 2θ angle can be calculated.

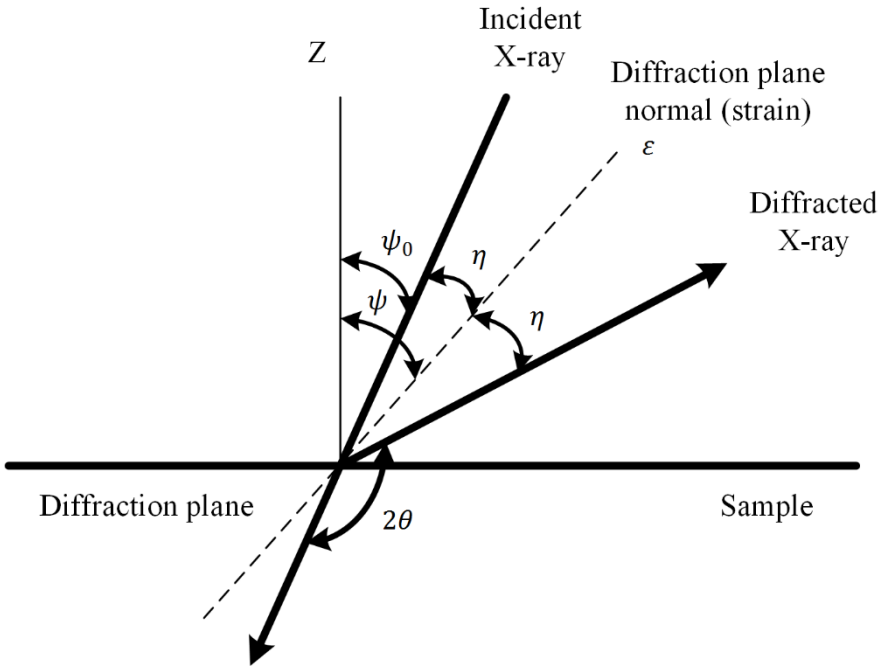

Fig. A.3. Schematic of X-ray diffraction.

The incident X-ray is 360º-omnidirectionally diffracted, by polycrystalline samples, creating an angle with the diffracted X-ray. The angle is represented by 2θ. The angle (2θ) of the diffracted X-rays can be varied according to the amount of residual stress.

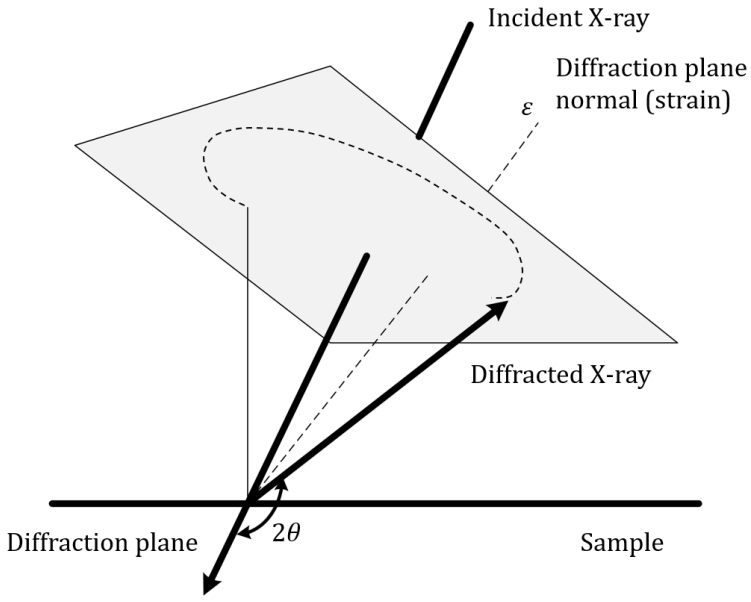

Fig. A.4. The schematic incident X-ray and diffraction plane.

A.3 The cos α method

In this method, X-rays are 360º-omnidirectionally diffracted from the sample's polycrystalline structure around the path of incident X-rays and are detected by the 2-dimensional detector.

The residual stress is calculated from the change to the diffraction angle due to the influence of the residual stress on the interplanar distances within the grain's crystal structure.

Due to the ability to detect the complete Debye-Scherrer ring in a single exposure, the μ-X360s can be made of a compact and light-weight system.

In addition, in this method the angle of incident X-rays (ψ_0) is not required to be changed comparing with the $\sin^2\psi$ method. Moreover, the μ-X360s has the capability to determine the texture within a sample and specifying the grain size. This information can be detected by the intensity distribution derived from the Debye-Scherrer ring.

The two-dimensional detector can distinguish the diffracted X-rays with high precision. Due to having the high sensitivity of the detector, the X-ray source utilizes relatively low power. This enables the μ-X360s to be operated with a battery for measurements in locations where there is no access to the power source. Another advantage of using high sensitive detecter is that it enables to have relatively short irradiation times. The sequence of operation from X-ray irradiation, data reading to initialization is automatically processed which leads to an easy operation for conducting the XRD residual stress measurements. These advantages offer the potential for on-site residual stress measurements.

The residual stress is calculated from the following formula [138]–[140]. The maximum number of α_1 is 125 data because the resolution of μ-X360s is 500 points per 360 degrees.

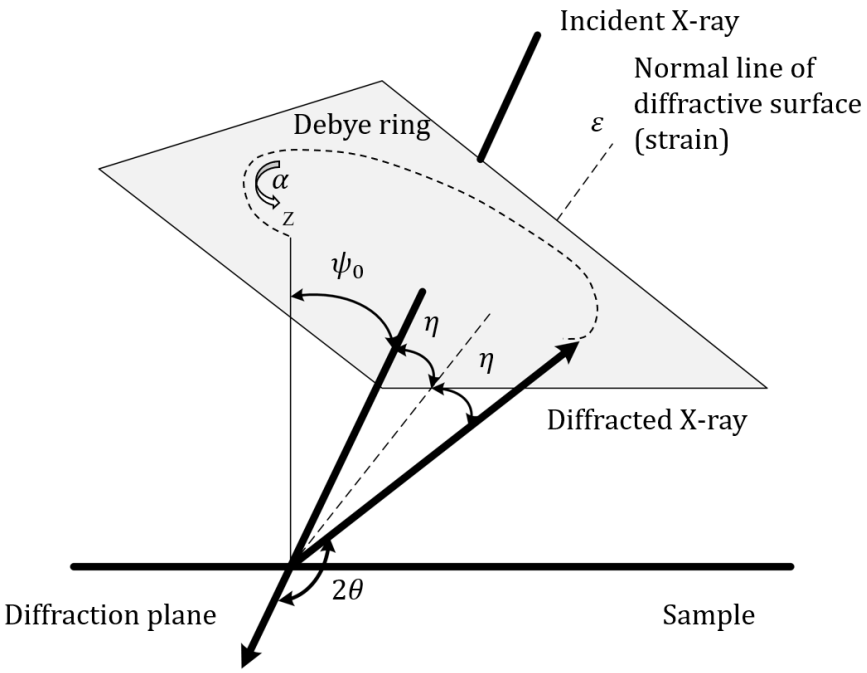

Fig. A.5. Schematic of the debye ring.

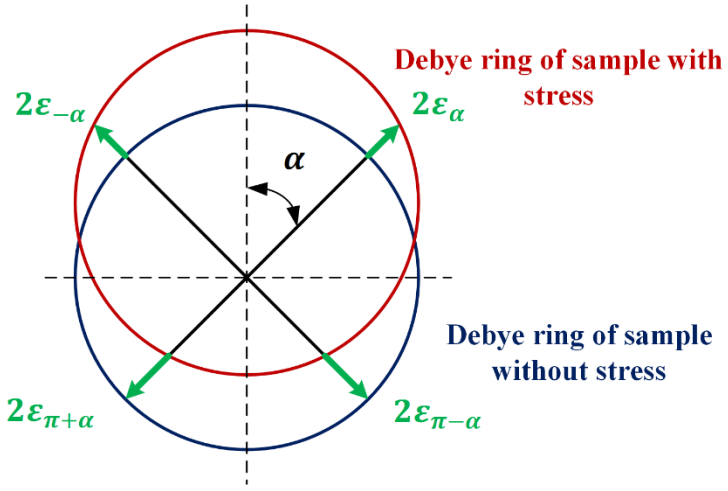

Fig. A.6. Mechanism of the stress measurement based on cos α.

$$\varepsilon_\alpha = \frac{\sigma_x}{E}[{n_1}^2 - \nu({n_2}^2 + {n_3}^2)] + \frac{\sigma_y}{E}[{n_2}^2 - \nu({n_3}^2 + {n_1}^2)] + \frac{2(1+\nu)}{E}\tau_{xy}n_1n_2 \quad \text{(A.1)}$$

$$\sigma_x = -\frac{E}{1+\nu}\frac{1}{\sin 2\eta}\frac{1}{\sin 2\psi_0}\left[\frac{\partial \alpha_1}{\partial \cos_\alpha}\right] \tag{A.2}$$

where ε_α is the strain, σ_x is the residual stress, n_1, n_2, n_3 are the orientation cosine, respectively. E is Young's modulus, ν is the Poisson's ratio [140].

Defining

$$n_1 = \cos\eta \sin\psi_0 \cos\phi_0 - \sin\eta \cos\psi_0 \cos\phi_0 \cos\alpha - \sin\eta \sin\phi_0 \sin\alpha \tag{A.3}$$

$$n_2 = \cos\eta \sin\psi_0 \sin\phi_0 - \sin\eta \cos\psi_0 \sin\phi_0 \cos\alpha + \sin\eta \cos\phi_0 \sin\alpha \tag{A.4}$$

$$n_3 = \cos\eta \cos\psi_0 + \sin\eta \sin\psi_0 \cos\alpha \tag{A.5}$$

$$\alpha_1 = \frac{1}{2}[(\varepsilon_\alpha - \varepsilon_{\pi+\alpha}) + (\varepsilon_{-\alpha} - \varepsilon_{\pi-\alpha})] \tag{A.6}$$

where ϕ_0 is the orientation angle between the projection of input X-ray on the sample surface and axis x.

In the cos α method, the residual stress is determined by the Debye-Scherrer ring. Because of more measuring points in the ring, this method is more reliable than the $\sin^2\psi$ method [138], [141].